journal of the international meteor organization

WGN

46:1
february 2018

Time perception of a meteorite fall
Efficiency of cameras for video meteor observation
Video meteor astrometry
Mass and magnitude distributions of meteor showers
Visualizing meteor streams by radio forward scattering
July video meteors

ISSN 1016-3115

WGN Vol. 46, No. 1, February 2018, pp. 1 – 50

Administrative

Conferences

Meteor science

Radio meteors

Preliminary results

Front cover photo

Aurora and Geminid Fireball over Lovozero Lake, Murmansk, Russia. December 2017. ©Yang Sutie.

Back over photo

Four Geminid meteors recorded in this 15-minute star trail taken at Pedra da Boca State Park in Paraiba, Brazil on 2017 December 14, using Nikon D5100 camera with Rokinon 14 mm F2.8 lens, combining 39 photos of 20 s exposures at ISO 6400. Photo courtesy: Marcelo Zurita.

Writing for WGN

This Journal welcomes papers submitted for publication. All papers are reviewed for scientific content, and edited for English and style. Instructions for authors can be found in WGN **45:1**, 1–5, and at `http://www.imo.net/docs/writingforwgn.pdf` .

Legal address

International Meteor Organization, Jozef Mattheessensstraat 60, 2540 Hove, Belgium.

Janus

Cis Verbeeck[1]

Welcome to the first WGN issue of 2018! The start of a new year offers an opportunity to reflect: what did we achieve in the past year? Which opportunities are at hand and what do we want to achieve in the near future? Sanity check: what does the International Meteor Organization stand for? What are its goals? Are we on the right track or do we need to refocus?

IMO's mission

In my view, IMO's very reasons of existence are to connect meteor workers so they can share their work and passion for meteors, to aid the meteor community by collection and distribution of data and information, to foster new ideas, and to make things happen. All these aspects contribute to the advance of meteor science. IMO is at its best when its officers sense what is hanging in the air, catalyze promising evolutions, and help make things happen. Recent examples are the development of the video flux viewer and the organization of the visual and spectroscopic workshops at the IMC 2018.

Connecting people

As an international organization, IMO has torn down walls and enables meteor workers around the globe to get to know each other and to collaborate. New ideas get born when you bring people together. The IMC, IMO's annual conference, is the most powerful way of bringing meteor workers together, and each IMC concludes with a burst of new ideas, collaborations and the exciting feeling of shared passion by fellow meteor enthusiasts who very often have become good friends. Nowadays, the IMO website, the IMO Facebook page, and the IMO forum provide a great platform to strengthen contacts throughout the year. So show your meteor work online, and employ these tools to reach out and connect!

Information is one of the pillars of our organization. IMO informs beginners about all aspects of meteor science and presents an overview of recent meteor-related news on the IMO website and more in-depth analyses and stories in WGN or in the Proceedings of the IMC. As a courtesy towards IMO members, the IMO Council has decided to provide the pdf version of the Handbook For Meteor Observers and the Meteor Shower Handbook for free to IMO members. IMO's annual Meteor Shower Calendar is an invaluable tool for meteor observers, presented for free on the IMO website.

Gathering and distributing data

An essential aspect of meteor science is gathering data. IMO strives to define objective and efficient observation methods and data formats, to provide clear instructions to observers, to collect data worldwide in a user-friendly way, and to provide easy access to global data. For visual observations, most of these objectives were met from the time of IMO's foundation in 1988 onwards. Thanks to the updated Visual Meteor Data Base, all visual data are now within easy reach of anyone. This rich data set is screaming out to be exploited more heavily. In order to share our experts' knowledge on the analysis of visual meteor data, IMO organizes a workshop on visual observations one day prior to the IMC 2018 in Slovakia.

Since its inception many years ago, the field of video meteor observations has reached a diverse and mature state, with several networks and systems providing complementary information about meteors. The IMO Video Meteor Network comprises over 75 cameras, and interesting monthly analyses of meteor activity are published in WGN. All its data can be found in the IMO Video Meteor Database, and are exported to the EDMOND database regularly. During the IMC 2017, Video Commission Director Sirko Molau, Mike Hankey, Vladimir Nikolić and his colleagues from Petnica Science Center joined forces to start working on a near real time video flux viewer.

Radio observations of meteors are an inherently indirect and rather complicated way of studying meteors. Though no standard data format is currently employed for radio observations and there is no IMO database for radio observations, the Radio Meteor Observing Bulletin (RMOB) has gathered radio data worldwide since 1993. At present, no single standardized reduction method for radio data is in use, but promising advances have been made in the past years, for example by Ogawa and Steyaert (2017) and the BRAMS team (Verbeeck et al., 2018). I expect this field to grow to a more mature state in the years to come.

The field of spectroscopic meteor observations has reached the point where experts need to sit together and discuss a standard methodology and data format. This is exactly the purpose of IMO's Spectroscopic Workshop which will take place one day prior to the IMC 2018.

[1] Bogaertsheide 5, 2560 Kessel, Belgium.
Email: cis.verbeeck@scarlet.be

IMO bibcode WGN-461-verbeeck-janus NASA-ADS bibcode 2018JIMO...46....1V

Though few people are currently employing infrasound to observe fireballs, I expect this field will be growing in the next years. IMO strives to distribute information on this exciting technique and encourages meteor workers to start infrasound observations.

Ever more fireballs

One of the most striking trends in the last few years, is the rise in numbers of reported and filmed fireballs, and even of recovered meteorites. Since IMO's online fireball form was launched in 2015, 15 809 fireball reports and 4 964 events were reported through the IMO fireball form (apart from the large American Meteor Society contribution, where fireball report collection started already in 2005). The 2017 statistics are compared to those of 2016 in Tables 1 and 2. We clearly see that IMO's contribution to the fireball form statistics is rising. A new feature for the fireball form was introduced in 2017: the ability to add images, videos, and other information to a fireball report. This allows us to combine all fireball information in one place, enhancing the chances for swift recovery of meteorites.

Table 1 – Number of fireball reports in 2016 and 2017 (total number of reports, number of reports entered via IMO form or customized form (non-AMS), and percentage of reports entered via IMO form or customized form).

Year	Number of reports	Number of IMO reports	IMO contribution (%)
2016	26 622	3 635	14%
2017	28 219	8 096	29%

Table 2 – Number of fireball events in 2016 and 2017 (total number of events, number of events entered via IMO form or customized form (non-AMS), and percentage of events entered via IMO form or customized form).

Year	Number of events	Number of IMO events	IMO contribution (%)
2016	5 365	1 512	28%
2017	5 446	1 844	34%

Do you remember the following striking events of 2017?

- L6 ordinary chondrite (530 g) recovered in Broek in Waterland, the Netherlands, after bright fireball at $16^{\mathrm{h}}09^{\mathrm{m}}$ UT on January 11.
- Several meteorite fragments recovered (largest one: 1 kg) in Ait Ouabelli, Southeastern Morocco, after bright fireball at $22^{\mathrm{h}}10^{\mathrm{m}}$ UT on July 12.
- Bright fireball over Northern US and British Columbia at $04^{\mathrm{h}}53^{\mathrm{m}}$UT on July 30, reported by 888 people.
- Bright fireball over The Netherlands at $19^{\mathrm{h}}01^{\mathrm{m}}$ UT on September 21, reported by 479 witnesses. Magnitude -10, duration 5.3 seconds, 16° above horizon, speed 31 km/s, light path ended offshore. This meteoroid was a Northern delta-Piscid, hence a nucleus fragment of 2P/Encke.
- Huge fireball over Yunnan province, China at $12^{\mathrm{h}}07^{\mathrm{m}}05^{\mathrm{s}}$ UT on October 4. According to CNEOS/NASA (Center for Near Earth Objects Studies), this was the 4th most energetic atmospheric entry of the year, and the most energetic one over China since December 15, 2000! Probably a small asteroid (a few meters large) entering at 15 km/s.
- Bright fireball over Germany at $16^{\mathrm{h}}48^{\mathrm{m}}$ UT on November 14 is most reported fireball event from Europe since launch of IMO fireball form (2 045 reports from 7 different versions of the fireball form).
- Very bright fireball over Northern Finland at $16^{\mathrm{h}}40^{\mathrm{m}}$ UT on November 16, estimated magnitude -20, the meteor blast was felt by many people.

Several very performant fireball and video meteor networks are already in place, and more are yet to come. For instance, Mike Hankey plans to cover the US with a new network of $\sim$ 350 cameras (1 % ready). I am convinced that close collaboration between all those networks and with IMO's fireball form will further advance the already impressive quantity and quality of fireball data, as well as meteorite recoveries. IMO will do whatever it can to support this development.

Spreading the word

Did we address all of IMO's activities here? No, at least one aspect still needs to be mentioned: IMO aims to (help people) spread the word that meteors are awesome! IMO's website, Facebook, and Twitter channels are great for introducing the wonderful world of meteors to ever more people around the globe. And they are being used as well. In 2017, IMO's Facebook account had 7 700 video views, which is 1 201% as compared to 2016. The most shared Facebook post (about the August 5 fireball over Seattle) reached 66 068 people.

Figure 1 – IMO is at its best when its officers sense what is hanging in the air, catalyze promising evolutions, and help make things happen.

Thank you!

Following the 2017 IMO Council elections, Marc Gyssens, Detlef Koschny, Robert Lunsford, Sirko Molau, Jean-Louis Rault, and Jürgen Rendtel were re-elected as Council members (for 2018–2021), and I was re-elected as President. I would like to thank all voters for their support. As President, together with the other Council members, I will continue my dedication to monitor and foster our organization's health for many years to come.

Geert Barentsen did not renew his term in the IMO Council. Geert has been Council member since 2010, has been IMO webmaster and was the main person behind the Virtual Meteor Observatory and the online ZHR plots in the previous version of the IMC website, as well as the MetRec FluxViewer, which serves as prototype for the real time video flux viewer currently under construction. We will miss Geert's original ideas, thorough and careful evaluation of proposals and situations, and passionate involvement in our organization. In name of the IMO Council, I thank Geert for all the great work he has done for IMO.

In the past months, the function of Press Officer has been abolished as it turned out that press releases in case of a major fireball were typically drafted by national groups, with help from the IMO news editors, within hours of the event. Adapting to this reality, I have instead established a list of national Points of Contact in many countries that will communicate quickly with the IMO news editors in case of a major event in their country. In name of the Council, I thank Megan Argo for the good work that she has performed as Press Officer.

Needless to say, IMO's achievements are only possible through the dedication of many volunteers, such as WGN's Editor-in-Chief Javor Kac, our webmaster Karl Antier, and Mike Hankey and Vincent Perlerin who developed and maintain the IMO website and fireball form. Essential tasks are performed by the IMO Council members and Commission Directors and many more volunteers. Without mentioning them all in detail, I want to thank them all for their part in running the International Meteor Organization!

How would *you* define IMO's mission?

IMO is *your* organization, it is there to support your meteor activities. Do you support IMO's mission as described above? Or do you have different or extra ideas? Your opinion is much appreciated, and I invite you to comment on this Janus article and provide your own suggestions, either as a letter to WGN or as an online reaction to the website Janus article. Let your voice be heard!

Call for action

I invite you all to join the effort and make things happen in 2018! Perform those observations, submit those data, use that database and analyze that shower return, write that paper, share your work, your passion about meteors, the beauty of it all through internet. Share and like that meteor post, put IMO's fireball form on your website, and attend that International Meteor Conference to take an overwhelming meteor bath. The opportunities abound! IMO is there for you. Share your thoughts, experiences and wishes and help us make it even better.

References

Ogawa H. and Steyaert C. (2017). "Major and daytime meteor showers using global radio meteor observations covering the period 2001–2016". *WGN, Journal of the IMO*, **45:5**, 98–106.

Verbeeck C., Lamy H., Calders S., Tétard C., and Martínez Picar A. (2018). "Overview of major shower observations 2016–2017 by the BRAMS network". In *Proceedings of the International Meteor Conference 2017, Petnica, Serbia, September 21–24*. (in press).

Janus *was a Roman god with two faces, one looking to the past and one to the future, called upon at the beginning of any enterprise. Today he is often a symbol of re-appraisal at the start of the year.*

Conferences

Announcement: Visual Workshop, Pezinok-Modra, Slovakia, August 29–30, 2018

Cis Verbeeck

Introduction

Right before the IMC 2018, a Visual Workshop will be organized at the conference venue. The Workshop will focus on a hands-on session where experts share their experience in a global analysis of the visual observations of the Perseids 2016, using the Visual Meteor Database and the MetFns analysis software. With this software having been updated recently, we feel the timing for such a workshop is just right. We hope it will contribute to helping meteor workers to get the most out of the IMO's visual (and other) meteor data, e.g., by performing global analysis of meteor showers themselves.

Practical information and program

The Visual Workshop will start at 14^{h} on Wednesday, August 29, and end at 18^{h} on Thursday, August 30. A detailed program will be provided in due time.

People interested in data analysis of visual or other meteor observations are encouraged to participate.

Cost

Participation in the Visual Workshop is free. The extra night of August 29-30 and the extra meals (lunch and dinner on August 29 and lunch on August 30) should be arranged with the hotel by the participants themselves, just like any other additional nights or meals you may wish. If you mention "IMC2018" while booking, a double room for one night costs 50 Euro plus 0.33 Euro tax (including breakfast), and a meal costs 8.50 Euro. These prices are not guaranteed if you use third parties such as `booking.com` to book the hotel. If you would like to share a double room during the workshop, please mail this request to `imc2018@imo.net` before booking the room. The LOC can then assist you with finding a roommate with whom you can share the room cost.

Registration

If you want to participate, please check "I register for the Visual Workshop" on the IMC registration form (`http://imc2018.imo.net/registration`). People who already registered for the IMC before this option was available may send a mail to `imc2018@imo.net`.

IMO bibcode WGN-461-verbeeck-visual NASA-ADS bibcode 2018JIMO...46....5V

Announcement: Spectroscopic Workshop, Pezinok-Modra, Slovakia, August 29–30, 2018

Regina Rudawska, Juraj Tóth

Introduction

Right before the IMC 2018, a Spectroscopic Workshop will be organized at the conference venue. The Workshop is limited to experts and will focus on the discussion of spectroscopic methodology and data format. Spectroscopy in meteor observing is an emerging technology in which several research groups have meanwhile gathered considerable expertise, and the time is now ready to bring this expertise together.

Practical information and program

The Spectroscopic Workshop will start at 14^{h} on Wednesday, August 29, and end at 18^{h} on Thursday, August 30. A detailed program will be provided in due time.

Experts in spectroscopic observations and/or analysis are encouraged to participate.

Cost

Participation in the Spectroscopic Workshop is free. The extra night of August 29-30 and the extra meals (lunch and dinner on August 29 and lunch on August 30) should be arranged with the hotel by the participants themselves, just like any other additional nights or meals you may wish. If you mention "IMC2018" while booking, a double room for one night costs 50 Euro plus 0.33 Euro tax (including breakfast), and a meal costs 8.50 Euro. These prices are not guaranteed if you use third parties such as `booking.com` to book the hotel. If you would like to share a double room during the workshop, please mail this request to `imc2018@imo.net` before booking the room. The LOC can then assist you with finding a roommate with whom you can share the room cost.

Registration

If you want to participate, please check "I register for the Spectroscopic Workshop" on the IMC registration form (`http://imc2018.imo.net/registration`). (People who already registered for the IMC before this option was available may send a mail to `imc2018@imo.net`.) Note that due to the expert character of the workshop, participation requires confirmation by the workshop organizers.

IMO bibcode WGN-461-rudawska-spetroscopic NASA-ADS bibcode 2018JIMO...46....5R

Meteor science

Time perception of a meteorite fall

A. Egal[1,2], *K. Veljkovic*[3], *J. Vaubaillon*[2,4], *M.-K. Kwon*[5], *V. Perlerin*[4,6], *M. Hankey*[4,6], *F. Colas*[2], *W. Thuillot*[2]

A study of the ability of human beings to correctly estimate and count the time in case of a meteorite fall is performed. Three videos showing a simulation of a bolide are shown to more than 500 people, who are asked to guess the duration of the phenomenon. The people take each test twice: first without knowing what to see nor what will be asked of them, and second knowing they have to estimate the duration of the event. The experiment is repeated for different populations, durations, and with or without fragmentation. The results obtained were overall analyzed by statistical tests to investigate the effects of these parameters on the accuracy of the time estimates. An illustration of the effective percentage of individuals able to either accurately count and guess the duration of the phenomenon for each simulation is also presented. We show that in the case of a long (duration $\geq$ 4 s) and fragmenting fireball, a small number of visual observations would likely lead to a significant underestimate of the phenomenon duration, especially when the witnesses are not expecting such an event.

Received 2017 September 5; Re-submitted 2018 February 12

1 Introduction

Thanks to the extension of meteors detection networks, it is rare for a meteorite fall in highly populated areas to be detected today only by human observers. Such an energetic event generally appears on seismological and radar surveys of civilian and military surveillance networks, like the case of the Chelyabinsk fireball over Russia in February 2013 (Emel'yanenko et al., 2013), which allow to roughly estimate the location of the phenomenon. The coupling of this information with the visual observations of fireballs has proved its efficiency in the search for meteorites. Eyewitness-reports of fireballs allowed scientists to find meteorites shortly after their fall in Europe (Haack et al., 2012) and by 7 times over the American ground (Jenniskens et al., 2012; Fries et al., 2014; Hankey & Perlerin, 2016). For decades, various organizations like the International Meteor Organization (IMO) and the American Meteor Society (AMS) have therefore been mobilizing people to collect as much observations of fireballs as possible.

In the case of a meteorite fall not recorded by a detection network, fireball observation reports become the only information that can be use to determine the location and the orbit of the body. This situation also applies to events having occurred in the past centuries, like the Orgueil meteorite fall in France in 1864. In order to identify the dynamic origin of these bodies, the meteoroids trajectories and velocities have to be carefully computed from visual observation reports. Among the observable characteristics of a fireball, an accurate estimate of the phenomenon duration is particularly crucial to reduce the uncertainty of the potential impact zone of a meteorite (Andreic, 2012). It is also an essential parameter to determine the velocity and the orbit of the meteoroid. The purpose of this work is therefore to evaluate how accurate the time perception of a meteorite fall observed by a human being can be.

As a first step, such a study can be performed by comparing visual witnesses and video records of the same fireball (e.g. Moser (2017)). Unfortunately, these comparisons are difficult to assess. On one hand, because observers and cameras generally don't observe the same part of the trajectory of a fireball (it is at least hard to define). On the other hand, because visual witnesses usually provide too varied duration estimates to allow a reliable analysis of the observations. In this work, the ability of individuals to evaluate a time duration is rather tested using different and reproducible fireballs simulations. By analyzing the time perception accuracy of several samples of population, representing more than 500 individuals, we propose to investigate the following questions:

q.1 Are people able to estimate a short duration (3–7 s) with an accuracy of 1 s or better?

q.2 Is this accuracy worse when we do not expect to observe and analyze a fireball?

q.3 Do the estimate errors follow a trend (underestimate, overestimate)?

q.4 Does the time perception accuracy depend on:
a. The preparation (expecting to analyze the phenomena or not);
b. The knowledge of meteor science;
c. The phenomena duration;
d. Other characteristics (like a fragmentation)?

[1]Department of Physics and Astronomy, University of Western Ontario, London, ON, N6A 3K7, Canada. Email: aegal@uwo.ca
[2]IMCCE, Observatoire de Paris, PSL Research University, CNRS, Sorbonne Universités, UPMC Univ. Paris 06, Univ. Lille., France.
[3]Department of Probability and Statistics, Faculty of Mathematics, University of Belgrade, Serbia.
[4]International Meteor Organization.
[5]IRAP, UMR 5277, Université de Toulouse [UPS-OMP] / CNRS.
[6]American Meteor Society, USA.

IMO bibcode WGN-461-egal-time
NASA-ADS bibcode 2018JIMO...46....7E

In Section 2, the pertinence of comparing visual observations to video records of fireballs to estimate the accuracy of eyewitnesses reports is investigated. Section 3 presents the characteristics of the experiment conducted with simulations, and the results obtained are analyzed in Sections 4 and 5. The validity of the results obtained are discussed in Section 6 and summarized in Section 7.

2 Comparison with video records

A natural idea when planing to estimate the accuracy of visual observations of fireballs is to compare them to video records of the same events. Such a study was for example performed by Moser (2017), who found a correlation between 33 events listed in both the AMS and the NASA fireball detection network databases and determined the precision obtained on the direction, duration, altitude and speed of these objects from the visual testimonials. The estimated error on the velocity varied for these fireballs from 2% in the case of an exceptionally precise trajectory determination to 209% in the case of a bad determination. The mean error of the velocity estimate from visual observations of these fireballs is about 75% in the case of a low number of concordant testimonies (< 75), and about 20% in the case of a higher number of reports. By using the AMS & IMO visual observations databases, we can conduct a similar study focused on the duration estimate of a fireball.

2.1 AMS/IMO fireball report

The American Meteor Society (AMS) has accepted reports of suspected fireballs from the general public from as far back as 1922 (Olivier, 1925) and online since 2005 (Hankey et al., 2014). The online version of this citizen science program is based on an advanced data collection, Google Maps and custom-widgets-driven user interface that allowed eyewitnesses with little to no astronomical knowledge to record their observation. In 2014, the AMS online fireball report form was translated into 30 languages and made available worldwide through 25 different websites[a,b] thanks to the International Meteor Organization (IMO). This online form is now used yearly by tens of thousands of people (26 464 reports were submitted in 2016).

2.2 Duration estimate

The first version of this observation report made it possible to freely indicate the estimated duration of a fireball. The analysis of the results obtained in this way seems to indicate that most of the time, the witnesses underestimate the actual duration of the phenomenon and overestimate its magnitude (most of the time, the fireball is described as "as bright as the sun"). However, the wide range of time estimates associated with a unique fireball prevented any reliable estimate of the phenomenon duration. The report form was then updated to force the user to select a time interval (<1 s, 1 – 2 s, 2 – 5 s, 5 – 10 s, 10 – 30 s, 30 s – 1 min and more than 1 minute) and not to provide a direct estimate of the duration, which is then assimilated to the mean value of each answer interval (e.g. 1.5 s, 3.5 s, 7.5 s, 20 s, etc.).

An example of the results obtained for eight fireballs reported to the AMS is presented in Table 1. For these examples, we see that the most frequent category selected is {2 to 5 s}, whatever the real duration of the fireball is. About 50% of the visual witnesses selected a category containing the duration recorded by video devices. When a wrong time interval is chosen, it usually leads to an underestimate of the real duration of the fireball (e.g. events lasting more than 5s). From these examples, we see that the new version of the form still remains not fully satisfactory. Indeed, it is sometimes difficult to discriminate between two proposed time intervals (like for the AMS 614-2017 event, Table 1). It is also conceivable that the width of each category of solutions tends to favor the choice of the largest interval when the user hesitates between two categories. Finally, the duration of the phenomenon is assimilated to the average value of the proposed interval, and is then constrained to take fixed discrete values (1.5 s, 3.5 s, 7.5 s, etc.) which prevent the exploitation of the results obtained with confidence. The duration estimates provided with this form are therefore only used to exclude events that are too long to be a fireball (entry of debris, Chinese lanterns, etc.). Given the poor agreement of the durations estimated by the witnesses, any computation of velocities and orbits from visual observations was excluded by the IMO and the AMS organizations.

2.3 Reliability of the reports

The quality of the results obtained from a citizen science approach such as the AMS/IMO Fireball program mostly depends on the number of reports submitted for a given event, and not only on the quality of each individual report. The AMS/IMO citizen-science projects mainly rely on witnesses with no astronomical knowledge and no experience in meteor watching. Human factors such as the capacity of the witness to answer simple questions, as well as their relative location to the event, play a determinant role in the quality of the results obtained. The reliability of the estimated trajectory also depends on the weather conditions at the time of the event, the density of population of the involved areas and the time of the event. Another important factor for the reliability of the report of the eyewitnesses is the time elapsed between the event and the report submission. The study of the fireball spotted over Wisconsin on 2017 February 6, $07^{\mathrm{h}}25^{\mathrm{m}}$ UT (Perlerin, 2017) shows for instance the difference between the trajectory obtained from all the 507 reports received for this event and the trajectory obtained only from the reports submitted less than 4 hours after the fireball appearance (a total of 140 reports). The end of the first trajectory was more than 14.24 km away from the possible impact zone determined from Doppler Weather radar data (Fries et al., 2014), while the second one was right on the possible impact zone – see Figure 1. This illus-

[a] http://www.amsmeteors.org/ams-programs/visual-observing
[b] http://fireballs.imo.net

Table 1 – Example of durations reported to the IMO/AMS for eight fireballs recorded by a video camera.

IMO/AMS event	Nb of reports	video	?	< 1 s	1.5 s	3.5 s	7.5 s	20 s	45 s	Underestimate	Right category	Overestimate
4239-2016	368	3	0	5.2	37.8	48.6	5.7	2.7	0	43	48.6	8.4
1298-2017	542	4	0.4	3.1	31.2	57.7	5.9	1.7	0	34.3	57.7	7.6
454-2017	511	4	1.6	3.1	27.4	51.1	13.1	2.9	0.8	30.5	51.1	16.8
302-2017	138	4	2.2	8.7	30.4	42	10.1	5.8	0.7	39.1	42	16.6
614-2017	72	5	0	4.2	45.8	41.7	6.9	1.4	0	50	41.7	8.3
340-2016	965	5	0.93	0.1	2.8	27.98	55.85	10.67	1.66	30.88	55.85	12.33
1882-2016	421	6	2.1	2.6	21.4	52.3	15.4	5.0	1.2	76.3	15.4	6.2
1750-2016	857	6	2.8	2.6	21.6	50.8	16	4.9	1.4	75	16	6.3
2563-2017	280	8	0	0	16.4	62.1	17.5	3.6	0.4	78.5	17.5	4

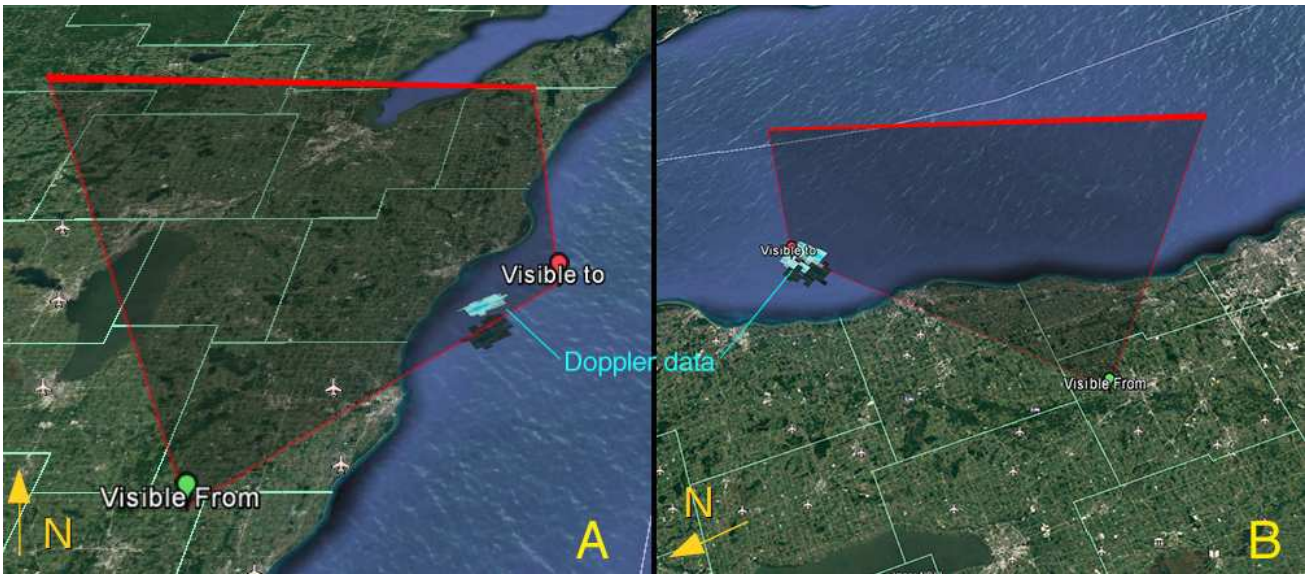

Figure 1 – Comparison between the trajectory obtained from all the 507 witness reports (A) with the trajectory obtained from the 140 reports submitted less than 4 hours after the event (B) and the Doppler data.

trates the importance of immediate reports.

2.4 Remarks

The coupling of a significant number of immediate eyewitness reports with Weather Doppler Radar records (or other sources such as video or radio records) allow to determine the time and approximate location of a meteorite fall. However, the wide variety of duration estimates collected by the IMO or the AMS and the impossibility to test the reliability of the witnesses having filled the on-line form prevent from fully evaluating the accuracy of the time perception of a fireball by a human being. It is also difficult to assess a comparison between visual and video observation of the same event if there is no certainty that the same part of the trajectory at the same limiting magnitude was detected. A correct evaluation of the time perception of a visual observer needs therefore to be performed by using a phenomenon with a perfectly known duration. This event must also be identically reproducible to produce results statistically meaningful. To meet these requirements, we have set up an experiment based on the creation of several fireball simulations.

3 Experiment

In order to analyze the accuracy of the time perception of different samples of population, we have created several animations representing a fireball in a night sky, whose duration is precisely known. Each animation is then presented to several people, respecting the following methodology:

s1 A person (subject) is asked to participate in a scientific experiment. If agreed, the person is asked to pay attention to a video before answering a question. No other information regarding what to expect is provided.

s2 After watching the video, the subject is asked to first guess the duration t_1 of the observed phenomenon (between the appearance and disappearance of the phenomenon), as well as the uncertainty Δt_1 such that the first duration guess t is $t = t_1 \pm \Delta t_1$.

s3 If the subject is not a specialist of meteors, (s)he is asked to describe the nature of the observed phenomenon. If the subject cannot answer, (s)he receives information regarding what was observed (meteor, fragmentation, meteor train, etc.).

s4 The subject watches the video again, after being told that (s)he will be asked again the same question. All subjects then immediately start to mentally count the number of seconds between the time the meteor appears and disappears. They do not count the number of seconds the meteor train is lasting.

s5 The subject provides a second guess of the duration of the phenomenon $t = t_2 \pm \Delta t_2$.

s6 The subject is asked if (s)he is used to sending meteor observation reports.

3.1 Simulations

Because the appearance of a fireball differs from one case to another, three different simulations were created for this experiment:

Sim1 is inspired by the Orgueil meteorite fall: the main body fragments into several pieces and explodes at the center of the field of view. A meteor train appears. The total duration of the fireball is 7 s. Several snapshots are provided in Figure 2.

Sim2 : same as Sim1 but faster and shorter. The fireball lasts 4.2 s.

Sim3 : Fast meteor without fragmentation. The fireball lasts 3.1 s. Several snapshots are provided in Figure 3.

The choice of different durations and characteristics (with or without fragmentation) of the simulations has been made to answer the questions q.4.c and q.4.d presented Section 1.

3.2 Sampled population

Sim1 was the most widely used simulation for the experiment, since it is closest to represent a meteorite fall. In order to analyze the influence of the knowledge degree in meteor science on the accuracy of the duration estimate (q.4.b), the simulation was presented to different population samples, defined as:

- Observing specialists: scientists or highly qualified amateurs, working in the field of meteors and regularly producing meteor observation reports (to e.g. IMO or to scientific journals).

- Non-observing specialists: scientists or highly qualified amateurs working in the field of meteors but not publishing observation reports.

- Scientists: astronomy scientists not working in the field of meteors.

- General Public: non scientific people, generally interested in science enough to participate to the experiment. This population was interviewed and tested in the galleries of the National Museum of Natural History in Paris, France, during their visit to the facility.

The three simulations were also presented to the public. In total, 576 individuals took the test. The distribution of the different populations is provided in Table 2. Each person was personally interviewed and tested by A. Egal (83% of the total population) and M.K. Kwon (17%).

Table 2 – The sampled population of people participating to the tests, as a function of the kind of simulation.

Population	Sim1	Sim2	Sim3
General Public	100	100	104
Scientists	123	—	—
Observing specialists	66	—	—
Non-observing specialists	83	—	—
Total specialists	*149*	—	—

4 Statistical analysis

4.1 Procedure

In this section, a statistical analysis of the whole distribution of the results obtained is performed. The duration estimates provided in step s2 (hereafter called "first guess", "first estimate" or "first video watching") and in step s4 ("second guess", "second estimate" or "second video watching") are globally analyzed for each population type (general public, scientists, non-observing specialists, observing specialists) and simulation type (Sim1, Sim2, and Sim3). No correlation between the accuracy of the first and the second duration estimate of a specific individual is taken into account. The size and the sign of the duration estimate errors provided by each sample of tested population is first presented using descriptive statistics, and then the effects of population type, simulation type and video watching are further investigated.

4.1.1 Measures

For all of the simulations, the fireball duration error was calculated for each participant as:

$$error = real\ duration - estimated\ duration.$$

The duration error can provide information about the size and the sign of the error; both these measures were taken separately for further analysis. The size of the error is measured in the following way:

1. In simulation 1, for comparisons of the estimated fireball durations taken from samples from 4 populations, we examine the absolute value of the error.

2. In simulations 1, 2 and 3, for comparisons of the estimated fireball durations from the general public, we examined the absolute error and the percentage relative error defined as:

$$relative\ error = 100\% \frac{absolute\ error}{duration}$$

The relative error percentage allow to compare the size of the error for the three different lengths of fireball duration in simulations 1, 2 and 3.

The sign of the error is defined as

$$sign = \begin{cases} \text{overestimated}, & error < -1.2, \\ \text{exact}, & -1.2 \leq error \leq 1.2, \\ \text{underestimated}, & error > 1.2 \end{cases} \quad (1)$$

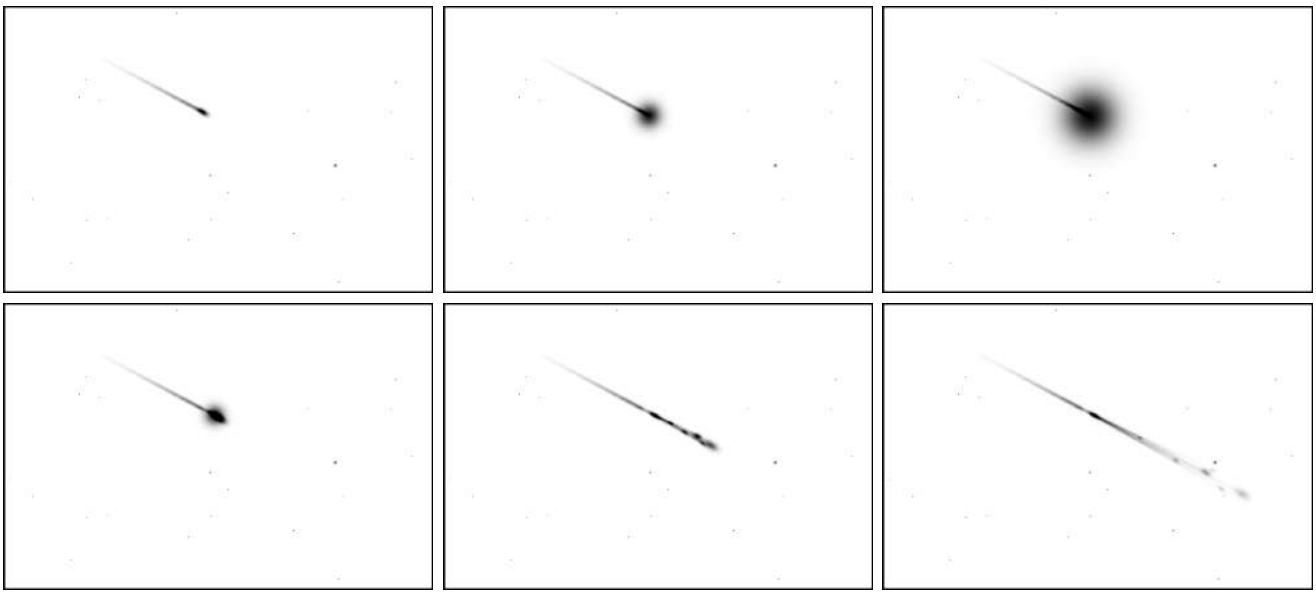

Figure 2 – Several snapshots of Sim1 (inverted colors) – fragmenting fireball.

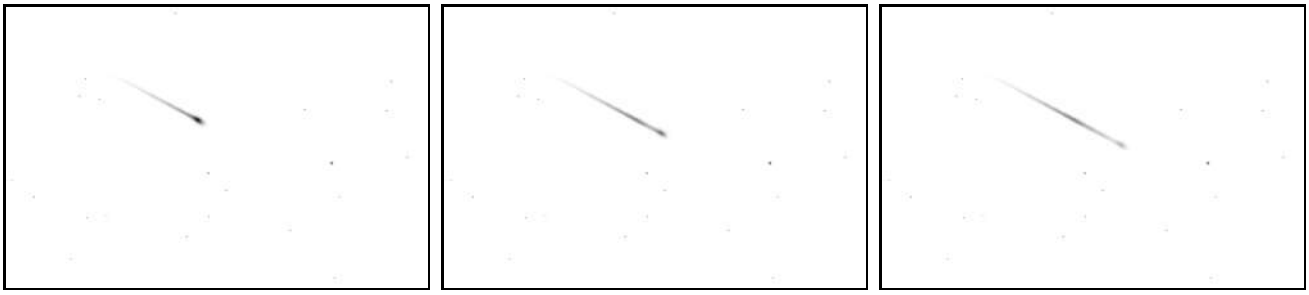

Figure 3 – Several snapshots of Sim3 (inverted colors) – not fragmenting fireball.

It was chosen that ±1.2 seconds above/under the fireball duration imply exactness of the fireball duration estimate, taking into account different lengths of three fireballs in simulations (7 s, 4.2 s, 3.1 s) and the fact that participants gave round seconds estimates. In the first simulation, 6 – 8 s estimate is considered exact, in the second simulation 3 – 5 s and 2 – 4 s in the third simulation.

We wanted to further disseminate the sign of the error into the separate analysis of presence of underestimated and presence of exactly estimated duration, denoted as dichotomous variables (0 - not present, 1 - present).

4.1.2 Research hypotheses

In this section, the following 6 hypotheses are tested:

1. The effects of the population type (general public, scientists, non-observing specialists, observing specialists), the video watching (first time, second time) and their interaction on the absolute duration error for simulation 1 are significant.

2. The effects of the population type, video watching and their interaction of the presence of an underestimated duration for simulation 1 are significant.

3. The effects of population type, video watching and their interaction on the presence of an exactly estimated duration for simulation 1 are significant.

4. The effects of the simulation type (simulation 1, 2, 3), video watching and their interaction on the percentage relative error of the fireball duration estimated by the general public are significant.

5. The effects of the simulation type, video watching and their interaction on the presence of an underestimated duration for the general public are significant.

6. The effects of the simulation type, video watching and their interaction on the presence of an exactly estimated duration for the general public are significant.

4.2 Descriptive statistics

The distribution of the absolute duration error, as well as the percentage relative error in simulations 1, 2 and 3, was analyzed with descriptive statistics (minimum, maximum, 1st quartile, median, 3rd quartile, mean rank) appropriate for asymmetric data. The distribution of the sign of the duration error is graphically represented with barplots and tables of frequencies and percentages.

4.2.1 Mean ranks

The distribution of the absolute duration error in simulation 1, as well as the distribution of the percent-

Table 3 – Summary statistics of the absolute detection error in simulations 1, 2 and 3 for the 1st and the 2nd video watching.

Group	Number	Min	Max	1.quartile	Median	3.quartile	Mean rank
Simulation 1							
General public							
1st video watching	100	0	43	2	3	4	464.6
2nd video watching	100	0	25	0.75	1	3	306.9
Scientists							
1st video watching	123	0	7	1	3	4	464.2
2nd video watching	123	0	7	1	1	2	274.5
Non-observing specialists							
1st video watching	83	0	6	1	3	4	431.2
2nd video watching	83	0	5	1	2	3	316.5
Observing specialists							
1st video watching	66	0	7	1	2	3	406.0
2nd video watching	66	0	6	1	2	3	307.3
Video watching							
1st time	372	0	43	2	3	4	441.5
2nd time	372	0	25	1	1	3	301.3
Simulation 2							
General public							
1st video watching	100	0.2	10.8	0.8	1.2	2.2	—
2nd video watching	100	0.2	5.8	0.8	0.8	1.8	—
Simulation 3							
General public							
1st video watching	104	0.1	16.9	0.1	0.9	1.9	—
2nd video watching	104	0.1	6.9	0.9	0.9	1.9	—

age relative error in simulations 1, 2 and 3, is not normal. The presence of underestimated and of exactly estimated duration are dichotomous variables. To analyze the effects of population type and video watching (or simulation type and video watching) on these variables, we rely on non-parametric mixed ANOVA (ANalysis Of VAriance) that compares the mean ranks of the groups. For example, when comparing the absolute duration error in simulation 1 for the 1st and the 2nd video watching, the mean rank is calculated in the following way: all of the 744 absolute duration errors in simulation 1 are sorted in increasing order and then ranked so that the smallest absolute error gets rank 1 and the greatest absolute error gets rank 744. Then, the mean rank for the 1st and the 2nd video watching is calculated by dividing the sum of the ranks for each video watching with the total number of absolute errors in that group (372 absolute errors for each video watching). The mean rank allows us to compare the distributions of the groups. An advantage of the ranking method is that it can be applied to various data types – continuous, discrete, ordinal, or even dichotomous.

4.2.2 Absolute duration error

Summary statistics (number, minimum, maximum, first and third quartile, median) of the absolute duration error in simulation 1 for all the people tested, as well as in simulations 2 and 3 for the general public, for the 1st and the 2nd video watching are presented in Table 3. For further comparisons of absolute errors, the mean ranks in simulation 1 are also provided.

If we look at the third quartiles in Table 3, we get the following results. In the first simulation, most of the data (87%) is in the range 0 – 4 s for the first video watching and in the 0 – 3 s range for the 2nd video watching (90%). This result are also valid for the general public. The mean ranks are calculated by first ranking the data from all participants in simulation 1, and then by averaging the ranks for each population type. In the second simulation, most of the data (85%) is in the interval [0 s, 2.2 s] for the first video watching and in the interval [0 s, 1.8 s] for the second video watching (82%). In the third simulation, most participants had absolute error in the interval [0 s, 1.9 s], 84% of them for the first video watching and 80% for the second video watching.

4.2.3 Relative duration error

Summary statistics (number, minimum, maximum, first and third quartile, median and mean rank) of the percentage relative error in simulations 1, 2 and 3 for the 1st and the 2nd video watching are presented in Table 4.

In the first simulation, 87% of participants of the general public had a percentage relative error of 57.1 and less (3 – 11 s duration estimate) for the first video watching and 90% participants had a percentage relative error of 42.9 and less (4 – 10 s duration estimate) for the second video watching. In the second simulation, 85% participants had a percentage relative error of 52.4 and less (2 – 6 s duration estimate) for the first video watching and 82% participants had a percentage relative error of 42.9 and less (3 – 6 s duration estimate)

Table 4 – Summary statistics of the percentage relative error for the general public in simulations 1, 2 and 3 for the 1st and in the 2nd video watching.

Group	Number	Min	Max	1.quartile	Median	3.quartile	Mean rank
Simulation 1							
1st video watching	100	0	614.3	28.6	42.9	57.1	347.56
2nd video watching	100	0	357.1	10.72	14.3	42.9	223.91
Simulation 2							
1st video watching	100	4.8	257.1	19	28.6	52.4	315.57
2nd video watching	100	4.8	138.1	19.0	19.0	42.9	271.75
Simulation 3							
1st video watching	104	3.2	545.2	3.2	29.0	61.3	299.93
2nd video watching	104	3.2	222.6	29.0	29.0	61.3	366.00
Video watching							
1st time	304	0	614.3	19.0	29.0	57.1	321.02
2nd time	304	0	357.1	14.3	28.6	42.9	287.22

for the second video watching. In the third simulation, a percentage relative error of 61.3 and less (2 – 5 s duration estimate) had 84% participants for the first video watching and 80% of them for the second video watching.

4.2.4 Sign of the duration error

The barplots of the sign of the duration error (hereafter called "sign") for 4 population types for the first and the second video watching are presented in Figure 4. For each video watching, on y-axis are represented the percentages within each population type and the overall percentage, for all of the participants (for example, the three "overall" bars obtained for the 1st video watching add up to the 100%). This also allows for visual comparisons between percentages of 4 population types for each category of the sign. Summary statistics (number, frequency and percentage) of the sign in simulation 1 for the 4 population types and the 1st and 2nd video watching are presented in Table 5. For the first video watching, almost 2/3 of the participants (66%) underestimated the fireball duration and 22% of the participants estimated it exactly (reported 6-8 seconds duration). For the second video watching, less than a 1/4 (23%) of participants underestimated and more than a half (54%) exactly estimated the fireball duration.

The barplots of the sign of the duration error for the general public in simulations 1, 2 and 3, for the first and the second video watching are presented in Figure 5 and summary statistics (number, frequency and percentage) in Table 6. For the first simulation, there is a big drop of the percentage of underestimated duration (57% in the first video, 11% in the second video watching) and a great rise of the percentage of exactly estimated duration (19% in the first video, 51% in the second video). Exactly estimated duration is the category with the greatest frequency in simulations 2 and 3 and it does not go through big changes when comparing the first and the second video watching. Whatever the simulation, we notice a general tendency in increasing the duration estimate for the 2nd video watching; the percentage of underestimated values decreases for the 2nd video watching, while the percentage of {exact + overestimated} durations increases (for a global better accuracy in case of simulations 1 & 2, and for a worse estimate in case of simulation 3).

4.3 Testing research hypotheses

After describing the error distributions obtained with the experiment, we investigate the truthfulness of the assumptions presented in Section 4.1.2.

4.3.1 Methods

The Brunner-Langer non-parametric mixed ANOVA method (Noguchi et al., 2012) was used for testing the significance of the effects of population type, video watching and their interaction on the absolute error, the presence of underestimated and of exactly estimated duration in simulation 1, and for testing the significance of the effects of simulation type, video watching and their interaction on the percentage relative error, the presence of underestimated and of exactly estimated duration in simulations 1, 2 and 3.

In a post-hoc analysis, significant interactions between the main effects were inspected in more detail, as it can override the main effects and, also, gives a more accurate picture of what is actually happening. Multiple comparisons between the absolute duration errors in simulation 1, as well as the relative error percentages in simulations 1, 2 and 3, for different groups was performed using the Brunner-Munzel test (Generalized Wilcoxon test) for independent samples (Brunner & Munzel, 2000) and the Munzel-Brunner exact rank test for paired samples (Munzel & Brunner, 2002). A posthoc analysis for the presence of underestimated and the presence of exactly estimated duration for the populations of simulation 1 and for simulations 1-3 was performed using one-sided exact McNemar test (Fay, 2010) for paired samples and Barnard test (Erguler, 2016) for independent samples. The probability of type I error was controlled using the Hochberg method (Wilcox, 2012).

P-values < 0.05 were considered statistically significant. The statistical analysis was performed in the statistical software R, version 3.4.2 (using packages nparLD, lawstat (Gastwirth et al., 2017), exact2x2 and Barnard (Erguler, 2016).

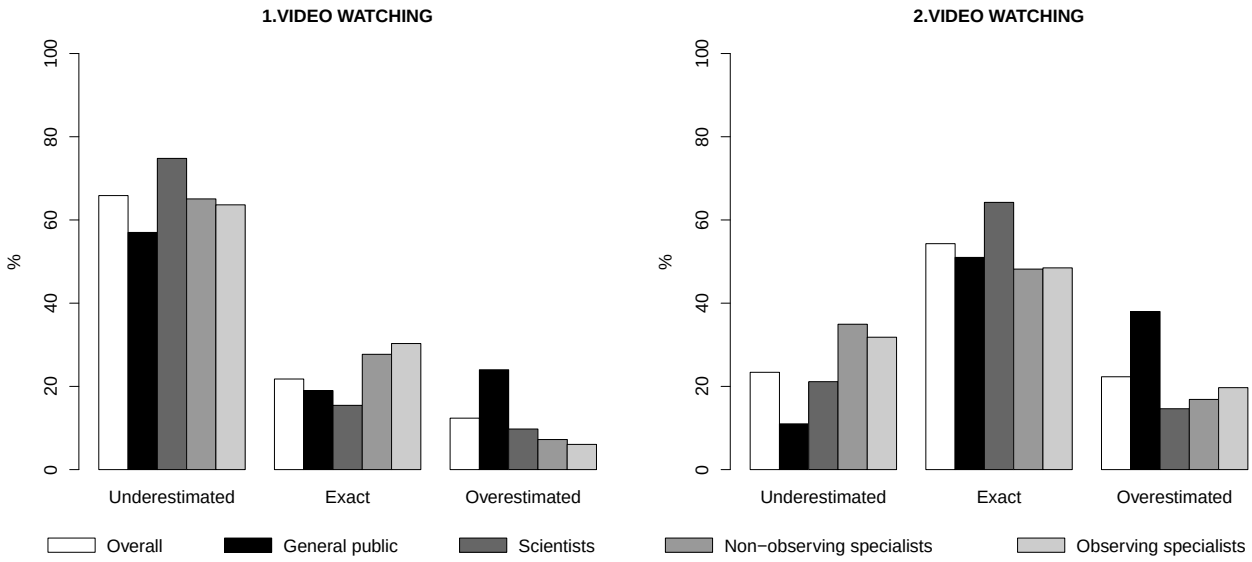

Figure 4 – Barplots of the sign of the duration error in simulation 1 for the 1st and the 2nd video watching.

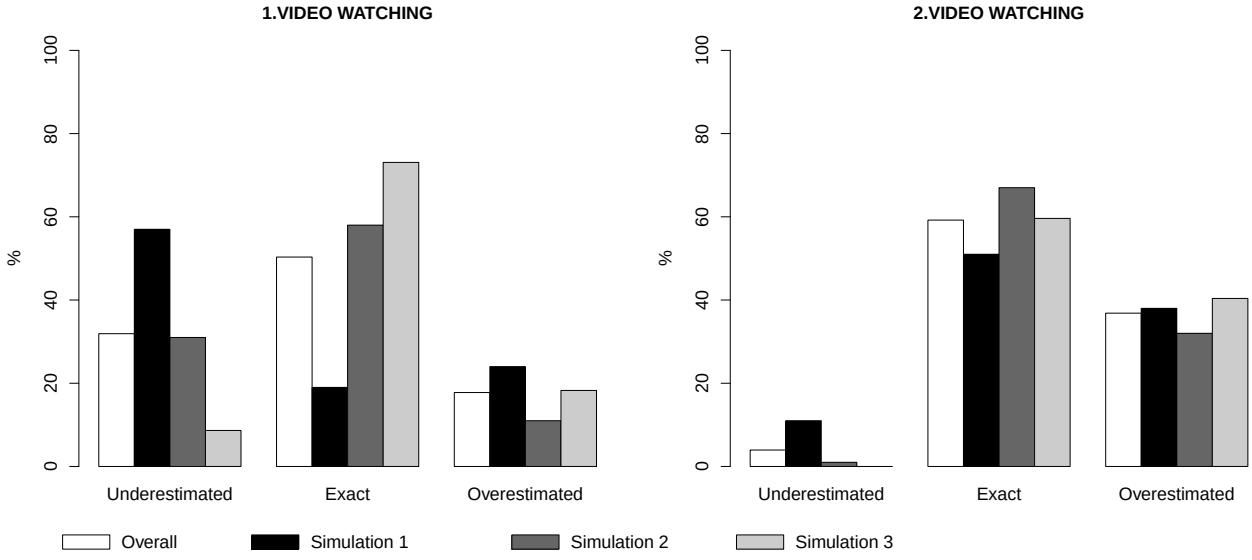

Figure 5 – Barplots of the sign of the duration error for the general public in simulations 1, 2 and 3 for the 1st and the 2nd video watching.

4.3.2 Sim 1: Effects of population type & video watching

Analysis of the absolute duration error

The Brunner-Langer mixed ANOVA showed that the effects of video watching (ANOVA type-statistic $F = 123.232$, $df_1 = 1$, $df_2 = +\infty$, $p < 0.001$) and the interaction between the population type and the video watching (ANOVA type-statistic $F = 2.679$, $df_1 = 2.98$, $df_2 = +\infty$, $p = 0.046$) on the absolute duration error in simulation 1 are statistically significant. The absolute duration errors of the 4 population types does not differ significantly. The mean rank of the absolute duration error for the first video watching is significantly higher than the mean rank of the absolute duration error for the second video watching (Table 3). In other words, the duration error is higher in the first video watching. A further inspection of the interaction will show for which population types this follows. It should be noted that ANOVA gives us only the result that the mean ranks for the first and the second video watching are significantly different, but the difference direction (smaller, greater) that we get in further analysis is much more useful in practice.

In post-hoc analysis, we therefore inspected a significant interaction between the population type and the video watching in more detail. We made 4 comparisons of the absolute error for the first and the second video watching for the 4 population types (Munzel-Brunner test for paired samples), 6 comparisons between the ab-

Table 5 – Summary statistics of sign of detection error in simulation 1 for the 1st and the 2nd video watching.

Group	Number	Underestimated N(%)	Exact N(%)	Overestimated N(%)
General public				
1st video watching	100	57 (57%)	19 (19%)	24 (24%)
2nd video watching	100	11 (11%)	51 (51%)	38 (38%)
Scientists				
1st video watching	123	92 (75%)	19 (15%)	12 (10%)
2nd video watching	123	26 (21%)	79 (64%)	18 (15%)
Non-observing specialists				
1st video watching	83	54 (65%)	23 (28%)	6 (7%)
2nd video watching	83	29 (35%)	40 (48%)	14 (17%)
Observing specialists				
1st video watching	66	42 (64%)	20 (30%)	4 (6%)
2nd video watching	66	21(32%)	32(48%)	13(20%)
Video watching				
1st time	372	245(66%)	81(22%)	46(12%)
2nd time	372	87 (23%)	202(54%)	83 (22%)

Table 6 – Summary statistics of sign of detection error for general public in simulations 1, 2 and 3 for the 1st and for the 2nd video watching.

Group General public	Number	Underestimated N(%)	Exact N(%)	Overestimated N(%)
Simulation 1				
1st video watching	100	57 (57%)	19 (19%)	24 (24%)
2nd video watching	100	11 (11%)	51 (51%)	38 (38%)
Simulation 2				
1st video watching	100	31 (31%)	58 (58%)	11 (11%)
2nd video watching	100	1 (1%)	67 (67%)	32 (32%)
Simulation 3				
1st video watching	104	9 (9%)	76 (73%)	19 (18%)
2nd video watching	104	0 (0%)	62 (60%)	42 (40%)
Video watching				
1st time	304	97(32%)	153(50%)	54(18%)
2nd time	304	12 (4%)	180(59%)	112 (37%)

solute errors of pairs of population types for the first video watching (Brunner-Munzel test for independent samples) and 6 comparisons between the absolute errors of pairs of population types for the second video watching (Brunner-Munzel test for independent samples). For the 4 comparisons within each population type in the video watching, we tested the hypothesis that the absolute error is higher for the first video watching than for the second video watching. Only comparisons between the absolute errors within each population type for the first and the second video watching were statistically significant: general public ($T = -6.384$, $df = 99$, $p < 0.001$), scientists ($T = -8.168$, $df = 122$, $p < 0.001$), non-observing specialists ($T = -4.787$, $df = 82$, $p < 0.001$), observing specialists ($T = -3.671$, $df = 65$, $p < 0.001$). In other words, for all of the population types, the absolute duration error is higher for the first video watching.

Underestimated & exactly estimated duration

The effects of population type, video watching and their interaction on the presence of underestimated duration are statistically significant. For each population type, a smaller number of participants underestimated the fireball duration for the second video watching. Further, for the first video watching, a greater percentage of scientists underestimated the fireball duration than the general public. For the second video watching, a smaller percentage of general public underestimated the fireball duration than the non-observing and observing specialists (for more details see Appendix 9.2.1).

The effects of the video watching and interactions of the population type and the video watching on the presence of exactly estimated duration are statistically significant. A greater number of general public, scientists and non-observing specialists exactly estimated the fireball duration for the second video watching than for the first video watching. There are no statistically significant differences between the presence of exactly estimated duration of the 4 population types for the first and for the second video watching (for more details see Appendix 9.2.2).

4.3.3 Sims 1, 2, 3: effects of simulation type & video watching

Analysis of the relative error percentage

The effects of simulation type, video watching and their interaction on the relative error percentage are statistically significant. For the second video watching, the relative error percentage significantly decreases in simulation 1 and in the simulation 2. For the first video watching, there is no significant difference between the relative error percentages in the simulations 1-3. The relative error percentage in the simulation 3 is significantly greater than in simulations 1 and 2, for the second video watching (more details can be found in Appendix 9.3.1). It should be noted that an analysis of the absolute error within each simulation type give the same results (as the relative error percentage contains the absolute error and applied statistical tests are based on the ranking method): there is a significant decrease of the absolute error in simulations 1 and 2 for the second video watching.

Underestimated & exactly estimated duration

The effects of simulation type, video watching and their interaction on the presence of underestimated duration are statistically significant. A smaller number of participants underestimated the fireball duration in simulation 1 and in the simulation 2 for the second video watching. For the first video watching, the greatest percentage of underestimated duration was present in the first simulation and the smallest in the third simulation. For the second video watching, a greater percentage of participants underestimated the fireball duration in simulation 1 than in simulations 2 and 3 (for more details see Appendix 9.3.2).

The effects of simulation type, video watching and their interaction on the presence of exactly estimated duration are statistically significant. A greater number of the participants exactly estimated the fireball duration in simulation 1 for the second video watching. For the first video watching, a smaller percentage of participants in the simulation 1 exactly estimated the fireball duration than in simulations 2 and 3. There are no significant differences between the presence of exactly estimated duration of simulation types in the second video watching (more details can be found in Appendix 9.3.3).

4.4 Recap of the statistical conclusions

The statistical analysis of the duration estimates provided by each sample of population tested for a given simulation and video watching highlighted the main following conclusions:

For the first simulation (long with fragmentation):

1. The majority of witnesses underestimated the real duration of the event at the 1st video watching. The number of underestimates decreases for the 2nd video watching. A greater number of the general public, the scientists and the non-observing specialists exactly estimated the duration in the 2nd video watching.

2. No statistical difference was noticed between the presence of exactly estimated duration for the 4 population types and the 1st and 2nd video watching. The absolute duration errors for the 4 population types does not differ significantly. However, the general public less underestimated the fireball duration than the scientists for the first video watching and than the specialists for the second video watching. In other words, no difference of accuracy in the duration estimate can be established in function of the degree of knowledge about meteor science, but the general public proved to have a smaller tendency to underestimate the duration than the specialists when counting the time.

Comparing simulations 1, 2 & 3:

3. For the first video watching there is no significant difference of the relative error percentage obtained for each simulation. The relative error does not depend on the length of the simulation when the witnesses guess the duration; the absolute error associated to a duration estimate therefore increases for long fireballs.

4. The higher number of exact durations is achieved for short simulations (2 & 3) in the first video watching. The higher number of underestimates is achieved for the long simulation (1) and the smallest for the shorter simulation (3) for the first video watching.

5. For the simulations presenting a fragmentation (Sim1 & Sim2, the absolute error and the relative error decreases for the 2nd video watching compared to the 1st video watching: the witnesses ready to count the duration were more accurate than the surprised ones. For the short simulation without fragmentation (Sim3), which presented a first guessed duration generally accurate, the second estimate determined by counting the time is worse than the guessed duration.

6. Whatever the simulation, there is a significant tendency in increasing the duration estimate between the first and the second video watching (for a better estimate in case of Sim1 & Sim2 and worse in case of Sim3). We can therefore expect that a witness having guessed the time will provide a smaller duration estimate than if he had counted the time.

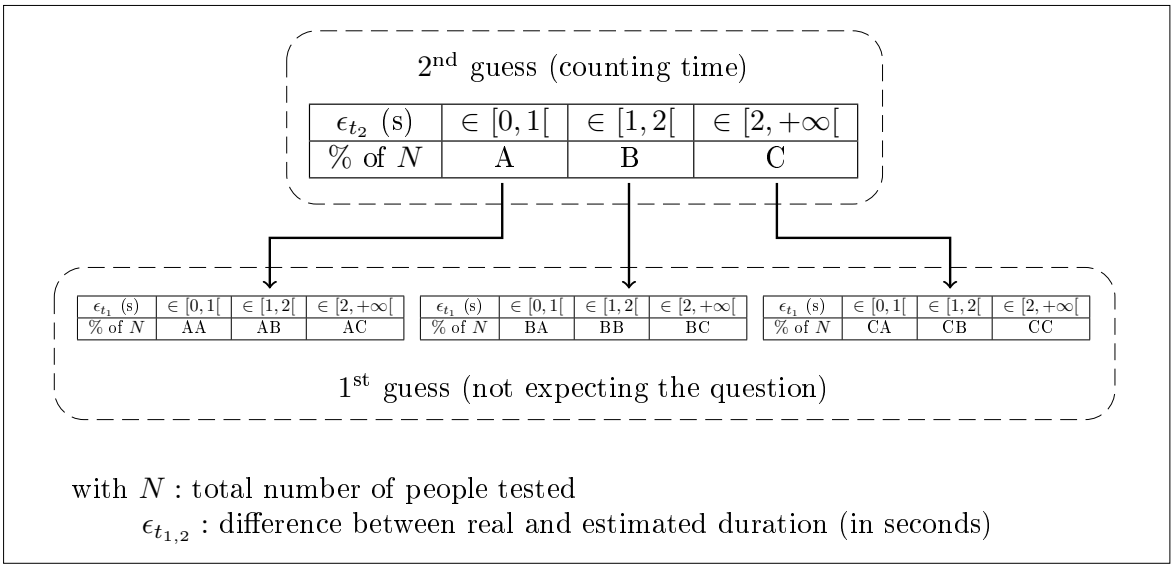

Figure 6 – Analysis of correct guess of the duration of the phenomenon, for a population of N members, for a single simulation.

5 Reliability of a small number of reports

The analysis performed above allows us to assess statistically reliable trends and conclusions on the accuracy of the time perception of a fireball when processing a large amount of duration estimates. By considering all the data available, no selection was made on the performance of the people tested (like for example retaining only the estimates of the witnesses able to accurately count a few seconds); the influence of the first video watching on the second one (and vice versa) was neglected.

In this section, we highlight the results obtained when the reliability of a witness is quantified. For the general public and each of the three simulations created, we first evaluate the ability of people to correctly count a duration of a few seconds without diverging. Depending on the accuracy of the counted duration, we then focus on the first duration estimate (by guessing) of each witness. If this methodology doesn't allow us to give a statistical sense to the ascertainments performed, it nonetheless allows us to illustrate the confidence we can grant on a small number of eyewitness reports.

5.1 Analysis procedure

In the following, the first guess of the duration provided by the subject at step s2 is denoted t_1, and the second estimate provided by the subject counting the duration at step s5 is denoted t_2. For the sample of population tested and a given simulation, we first evaluate the percentage of people able to correctly count the time (with a small error ϵ_{t_2}). The reason is that a witness W_u unable to correctly count the time cannot reliably provide us with the duration of the phenomenon. The first guess provided by such a witness W_u is of lower confidence than that provided by a witness W_a able to correctly count the time. Indeed, if a correct first guess is provided by W_u, it might just be a coincidence and should not be taken into account. We then compute the percentage of witnesses A, B and C who count the duration of the phenomenon with an error ϵ_{t_2} to the real duration respectively strictly smaller than 1 s, higher than 1 but strictly smaller than 2 seconds and greater or equal to 2 seconds. Such errors ϵ_{t_2} correspond to relative differences regarding the real duration of:

- 0% ($\epsilon_{t_2} < 1$ s), 14.3% ($\epsilon_{t_2} \in [1\text{ s}, 2\text{ s}[$), $\geq$ 28.6% ($\epsilon_{t_2} \geq 2$ s) for Sim1
- 0% ($\epsilon_{t_2} < 1$ s), 23.8% ($\epsilon_{t_2} \in [1\text{ s}, 2\text{ s}[$), $\geq$ 47.6% ($\epsilon_{t_2} \geq 2$ s) for Sim2
- 0% ($\epsilon_{t_2} < 1$ s), 32.3% ($\epsilon_{t_2} \in [1\text{ s}, 2\text{ s}[$), $\geq$ 64.5% ($\epsilon_{t_2} \geq 2$ s) for Sim3

Then for each subset of error, we look at the error ϵ_{t_1} provided for the first guess. Such an analysis is illustrated Figure 6. This lead to the following categories:

- A, B, C: % of people of the whole sample N having counted (2nd estimate) a correct duration of the phenomenon with an error $\epsilon_{t_2} < 1$ s (A), $\in [1\text{ s}, 2\text{ s}[$ (B) or ≥ 2 s (C)
- AA, AB, AC : % of people having counted (2nd estimate) a correct duration of the phenomenon with an error $\epsilon_{t_2} < 1$ s and provided a right 1st estimate of the duration with an error $\epsilon_{t_1} < 1$ s (AA), $\in [1\text{ s}, 2\text{ s}[$ (AB) or ≥ 2 s (AC)
- BA, BB, BC : % of people having counted (2nd estimate) a correct duration of the phenomenon with an error $\epsilon_{t_2} \in [1\text{ s}, 2\text{ s}[$ and provided a right 1st estimate of the duration with an error $\epsilon_{t_1} < 1$ s (BA), $\in [1\text{ s}, 2\text{ s}[$ (BB) or ≥ 2 s (BC)
- CA, CB, CC : % of people having counted (2nd estimate) a correct duration of the phenomenon with an error $\epsilon_{t_2} \geq 2$ s and provided a right 1st estimate of the duration with an error $\epsilon_{t_1} < 1$ s (CA), $\in [1\text{ s}, 2\text{ s}[$ (CB) or ≥ 2 s (CC)

Table 7 – % of the general public who provide a first and second estimate of the duration with the accuracy associated to the categories AA, AB, . . . , CC (cf. Figure 6) for the Sim1, Sim2 and Sim3.

Simulation	A	B	C	AA	AB	AC	BA	BB	BC	CA	CB	CC
1	25	26	49	1	5	19	2	5	19	3	3	**43**
2	52	30	18	15	16	**21**	8	13	9	6	4	8
3	55.7	23.1	21.2	**32.7**	18.3	4.8	10.6	9.6	2.9	12.5	3.8	4.8

5.2 Results for all simulations

Table 7 presents the percentage of correct guesses provided by the general public for the simulations 1, 2 & 3 and each category AA, AB, . . . , CC described in Figure 6.

For the first simulation representing a relatively long duration phenomenon (7 s), less than one person out of four was able to correctly count the time at better than one second (column A). Less than one out of twenty person was able to count and first guess the duration of the phenomenon with an accuracy of 1 s (column AB) and only 1% of the subjects was able to exactly count and guess the duration of the fireball (column AA). For the vast majority of cases, the error of the guessed duration is greater or equal to 2 s, which represents a $\sim$ 29% error. For almost all cases this 2 s error leads to an underestimated guess of the real duration of the phenomenon. The most probable guess deals with people unable to correctly count the time at better than 2 s, and providing a first guess that is at least within 2 s from the real duration (43% of all guesses, column labeled CC).

For a similar but shorter duration simulation ($\sim$ 4 s), we can see that there are twice as many people able to correctly measure the time better than 1 s: the human body internal clock is less prone to diverge from real time. As a natural consequence, the number of correct first guesses greatly increases, compared to Sim1. However, this number is not high enough to make this correct first guess the most probable one. The most probable guess is provided by people able to count the time, but whose first guess is at least 2 s off from the real duration (21% of all guesses, column AC).

For the short simulation without fragmentation (column AA), the results regarding the ability of the population to count the time correctly are similar to Sim2. However the most frequent guess is now provided by people able to correctly count the time and providing a first guess that is correct within a 1 s uncertainty (more than 30% of cases, column AA). Considering the entire dataset, we notice again that surprisingly the second guess is usually worse than the first one. This raises anew some questions regarding the reliability of visual witnesses.

6 Discussion

The large number of candidates interviewed should suffice to deduce statistical results related to the perception of time. However, the reliability of these findings depends on the presence of bias in the sample of the tested population. First of all, it should be checked that the samples chosen are sufficiently representative of a group of persons who would be likely to report the observation of a fireball to a scientific organism; but the composition of such a group is hard to pin down.

By its nature, this type of event is potentially observable by a wide variety of individuals, regardless of their age, gender, or education level. With the development of the communication media, it is also impossible to assume that only the persons with a marked interest to science would be able to transmit exploitable observation reports. Nowadays, a simple Internet article mentioning this type of event can give rise to a considerable number of testimonies from people who did not think of reporting their observations to organizations such as the IMO and the AMS. For example, the article about a fireball observed over France on 2016 August 6 at $22^{\rm h}07^{\rm m}$ UT described in the website of the amateur network REFORME allowed the IMO and the AMS to collect dozens of comments about this event, 20 of them which gave concrete information on the trajectory and the characteristics of the object. 5 of these witnesses estimated the duration of the phenomenon at "2 s" or "3–4 s"[c]. Thanks to this article, several people have filled and submitted a fireball report to the AMS and IMO.

Nowadays, the observation reports of fireballs can be written by any type of profile. For our experiment, we have then tried as much as possible to vary these parameters in the cases of the general public and the scientists. We questioned men, women, children, adults, elders, speaking French, English, Spanish, Italian or Portuguese. We made efforts to reach people interested enough in observational science to accept to be tested. We therefore hope not to have favored a certain type of profile for each category of assessed population.

In order to investigate the influence of the size of the screen on the result, the same simulation was shown to three groups of 50 subjects on a 10-inch, 17-inch screens and on one projection screen of several meters (format 16:9). No significant trends or differences were found in the responses for these three samples. No noticeable difference of results was detected between these formats. However, the use of different viewing supports induced the harmful disadvantage to cannot fully analyze the influence of the fragmentation in this work. Indeed, the simulations 2 and 3 were originally designed to present the same duration, in order to compare the time estimates in presence or not of a fragmentation. Unfortunately, the display of these simulations on different devices modified the effective duration of simulation 2,

[c] http://www.reforme-meteor.net/bolide-du-6-aout-2016-22h04-tu

passing from 3 s to 4.2 s and preventing any reliable analysis of the fragmentation influence on the accuracy of the time perception.

In this work, the presence of a significant underestimate of the fireball duration is investigated. Some previous studies (Goldstone et al., 1978; Fraisse, 1979) have found a correlation between the perceived duration of a luminous signal and its magnitude: larger stimuli are judged to last longer. Matthews et al. (2011) showed that the relative magnitude compared to the background rather than the absolute intensity of a stimulus is the primary determinant of its apparent duration. The duration estimate of a fireball observed during the day or the night should then slightly differ from one to another. However, all these studies were conducted for very short duration luminous signals (a few milliseconds), and were not extended to events lasting more than one second. The influence of the complexity of the observed signal was neither taken into account. To this day, we thus find no clue to predict a possible overestimate of the duration of a fireball because of its magnitude.

Because of the complexity of the topic, and considering that time perception depends strongly on psychological parameters of the witness, we do not claim here to provide robust results dealing with the accuracy of time duration guesses by a specific witness. However we believe this experiment highlights general tendencies of time perception and the systematic lack of reliable duration guesses. The first results highlighted in Section 2 seems to confirm these conclusions in the case of a real meteorite fall.

7 Conclusion & Future work

In this work, we have tried to estimate the accuracy of the time perception of a meteorite fall. Because of the complexity of comparing visual observations and video records of a specific fireball, we have set up an experiment based on the simulation of three fireballs of different and perfectly known characteristics (duration, presence of fragmentation, etc.). The simulations were presented to 576 persons in order to test the accuracy of their duration estimates; a first time, when the individuals were not expecting what to see and what will be asked, and a second time to allow the subjects to mentally count the duration of the phenomenon. The results obtained were overall analyzed by statistical tests, allowing to investigate the influence of the population type, the preparation of the individuals and the simulation duration on the accuracy of the time estimates. An illustration of the effective percentage of individuals able to either accurately count and guess the duration of the phenomenon is also presented, to help us understanding the confidence we can grant to a small number of visual observations.

From Section 5, we see that the effective percentage of reliable witnesses, able to either count and guess the duration of the simulated fireballs with an accuracy of 1 s or better (1% for Sim1, 15% for Sim2 and ∼32% for Sim3, cf. Table 7) prevents from assuming that the duration estimated by a small number of witnesses is accurate to one second close. A work similar to what is presented in Section 5 but taking into account the uncertainties associated with each duration estimate was performed, and lead to similar conclusions. However, this aspect could be deeply investigated in a future study.

From Section 4, we see that the accuracy of the duration estimate is worse when the subjects were not expecting what to see (first video watching) in the case of the simulations with fragmentation (simulations 1 & 2). The good accuracy achieved when guessing the duration of the short simulation without fragmentation (Sim3) is of reduced interest because of the worse performance of the witnesses when counting the time. These findings could be explained by the multiplicity of informations the witness has to process in simulations 1 & 2 (nature of the phenomenon, fragmentation etc.) resulting in a lower focus on the time duration. The model elaborated by Thomas & Weaver (1975) postulates that attention is divided between the estimation of duration and the information processing. Other studies (e.g. Fraisse (1979), Gil (2008)) confirmed that the less complex an observation is, the more attention a subject is able to give to the duration, resulting in a better time perception. However, a further analysis of the influence of fragmentation on the accuracy of the time perception should be made by reproducing this study on more data (simulations of exactly same duration, with and without fragmentation).

By comparing the duration estimates of different types of population (general public, scientists, non-observing specialists, observing specialists), no statistical evidence of a different accuracy of the time perception in function of the degree of knowledge about meteor science was found. In the case of a long phenomenon, the majority of witnesses underestimated the real duration of the phenomenon when guessing the time, whatever the population tested. However, the general public proved to have a smaller tendency to underestimate the duration than the specialists when counting the time. The total length of the simulations proved to have no significant impact on the relative error percentage when the subjects are guessing the duration after the first video watching. Therefore, the longer a fireball is, the greater the real error estimated on the duration will be (and the higher the impact on its velocity computation).

Whatever the simulation (i.e. the time length of the phenomenon), we notice a significant tendency in increasing the duration estimate between the first and the second video watching (for a better estimate in case of Sim1 & Sim2 and worse in case of Sim3). We can therefore expect that a witness having guessed the time will provide a smaller duration estimate than if he had counted the time.

In the case of a long fireball ($\geq$ 4 s), this tendency would lead to an underestimate of the real duration of the bolide. Moreover, we expect this misjudgment to be aggravated by the fact that it is highly unlikely that a witness of a real meteorite fall would focus on precisely counting the phenomenon duration (decreas-

ing the accuracy of its estimate) and by the "reaction" time required to notice the phenomenon and carefully look at it.

This study therefore highlight the necessity to consider the reliability of visual testimonies with great caution. Considering an accuracy of only one second on the duration of a fireball estimated by a few witness is far too optimistic, especially if the event is complex, spectacular, if the reliability of the witnesses cannot be evaluated and if the reports were harvested more than a few hours after the observation.

8 Acknowledgements

We are thankful to Brigitte Zanda and Sophie-Eve Valentin Joly for helping us gain access to the "Grande galerie de l'évolution" at the Muséum National d'Histoire Naturelle (MNHN, Paris) to conduct the tests with the public. We are also thankful to the 576 candidates that kindly accepted to take this test, and to have been so interested by the meteor science. This work was supported by grants from Region Ile-de-France (DIM-ACAV).

9 Appendix

The purpose of this appendix is to provide more information about the statistical analysis that led to the conclusions presented in Section 4. The terminology and the numerical results of the statistical tests performed are presented here in detail.

9.1 Definition of the statistical terms

The *null hypothesis* H_0 is the hypothesis that is being tested (Gibbons, 2010). The *alternative hypothesis* H_1 is the conclusion reached if the null hypothesis is rejected. A *statistical test* is a rule that enables us to make a decision whether the null hypothesis should be rejected on the basis of the value of a *test statistic*, which is some function of a sample. A *type I error* is committed if the null hypothesis is rejected when it is true (significance level, false positive result). We set it to 0.05. Knowing the distribution of a test statistic when the null hypothesis is true, we can calculate the *P-value*, *i.e.* the probability of obtaining a result equal to or more extreme than (in the direction of the alternative hypothesis) the value of the test statistics. If the P-value is smaller than 0.05 (significance level), we reject the null hypothesis and accept the alternative hypothesis.

In the non-parametric Brunner-Langer ANOVA method, the test statistics incorporates the mean ranks of the groups, as well as the group sample sizes and an estimate of the sample variability. The null hypothesis is that there are no differences between the groups (no significant effect of factor or factors), while the alternative hypothesis is that differences exist. Large values of test statistics lead to the rejection of the null hypothesis. Under the null hypothesis, the test statistics have a Fisher distribution with df_1 and df_2 degrees of freedom. They depend on the sample sizes and the number of groups and describe the shape of the Fisher distribution. For example, when testing the effects of the population type and the video watching on the presence of underestimated durations in simulation 1, we got that the value of the test statistics for the effect of population type is equal to $F = 3.529$, with $df_1 = 2.67$ and $df_2 = 249.47$ degrees of freedom. To illustrate how we calculate the P-value, we graphically represented a Fisher distribution with 2.67 and 249.47 degrees of freedom. The value of the test statistics is denoted on x-axis. The P-value is the probability (area under the density curve) of getting the value of test statistics and greater (Figure 7). It is equal to 0.019.

9.2 Simulation 1: Effects of population type & video watching

9.2.1 Presence of underestimated duration

The Brunner-Langer mixed ANOVA method showed that the effects of population type ($F = 3.529$, $df_1 = 2.67$, $df_2 = 249.47$, $p = 0.019$, the video watching ($F = 199.00$, $df_1 = 1$, $df_2 = +\infty$, $p < 0.001$) and their interaction ($F = 3.927$, $df_1 = 2.92$, $df_2 = +\infty$, $p = 0.009$) on the presence of underestimated duration are statistically significant. A significantly smaller number of participants underestimated the fireball duration for the second video watching than for the first video watching. A further analysis of the interaction of the main effects will show for which population types this follows.

In post-hoc analysis, we make the same comparisons as described for the absolute duration error. For comparisons between the presence of underestimated duration within each population type for the first and for the second video watching, we used one-sided exact McNemar test. For the comparisons between the presence of underestimated duration of pairs of population types for the first and for the second video watching, we used the Barnard test. For each population type, a smaller number of participants underestimated the fireball duration for the second video watching than for the first video watching: general public ($b = 1$, $c = 47$, $p < 0.001$), scientists ($b = 4$, $c = 70$, $p < 0.001$), non-observing specialists ($b = 5$, $c = 30$, $p < 0.001$), observing specialists ($b = 1$, $c = 22$, $p < 0.001$). For the first video, there is a significant difference between the presence of an underestimated duration of the general public and scientists (Score statistics $T = 2.807$, $p = 0.005$). A greater percentage of scientists underestimated the fireball duration. For the second video watching, there is statistical difference between the presence of the underestimated duration of the general public and the non-observing specialists (Score statistics $T = 3.901$, $p < 0.001$), the general public and the observing specialists (Score statistics $T = 3.328$, $p < 0.001$). A smaller percentage of the general public underestimated the fireball duration than the non-observing and observing specialists.

9.2.2 Presence of exactly estimated duration

The Brunner-Langer mixed ANOVA method showed that the effects of video watching ($F = 84.522$, $df_1 =$

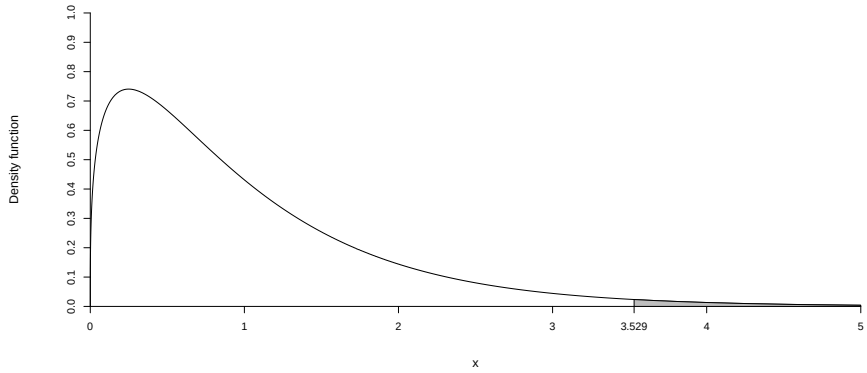

Figure 7 – P-value corresponding to the value of test statistics.

1, $df_2 = +\infty$, $p < 0.001$) and interaction of population type and video watching ($F = 4.636$, $df_1 = 2.86$, $df_2 = +\infty$, $p = 0.004$) on the presence of exactly estimated duration are statistically significant. There is no significant difference between the presence of exactly estimated duration of the 4 population types. A significantly greater number of participants exactly estimated the fireball duration for the second video watching than for the first video watching. A further inspection of the significant interaction of main effects will show for which population types this follows.

In post-hoc analysis, we make the same comparisons as described for the absolute duration error. For each population type, a greater number of participants of the following population types exactly estimated the fireball duration for the second video watching than for the first video watching: general public ($b = 38$, $c = 6$, $p < 0.001$), scientists ($b = 68$, $c = 8$, $p < 0.001$), non-observing specialists ($b = 25$, $c = 8$, $p = 0.002$). There are no statistically significant differences between the presence of exactly estimated duration of the 4 population types for the first and for the second video watching.

9.3 Simulation 1, 2, 3: Effects of simulation type & video watching

9.3.1 Analysis of the relative error percentage

Using the Brunner-Langer non-parametric mixed ANOVA method, we got that the effects of simulation type (modified ANOVA-type statistic with Box approximation $F = 4.431$, $df_1 = 1.98$, $df_2 = 296.05$, $p = 0.013$), video watching (ANOVA-type statistic $F = 6.241$, $df_1 = 1$, $df_2 = +\infty$, $p = 0.012$) and their interaction ($F = 16.520$, $df_1 = 1.98$, $df_2 = +\infty$, $p < 0.001$) on the relative error percentage are statistically significant. The percentage error for the second video watching is significantly smaller than for the first video watching. A further analysis of the interaction effect will show for which simulation types this follows.

In post-hoc analysis, we made 3 comparisons between the relative error percentages within each simulation type for the first and for the second video watching, 3 comparisons between the relative error percentages of all simulation types for the first video watching and 3 comparisons between the relative error percentages of all simulation types for the second video watching. For the 3 comparisons within the simulation types, we tested the hypothesis that the relative error percentage is higher for the first video watching than for the second video watching. For the second video watching, the mean rank significantly decreases in simulation 1 ($T = -6.384$, $df = 99$, $p < 0.001$) and in simulation 2 ($T = -2.441$, $df = 99$, $p = 0.008$). For the first video watching, there is no significant difference between the relative error percentages in the simulations 1-3. For the second video watching, there is a significant difference between the relative error percentage in simulations 1 and 3 ($T = 6.083$, $df = 200.48$, $p < 0.001$), simulations 2 and 3 ($T = 3.694$, $df = 195.84$, $p < 0.001$). The relative error percentage in the simulation 3 is significantly greater than in simulations 1 and 2.

9.3.2 Presence of underestimated duration

Using the Brunner-Langer non-parametric mixed ANOVA method, we got that the effects of simulation type (modified ANOVA-type statistic with Box approximation $F = 36.307$, $df_1 = 1.72$, $df_2 = 223.90$, $p < 0.001$), video watching (ANOVA-type statistic $F = 127.97$, $df_1 = 1$, $df_2 = +\infty$, $p = 0.012$) and their interaction ($F = 18.808$, $df_1 = 1.83$, $df_2 = +\infty$, $p < 0.001$) on the presence of underestimated duration are statistically significant. A significantly smaller number of participants underestimated the fireball duration for the second video watching than for the first video watching. A further analysis of the interaction effect will show for which simulation types this follows.

In post-hoc analysis, we made the same comparisons as described for the relative error percentage. For comparisons between the presence of underestimated duration within each simulation type for the first and for the second video watching, we used the one-sided exact McNemar test. For the comparisons between the presence of underestimated duration of pairs of simulation types for the first and for the second video watching, we used the Barnard test.

A smaller number of the participants underestimated the fireball duration in simulation 1 ($b = 1$, $c = 47$, $p < 0.001$) and in the simulation 2 ($b = 0$, $c = 30$, $p < 0.001$) for the second video watching. For the first video watching, there is a significant differ-

ence between the presence of underestimated duration in simulations 1 and 2 (Score statistics $T = -3.704$, $p < 0.001$), in simulations 1 and 3 (Score Statistics $T = -7.379$, $p < 0.001$) and in simulations 2 and 3 (Score statistics $T = -4.019$, $p < 0.001$). Of the three simulation types, the greatest percentage of underestimated duration was present in the first simulation and the smallest in the third simulation. For the second video watching, there is a significant difference between the presence of underestimated duration in simulations 1 and 2 (Score statistics $T = -2.977$, $p = 0.003$), in simulations 1 and 3 (Score statistics $T = -3.477$, $p < 0.001$). Comparisons between the presence of underestimated duration in simulations 2 and 3 were not possible because of the small frequencies obtained (1 and 0, respectively). A greater percentage of the participants underestimated the fireball duration in simulation 1 than in simulations 2 and 3.

9.3.3 Presence of exactly estimated duration

Using the Brunner-Langer non-parametric mixed ANOVA method, we got that the effects of simulation type (modified ANOVA-type statistic with Box approximation $F = 25.791$, $df_1 = 1.99$, $df_2 = 298.72$, $p < 0.001$), video watching (ANOVA-type statistic $F = 6.095$, $df_1 = 1$, $df_2 = +\infty$, $p = 0.014$) and their interaction ($F = 12.459$, $df_1 = 1.95$, $df_2 = +\infty$, $p < 0.001$) on the presence of exactly estimated duration are statistically significant. A significantly greater number of participants exactly estimated the fireball duration for the second video watching than for the first video watching. A further inspection of interaction effect will show for which simulation types this follows.

In post-hoc analysis, we made the same comparisons as described for the relative error percentage. A greater number of the participants exactly estimated the fireball duration in simulation 1 for the second video watching ($b = 38$, $c = 6$, $p < 0.001$). For the first video watching, there is a significant difference between the presence of exactly estimated duration in simulations 1 and 2 (Score statistics $T = 5.667$, $p < 0.001$), in simulations 1 and 3 (Score Statistics $T = 7.740$, $p < 0.001$). A smaller percentage of participants in the simulation 1 exactly estimated the fireball duration than in simulations 2 and 3. There are no significant differences between the presence of exactly estimated duration for the simulation types in the second video watching.

References

Andreic Z. (2012). "Dark flight calculations: how accurate can they be?". In *Proceedings of the International Meteor Conference, 30th IMC, Sibiu, Romania, 2011.* pages 23–28.

Brunner E. and Munzel U. (2000). "The nonparametric Behrens-Fisher problem: asymptotic theory and a small-sample approximation". *Biometrical Journal*, **42**, 17–25.

Emel'yanenko V. V., Popova O. P., Chugai N. N., Shelyakov M. A., Pakhomov Y. V., Shustov B. M., Shuvalov V. V., Biryukov E. E., Rybnov Y. S., Marov M. Y., Rykhlova L. V., Naroenkov S. A., Kartashova A. P., Kharlamov V. A., and Trubetskaya I. A. (2013). "Astronomical and physical aspects of the Chelyabinsk event (February 15, 2013)". *Solar System Research*, **47**, 240–254.

Erguler K. (2016). "Barnard: Barnard's Unconditional Test". R package version 1.8.

Fay M. P. (2010). "Two-sided Exact Tests and Matching Confidence Intervals for Discrete Data". *R Journal*, **2**, 53–58.

Fraisse P. (1979). "Perception and estimation of time". *Annual Review of Psychology*, **35**, 1–37.

Fries M., Le Corre L., Hankey M., Fries J., Matson R., Schaefer J., and Reddy V. (2014). "Detection and rapid recovery of the Sutter's Mill meteorite fall as a model for future recoveries worldwide". *Meteoritics and Planetary Science*, **49**, 1989–1996.

Gastwirth J. L., Gel Y. R., Wallace Hui W. L., Lyubchich V., Miao W., and Noguchi K. (2017). "lawstat: Tools for Biostatistics, Public Policy, and Law". R package version 3.1.

Gibbons, J. D. nd Chakraborti S. (2010). *Nonparametric Statistical Inference.* Chapman and Hall/CRC.

Gil S. (2008). "Perception du temps et émotions : étude de l'influence des expressions faciales émotionnelles chez l'enfant et l'adulte". Université Blaise Pascal - Clermont-Ferrand II, ED 0370, U.F.R. de Psychologie, Sciences Sociales et Sciences de l'Éducation.

Goldstone S., Lhamon W., and Sechzer J. (1978). "Light intensity and judged duration". *Bulletin of the Psychonomic Society*, **12:1**, 83–84.

Haack H., Grau T., Bischoff A., Horstmann M., Wasson J., Sørensen A., Laubenstein M., Ott U., Palme H., Gellissen M., Greenwood R. C., Pearson V. K., Franchi I. A., Gabelica Z., and Schmitt-Kopplin P. (2012). "Maribo - A new CM fall from Denmark". *Meteoritics and Planetary Science*, **47**, 30–50.

Hankey M. and Perlerin V. (2016). "A tale of two fireballs". In Roggemans P. and Roggemans A., editors, *Proceedings of the International Meteor Conference, Egmond, the Netherlands, 2-5 June 2016.* pages 111–112.

Hankey M., Perlerin V., R. L., and D. M. (2014). "American Meteor Society online fireball report". In Gyssens M., Roggemans P., and Zoladek P., editors, *Proceedings of the International Meteor Conference, Poznan, Poland, 22-25 August 2013.* pages 115–119.

Jenniskens P., Fries M. D., Yin Q.-Z., Zolensky M., Krot A. N., Sandford S. A., Sears D., Beauford R.,

Ebel D. S., Friedrich J. M., Nagashima K., Wimpenny J., Yamakawa A., Nishiizumi K., Hamajima Y., Caffee M. W., Welten K. C., Laubenstein M., Davis A. M., Simon S. B., Heck P. R., Young E. D., Kohl I. E., Thiemens M. H., Nunn M. H., Mikouchi T., Hagiya K., Ohsumi K., Cahill T. A., Lawton J. A., Barnes D., Steele A., Rochette P., Verosub K. L., Gattacceca J., Cooper G., Glavin D. P., Burton A. S., Dworkin J. P., Elsila J. E., Pizzarello S., Ogliore R., Schmitt-Kopplin P., Harir M., Hertkorn N., Verchovsky A., Grady M., Nagao K., Okazaki R., Takechi H., Hiroi T., Smith K., Silber E. A., Brown P. G., Albers J., Klotz D., Hankey M., Matson R., Fries J. A., Walker R. J., Puchtel I., Lee C.-T. A., Erdman M. E., Eppich G. R., Roeske S., Gabelica Z., Lerche M., Nuevo M., Girten B., and Worden S. P. (2012). "Radar-Enabled Recovery of the Sutterś Mill Meteorite, a Carbonaceous Chondrite Regolith Breccia". *Science*, **338**, 1583.

Matthews W., Stewart N., and Wearden J. (2011). "Stimulus intensity and the perception of duration". *J Exp Psychol Hum Percept Perform*, **37**, 303–13.

Moser D. E. (2017). "Comparing eyewitness-derived trajectories of bright meteors to instrumentally-observed data". *Planetary and Space Science*, **143**, 182–191.

Munzel U. and Brunner E. (2002). "An Exact Paired Rank Test". *Biometriical Journal*, **5**, 584–593.

Noguchi K., Gel Y. R., Brunner E., and Konietschke F. (2012). " nparLD: An R Software Package for the Nonparametric Analysis of Longitudinal Data in Factorial Experiments". *Journal of Statistical Software*, **50:12**, 1–23.

Olivier C. P. (1925). "The great meteor of May 11, 1922". *Popular Astronomy*, **33**, 502–503.

Perlerin V. (2017). "Green Fireball over Wisconsin: Citizen Science at Work". `https://www.amsmeteors.org/2017/02/green-fireball-over-wisconsin-citizen-science-at-work/`. Accessed: 2017-02-23.

Thomas E. and Weaver W. (1975). "Cognitive processing and time perception". *Perception and Psychophysics*, **17**, 363–367.

Wilcox R. (2012). *Introduction to Robust Estimation and Hypothesis Testing*. Elsevier.

Handling Editor: Javor Kac

This paper has been typeset from a LaTeX file prepared by the authors.

The Efficiency of Cameras for Video Meteor Observation – A theoretical contribution and a practical comparison between the Watec 120N+ and the Sony α7S

Peter C. Slansky[1]

In this article the author first makes a consideration of the theoretical background of the meteor detecting efficiency of video cameras and then presents a practical comparative test between an analog video camera and a digital photo camera with film function. The result of the practical camera test is strongly contradicting the theoretical consideration, so further research seems to be valuable.

Received 2017 November 26

1 Introduction

For meteor observation video cameras are widely in use based on analog technology with small monochrome CCD[a] sensors in Standard Definition, such as Watec or Mintron. "Standard Definition" (SD) means an analog resolution of 575 TV lines vertically, resulting in a resolution of 720 × 576 pixels when the signal is digitized in the European Television Standard respectively 720 × 480 pixels in the American Television Standard[b]. The first video cameras with CCD sensors were introduced in the analog television era in the late 1980s, so this technology is quite old fashioned. It is astonishing, how long it served well – and still does. The sensitivity of some of these video cameras is remarkably high, for example with only 0.0003 lux needed at F 1.4 for a Watec 902H to record a moving image.

But in the meantime television technology has advanced to digital and to High Definition with 1920 × 1080 Pixels ("Full HD"). Beyond that film and photo cameras with large CMOS[c] sensors are on the market with 30 million pixels or more and TV sets with Ultra High Definition with a resolution of 3840 × 2160 Pixels ("UHD") are available. There are digital photo cameras with film function with a sensitivity up to ISO 409 000, such as the Sony α7S or α7S II. Professional digital film cameras go up to ISO 4 000 000, such as the Canon ME20F-SH (Slansky, 2016). Although these impressive ISO values do not say anything about the image quality and especially not about the noise performance of these cameras, they are obviously interesting for meteor observation. And, obviously as well, they change our workflows.

So, how can we compare the meteor detecting efficiency of two cameras with different sensor technology, different sensor size, different pixel size, different resolution and different sensitivity?

To address this question the author first makes a short consideration of the theoretical background and then presents a practical comparative test between an analog video camera, a Watec 120N+, and a digital photo camera with film function, a Sony α7S[d]. This test was made in collaboration with Bernd Gährken alongside our Lyrids observation campaign on 2017 April 21/22 near Memmingen/Allgäu, Germany.

2 Meteor detecting efficiency

According to many authors (Hawkins, 1964; Sperberg, 2002; Rendtel, 2002) the effective meteor detecting efficiency is expressed by the following formula:

$$e \sim s_{\mathrm{ISO}} * \frac{d_{\mathrm{EP}}^2}{f} \qquad (1)$$

with e = meteor detecting efficiency, s_{ISO} = camera sensitivity according to ISO, d_{EP} = diameter of the entrance pupil of the lens, and f = focal length of the lens.

As can be seen, formula (1) does not represent an equation but a proportion. It consists of two parts: the opto-electronical efficiency, expressed by the ISO value of the camera, and the optical efficiency, expressed by the second term of formula (1): the diameter of the entrance pupil divided by the focal length of the lens.

As we will see, this approach is significantly incomplete, especially for the opto-electronical efficiency.

3 Sensitivity and noise

Digital photo cameras use the ISO value to express its sensitivity. This comes from the tradition of the photochemical film stock, for which the ISO value was defined. Video cameras are calibrated by a standard test chart with a certain reflectance, such as the "T 09" with a white field with 89.1% reflectance (Möllering & Slansky, 1993). The test chart has to be illuminated uniformly with a certain illuminance, 2000 lux for example. Gloss has to be avoided. Then the F-stop of the lens is adjusted in that way that for the white field the camera puts out a luminance signal with a level of 100%. For an analog video camera this means 1 V.

Both expressions of the sensitivity go back to the same roots. According to Möllering/Slansky (Möllering

[1]Hochschule für Fernsehen und Film München (University for Television and Film Munich, Germany).
Email: slansky@mnet-online.de

IMO bibcode WGN-461-slansky-cameras
NASA-ADS bibcode 2018JIMO...46...24S

[a]CCD: Charge coupled device

[b]The CCIR 601 Recommendation, also known as ITU BT.601, is based on an interlaced signal structure with odd and even fields and on a color subsampling of 4:2:2 with 720 samples per line for luminance (Y) and 360 samples per line for two color components (B-Y, R-Y). (Schmidt, 2013)

[c]CMOS: Complementary metal oxide semiconductor

[d]ILCE 7S, firmware version 3.20

& Slansky, 1993, p. 123) the interconnection can be calculated by the following formula:

$$s_{\mathrm{ISO}} = \frac{c_{\mathrm{ISO}} * F^2}{t * \frac{R}{100\%} * E} \qquad (2)$$

with s_{ISO} = camera sensitivity according to ISO, c_{ISO} = 228 lux s (ISO calibration factor), $F = F$-stop of the lens, t = exposure time [s], R = reflectance of the test chart [%], and E = illuminance of the test chart [lux].

As an example, the sensitivity of a video camera recording 50 fields per second (interlaced) with an integration time of 1/50 s with a test chart of 89.1% reflectance being illuminated with 2000 lux and the lens set to $F = 8.0$ resulting in a luminance signal level of 100% has a sensitivity equivalent to ISO 400.

As mentioned above, the ISO value does not tell anything about the image noise. So, for many video cameras the signal-to-noise ratio is indicated in decibel [dB]. Professional broadcast cameras have a signal-to-noise-ratio of 60 dB or higher when the camera is used at its native sensitivity. By the gain function the sensitivity can be increased (with some cameras also decreased). A step of +6 dB means a factor 2 for the sensitivity expressed in ISO. A positive or a negative gain also means that the signal-to-noise ratio is reduced or increased by the same amount (for cameras without active noise reduction). Theoretically any ISO value can be realized via signal amplification (gain), but the increasing of the noise provides a practical limit.

A big push for the sensitivity of modern cameras came with active noise reduction. Only by this, cameras like the Sony α7S or the Canon ME20F-SH achieve their extraordinary sensitivity. Three-dimensional noise reduction uses spatial and temporal image processing. By this the linear correlation between gain (respectively increasing the ISO value) and signal-to-noise ratio is suspended. But it introduces spatial and temporal image artefacts. This makes the comparison between a camera with active noise reduction and a camera without even more complicated.

4 Camera technology

The main advantage of CCD sensor technology is its comparably high sensitivity and the simplicity of the camera electronics. The main disadvantage of a CCD, designed for a video camera, is the limitation in size and resolution. The Watec 120N+, as well as the widely used Watec 902H2, has a 1/2" CCD sensor with a size of 6.4×4.8 mm and a native pixel count of $752 \times 582 = 440\,000$ pixels[e]. Each pixel has the size of 8.6×8.3 µm. The analog video signal of the camera according to the CCIR Standard 601 has to be digitized by a frame grabber. In our practical test a Matrox frame grabber card was used, providing an image resolution of 720×480 samples in the digital signal. (Hardware, such as sensors or displays, has pixels; a signal has samples.) On the sensor as well as in the image of the Watec the pixels respectively samples are non-square.

[e]CCIR version (Europe)

Interline transfer CCDs for video cameras are usually read out with odd and even fields ("interlaced") instead of full frames ("progressive"). In either case the information of each pixel has to pass the horizontal shift register. So, the outcome of a CCD sensor is a serial analog signal. Usually this serial analog signal is digitized by a single analog-to-digital converter instead of parallel processing. The Watec 120N+ provides two different read out modes of the interline CCD sensor: Field integration and frame integration. In field integration mode (with the shutter deactivated) the CCD is read out every 1/50 s with an alternation of odd and even fields, mixing the information of two lines of the pixels. The result is a loss of vertical resolution by the overlap of half a line from odd field to even field. But the temporal resolution is 50 fields per second. In frame integration mode the CCD is read out pixel line by pixel line with an integration time of 1/25 s each, but with an interval of 1/50 s between the odd and the even field. The result is the native vertical resolution of the sensor because no mixing of information of pixel lines is performed. The temporal resolution is still 50 fields per second but with a loss of temporal resolution by the longer exposure time.

In a CMOS sensor the pixels are organized in a two-dimensional readout design consisting of lines and columns. Each pixel has its own readout amplifier. This sensor structure makes it possible to read out only a part of the sensor. This "cropping" is done by most photo cameras when switched to film function with an aspect ratio of 16:9 for example. CMOS sensors are usually read out by full frames (progressive). Most digital film cameras and digital photo cameras with film function use one large CMOS sensor with a Bayer filter mask. So, digital film recording – instead of taking digital still photos – is done with a significant oversampling: The sensors have 1.5- to 2-times more pixels horizontally and vertically than samples in the signal. Oversampling does not mean binning: Oversampling is a real time down scaling done with complex algorithms. For this reason the scaling ratio is not limited to integer numbers such as 2:1 or 3:1 as with binning. Oversampling is also a mean to compensate the loss of resolution of a color sensor, compared to a monochrome sensor, caused by the Bayer mask: In a color sensor with a Bayer mask half of the sensor pixels are filtered in Green, a quarter in Red and another quarter in Blue. To reconstruct all three primaries for every sample of the signal, the native signal from the sensor has to be "de-bayered". For this, the information of two green filtered sensor pixels, one red and one blue sensor pixel are combined. In the brightness component of the signal this causes a loss of resolution of about 0.63-times of the sampled signal compared to the native sensor resolution, both horizontally and vertically. This loss can be compensated by an oversampling of 1.5-times more pixels horizontally and vertically. So, oversampling gives digital film cameras a smooth image and suppresses artifacts like aliasing or color aliasing. The oversampling ratio has to be taken for width and height, so a 2:1

Table 1 – Camera data

	Sony α7S 	Watec 120N+ 
Technology	Digital photo camera with film function	Analog video camera (CCIR 601)
Sensor type	Full format Bayer color CMOS	1/2" monochrome interline transfer CCD
Spectral sensitivity	400 nm – 640 nm (380 nm – 1100 nm with UV-/IR blocking filter removed)	380 nm – 1100 nm
Sensor size	35.6 mm × 23.8 mm (photo) 35.6 mm × 20.2 mm (film)	6.5 mm × 4.8 mm
Native sensor resolution	4240 × 2832 = 12 000 000 pixels	752 × 582 = 440 000 pixels
Native pixel size	8.4 µm × 8.4 µm = 71 µm^2	8.6 µm × 8.3 µm = 71 µm^2
Recording	1920 × 1080 = 2 070 000 samples (HD; internal) 3840 × 2160 = 8 280 000 samples (UHD; external)	720 × 480 = 415 000 samples (with Matrox frame grabber card)
Sample size	HD: 19 µm × 19 µm = 361 µm^2	8.6 µm × 8.3 µm = 71 µm^2
Oversampling	2.2-times	none
Maximum sensitivity	ISO 409 000	F 1.4, 256-times frame integration, Gain = +38 dB: 0.00002 lux
Contrast rendition	Rec.709: Gamma = 0.35, 0.45, 0.55; diverse Log curves	CCIR 601: Gamma = 0.35, 0.45, 1.0
Maximum contrast range	14 F-stops (= 16.000 : 1)	Less than 10 F-stops (= 1.000 : 1)
Frame rate(s)	25/30/50/60 frames per second (progressive, with 1920 × 1080 samples) 100/120 frames per second (progressive, with 1280 × 720 samples)	50 fields per second (interlaced)
Recording codec	Internal: XAVC-S	Depends on frame grabber
Maximum data rate	50 Mbit/s (internal)	Depends on frame grabber[f]
Price	∼ 2 000 €+ lens	∼ 710 €+ lens + computer + frame grabber
Information source	Sony Co. Ltd.: Technical specifications of the Sony a7S. `https://www.sony.com/electronics/interchangeable-lens-cameras/ilce-7s`	Watec Co., Ltd.: Data sheet of the Watec 120N+

over-sampling means four times more native pixels on the sensor than samples in the signal. It is obvious, that the application of a Bayer filter matrix and the use of oversampling have significant influence on the sensitivity, on the signal-to-noise ratio and on the resolution, so, on the limiting magnitude.

The Sony α7S has a color CMOS sensor with a native resolution of 4240 × 2832 pixels with a Bayer mask. In film mode the native signal from the sensor is debayered, cropped to 16:9 aspect ratio and downscaled by 1:2.2 in real time, resulting in a Full HD signal of 1920 × 1080 samples being recorded. This means an overall number of 12 000 000 pixels on the sensor but only 2 070 000 samples in the film image. Compared to other still photography cameras with up to 30 Megapixels or more this may sound mediocre, but Full HD resolution is five times the pixel number of SD video, as being provided by the Watec 120N+ (without oversampling).

Some authors[g] have reported a severe problem of the Sony Alpha series cameras, the so called "star eater issue": At longer exposure times the image processing eliminates stars, obviously mistaking them for hot pixels. These artefacts are introduced into the RAW data already, so its effect cannot be avoided. The Sony α7S (ILCE-7S) that was used in this test operated with firmware version 3.20 for which the star eater issue has not been reported for short exposure times as were used in film mode.

[f]Please note, that the frame grabber card that was used in this test did not reach the native vertical resolution of the Watec of 576 lines. Also, frame grabbers often have negative effects on the signal quality by the introduction of new artefacts such as jitter, noise, aliasing, quantisation artefacts or compression artefacts (Peterson, 2016).

[g]Please refer to `https://www.lonelyspeck.com/why-i-no-longer-recommend-sony-cameras-for-astrophotography-an-open-letter-to-sony/` and the authors mentioned at the bottom of the page.

5 Calculation of the ISO sensitivity of the Watec

As indicated by the manufacturer the Watec 120N+ needs a minimum illumination of 0.00002 lux at $F = 1.4$ and at the maximum gain of +38 dB with frame integration of 256 frames of 1/25 s. In frame integration mode the basic integration time is 1/25 s, being read out to 50 fields per second. At a frame integration of 256 frames the overall integration time is 1/25 s * 256 = 10.24 s. Inserting this number into formula (2) we get a maximum sensitivity for the Watec 120N+ equivalent to ISO 2 450 000[h]. This is 6 times of the sensitivity of the Sony α7S of ISO 409 000. According to formula (1) the meteor detecting efficiency based on the same area of the sensor should follow the same relation. But as the practical test shows, the effective meteor detection efficiency of the two cameras does not follow this theoretical consideration at all.

6 Considerations on a fair test setup

A first approach to a comparative test between two different cameras could be on the base of an identical field of view expressed in square degrees. In this case the optical efficiency of the lenses – the second part of formula (1) – would be part of the test. But it would be very difficult to make a fair choice of the two lenses: Due to the different sizes of the sensors for the same field of view the focal length for the Sony had to be 5 times longer than that for the Watec. For example, if we used a 10 mm lens on the Watec, we needed a 50 mm lens for the Sony to provide the same field of view. Meteors – like stars – can be considered as dots. According to formula (1) the limiting magnitude is proportional to the square of the diameter of the entrance pupil. If we chose lenses with an identical aperture – for example $F = 2.0$ – and for an identical field, this would mean an entry pupil of 25 mm diameter for the Sony but only 5 mm for the Watec. This would make the optical comparison for dot-shaped objects uneven by the factor $5^2 = 25$. On the other hand, an identical entrance pupil for both cameras and an identical field is unrealistic: If we took a 1.0/10 mm for the Watec, we would have to stop down a 50 mm lens for the Sony to 5.0. Nobody would do that. But even if we did it, the exposition of the sky background that is related to the F-stop would again be different by the factor 25.

To avoid this disparities caused by different lenses our camera test was made with the same lens on both cameras. This provides a constant optical output on the image plane, focusing the test entirely upon the opto-electronical efficiency of the cameras, but with different fields of view. Because of the consecutive change of the lens the test could only be made on stars but not on meteors.

[h]The result of this calculation was confirmed by Mr. Hiromitsu Kato, Watec, Ltd., although Watec use a slightly different calculation method.

7 Practical test setup

The test was done with a Canon FD 1.4/50 mm photo lens that could be adapted from Canon FD lens mount to Sony E-mount as well as to CS-mount for the Watec. Both cameras were set onto an equatorial mounting and pointed to Vega. The lens was stopped down to $F = 2.0$. Due to the identic focal length the sky region was reproduced to a constant area on the sensors of the two cameras. Because of its bigger sensor the field of view of the Sony was much larger than the field of view of the Watec. Taking into account that the Sony has an aspect ratio of 16:9 in film mode and the Watec 4:3, the factor of the image size is 5.

To provide an identic integration time the Sony was set to film mode with 25 frames per second (progressive) with 1/25 s integration time and the Watec 120N+ to frame integration mode, also with 1/25 s integration time, but being read out to 50 fields per second (interlaced). The analog interlaced signal of the Watec was digitized by a Matrox frame grabber with 25 frames per second progressive. Also very important for equal test conditions was the setting of the gamma, the contrast rendition function: According to CCIR 601 respectively ITU Rec.709 the gamma was set to 0.45 in both cameras.

In postproduction the image of the Sony was cropped exactly to the image field of the Watec. For the presentation in print media and still images the following processing was done with a consistent workflow: 100 frames were combined with the median function. This is appropriate to the visual experience of a video sequence and the averaging effect of the human eye with noise in the image running at 25 frames per second. The contrast rendition curve was elevated in exactly the same way by an identic gamma shift to show more detail in the blacks. The pixels of the cameras have nearly exactly the same size, but in film mode the Sony operates with a 2.2-times downscaling. So, for the comparison the image of the Sony had to be scaled up by the factor 2.2 before cropping. By this the image of the Sony has only 0.45 times the resolution of the image of the Watec at an identic field of view. This can be seen in Figure 1 by the larger diameter of the stars, i.e. Vega.

The spectral sensitivity of monochrome silicon sensors as the sensor of the Watec goes from 380 nm up to 1100 nm. For color sensors this range has to be reduced to the visual spectra by a UV-/IR blocking filter. Because the original UV-/IR blocking filter of the Sony α7S also blocks Hα, I had let it be removed. By this my α7S is also sensitive from 390 nm to the near infrared up to 1100 nm. So it was tested in two different conditions: In "VIS mode" the lens was provided with an external "UVI" UV-/IR blocking filter by Makario Optic and the camera was set to color mode in the camera menu. In "VIS+NIR mode", no UV-/IR blocking filter was used and the camera was set to black and white mode. The latter was providing a very similar spectral sensitivity as that of the Watec. In theory the Sony should have about 2.5-times the overall sensitivity without the blocking filter than with the filter (for energy equal radiation). Also the image noise was to be

expected significantly less in b & w mode than in color mode because a specific part of the image noise results from color noise. But surprisingly the results of the test did not show these differences.

The stellar limiting magnitudes of the three images – Sony α7S VIS color, Sony α7S VIS+NIR b & w and Watec 120N+ VIS+NIR b & w – were determined by visual star counting in the image field compared to star counts in a set of star charts from a planetary program. The Watec shows less statistical noise, but more fixed pattern noise that obviously comes from the structure of the CCD. The Sony shows more over all noise. As shown in Table 2, the star counting in the processed composite images was done twice for each camera: The first time "modestly" by counting apparent stars in the image, the second time "optimistically" by blinking with the star chart and verifying every star in the image that should be there according to the star chart. For the result the "modest" star counting is expected to be significant: Of course, stars are easier to detect, when you know where they should appear. Interestingly the difference between the modest and the optimistic star count is remarkably bigger for the Watec than for the Sony, as well in "VIS" mode as in "VIS+NIR" mode. In order to avoid a numeric fake precision, the limiting magnitude was rounded off.

8 The difference in field of view

As mentioned before, the Sony has a sensor that provides a 16:9 aspect ratio in film mode with an active area of 35.6 mm × 20.2 mm. The Watec has a sensor with 4:3 aspect ratio and an active area of 6.5 mm × 4.8 mm. With a 50 mm lens the field view of the Sony is $39\overset{\circ}{.}2 \times 22\overset{\circ}{.}8 = 894(^\circ)^2$, the field of the Watec is $7\overset{\circ}{.}44 \times 5\overset{\circ}{.}5 = 41(^\circ)^2$. So, with a 50 mm lens the Sony covers a sky region 22 times wider in square degrees than the Watec.

9 Interpretation

The test result shows that the Sony α7S reveals a slightly higher stellar limiting magnitude with the same lens as the Watec 120N+. Interestingly this is nearly independent from the usage of the UV-/IR-blocking filter (VIS mode or VIS+NIR mode). One reason for this could be the better focus with the UV-/IR-blocking filter due to chromatic aberrations of the lens in NIR. Another reason might be the fact that in a color image a faint white star can be separated better from the color-noisy background than in a black & white image.

The difference of the stellar limiting magnitude between 8.6 mag and 8.3 mag expresses a difference in the opto-electronical efficiency of 0.3 mag. This means, that the Sony α7S in VIS mode is $2.5^{0.3} = 1.316$ times as sensitive as the Watec 120N+ on the identic field of the sensor. If we assume that the meteor limiting magnitude is equivalent to the stellar limiting magnitude, the following calculation can be made: With a (hypothetical) population index of 2.5 the difference in opto-electronical efficiency of 0.3 mag means that the Sony detects 1.316 times more meteors than the Watec on the identic field of the sensor. But the sensor of the Sony is much larger than that of the Watec, covering a 22 times wider part of the sky in square degrees. So, assuming a homogenous spread of the meteors over the sky, the Sony should detect 29 times more meteors than the Watec – with a 50 mm lens without any loss of the optical performance from the center to the corner of the image. For the Sony in VIS+NIR mode the result is even slightly better.

This test results are in direct contradiction to the theoretical comparison of the meteor detecting efficiency equivalent to the ISO sensitivity of the two cameras: ISO 2 450 000 for the Watec versus ISO 409 000 for the Sony (in VIS mode). So, further research seems to be valuable. The author is grateful for any comment.

Acknowledgements

The author wants to thank Bernd Gährken for his very supportive collaboration and Hiromitsu Kato, Watec Co., Ltd., for his very valuable technical information.

References

Hawkins G. S. (1964). *The Physics and Astronomy of Meteors, Comets and Meteorites*. McGraw-Hill.

Möllering D. and Slansky P. C. (1993). *Handbuch der Professionellen Videoaufnahme*. Edition Filmwerkstatt, Essen.

Peterson C. (2016). "Evaluating video digitizer errors". In Roggemans A. and Roggemans P., editors, *International Meteor Conference Egmond, the Netherlands, 2-5 June 2016*. IMO, pages 214–216.

Rendtel J. (2002). *Handbook for Photographic Meteor Observations*. IMO Monograph No. 3.

Schmidt U. (2013). *Professionelle Videotechnik*. Springer Verlag.

Slansky P. C. (2016). "Meteor film recording with digital film cameras with large CMOS sensors". *WGN, Journal of the IMO*, **44:6**, 190–197.

Sperberg U. (2002). "Fotografische Meteorbeobachtung – eine kurze Einführung". *VdS Journal für Astronomie*, **I**, 57–60.

Handling Editor: Javor Kac

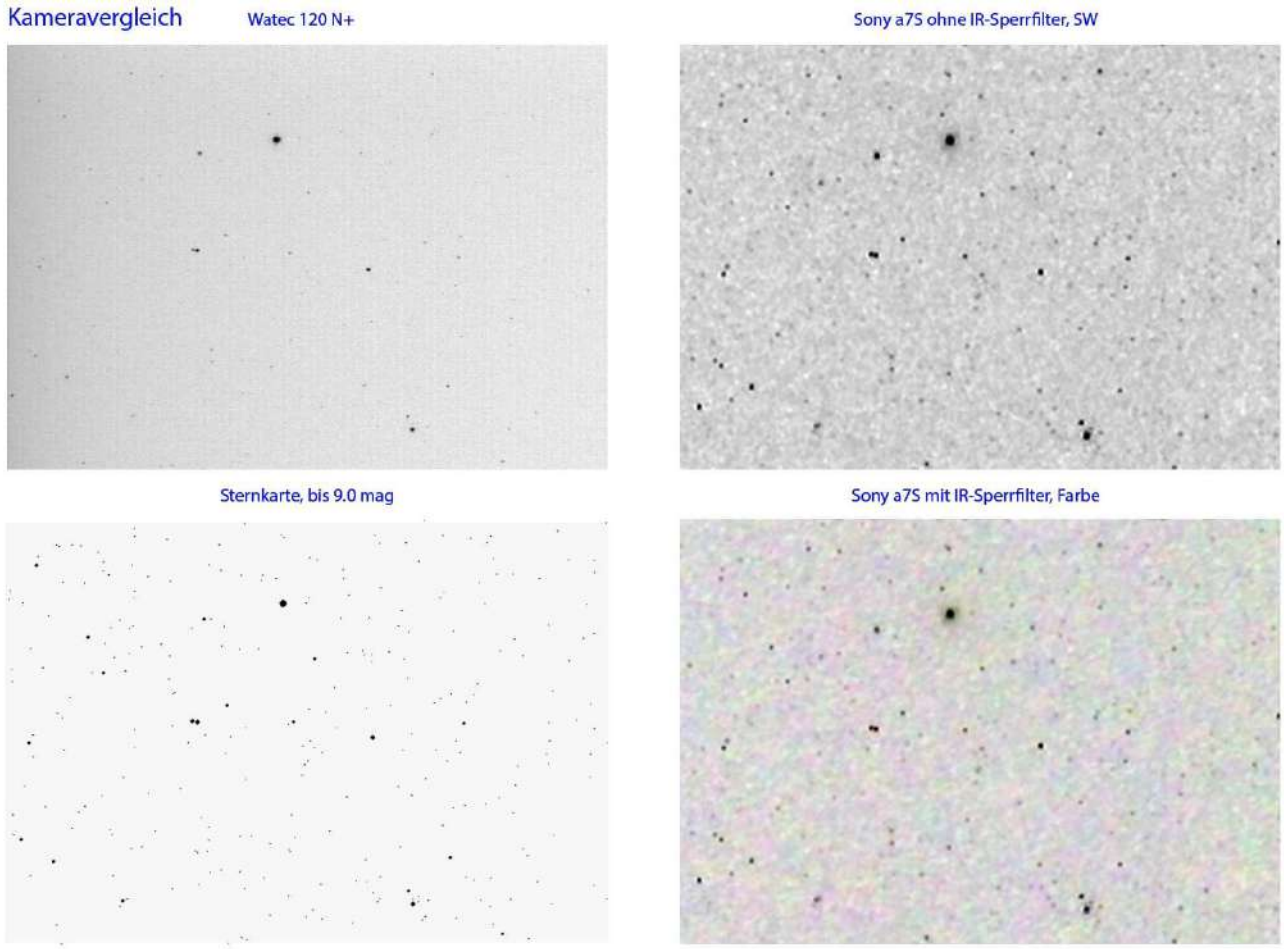

Figure 1 – Camera comparison of the resulting stellar limiting magnitude, lens Canon FD 1.4/50 mm, $F = 2.0$. Watec settings: AGC: High, gamma = 0.35, 50 fields per second (interlaced). Sony settings: ISO 409 000, 25 frames per second (progressive). Each image (except the star chart) is a composite of 100 frames integrated with a median function. The bright star is Vega, mag 0. Bottom left: Star chart with stellar limiting magnitude 9.0 mag. Top left: Watec 120N+ showing a stellar limiting magnitude 8.3 mag (modest star counting). Top right: Sony α7S VIS+NIR without UV-/IR-blocking filter in black & white mode showing a stellar limiting magnitude 8.7 mag (modest star counting). Bottom right: Sony α7S with UV-/IR-blocking filter VIS in color mode showing a stellar limiting magnitude 8.6 mag.

(Please note that the resolution of Figure 1 in this article is reduced. The star counting as detailed in Table 2 was done in the unreversed images. Refer to `http://www.peter-slansky.de/bereiche/astronomie/aufnahmetechniken/aufnahmetechniken13h.html`.)

Table 2 – Result of star counting in Figure 1.

Star chart	8.3 mag	8.4 mag	8.5 mag	8.6 mag	8.7 mag	8.8 mag
Stars in the field	111	123	142	173	200	237
Camera image	Watec “modest”	Watec “optimistic”	Sony VIS “modest”	Sony VIS “optimistic”	Sony VIS+NIR “modest”	Sony VIS+NIR “optimistic”
Stars in the field	109	155	184	219	199	213
Limiting magnitude	8.3 mag	8.55 mag	8.6 mag	8.75 mag	8.7 mag	8.75 mag

Polish Fireball Network: Video Meteor Astrometry

M. Wiśniewski[1,2], *P. Żołądek*[1], *A. Olech*[1,2], *W. Jonderko*[1]

The Polish Fireball Network (PFN) is a network of meteor-observing stations spread over the territory of Poland. In 2008 the network consisted of 13 stations, where 24 non-intensified video cameras along with 3 digital photo cameras operated each night. Most of PFN observers are amateurs, members of the Comets and Meteors Workshop, who perform observations from their homes.
The MetRec software was used for meteor detection. To obtain the highest possible accuracy for meteor astrometry and trajectory estimation, we have invented a method using an automatic identification of background stars, that are then combined from multiple mean images collected through the night, associated to a catalog, and collectively fit to an astrometric model. We developed the software to focus on combining those stars appearing in the mean images associated with detected meteors. An accuracy of 3 arcminutes across nearly the whole image was achieved.

Received 2018 February 8

Editor's Note:
This article was meant for the IMC 2008 proceedings that got lost, but has been requested to be referenced numerous times, so is being published officially in WGN at this time.

1 Introduction

Since 2004, the Polish sky has been patrolled by the Polish Fireball Network of cameras. The first double-station observations using video cameras were made during the Leonids maximum in 2003. PFN started in March 2004 with 3 continuously operating video stations in Ostrowik (PFN01), Złotokłos (PFN03) and Poznań (PFN05). First results from PFN for the brightest fireballs were recently presented (Spurný et al., 2004; Żołądek et al., 2007).

Most of the PFN observers are amateurs and members of the Comets and Meteors Workshop. Some cameras belong to the PFN, others have been purchased from observer's own funds. Most observations are performed from observer's houses. Some stations are installed in astronomical clubs and schools. The project involves the Warsaw University Astronomical Observatory (OAUW), the Nicolaus Copernicus Astronomical Center (NCAC) and the Astronomical Institute at the University of Zielona Gora. The PFN project was also supported by Siemens Building Technologies. The network consists of 13 continuously working stations where 24 video cameras and 3 digital photo cameras operate. A map of the PFN is shown in Figure 1.

The sensitive CCTV video cameras from Mintron, Siemens, Tayama and Fucho are used. The lenses that meet the quality required to conduct meteor observations were selected during the lens test (Wiśniewski et al., 2005). The best results were obtained for the Ernitec and Computar lenses. All cameras were equipped with CCTV lenses with a focal length $f = 4$ mm and $F = 1.2$ which gives approximately a 65×49 degrees field of view.

Figure 1 – Location of Polish Fireball Network stations. Stations which operate occasionally or stopped working were plotted with open circles.

For meteor detection the MetRec software written by Sirko Molau (Molau, 1999) has been used. About half of the cameras record images at full PAL resolution (768×576), the rest of them still work in half-resolution (384×288). This means the image resolution is approx. 5 arc minutes and 10 arc minutes per pixel for full and half-resolution images, respectively. Limiting magnitude is about magnitude 4 for stars and about second magnitude for meteors. In the years 2004–2007 the video cameras of the PFN performed more than 40 thousand hours of observations and collected nearly 60 thousand meteors.

2 RecoStar software package – for astrometry on video images

The main problem that we faced when analyzing PFN video data was the low sensitivity of the cameras. We were able to find only a few reference stars when

[1]Comets and Meteors Workshop, Bartycka 18, 00-716 Warszawa, Poland
[2]Nicolaus Copernicus Astronomical Center, Polish Academy of Sciences, Bartycka 18 00-716 Warszawa, Poland. Email: marand.w@gmail.com

IMO bibcode WGN-461-wisniewski-pfn
NASA-ADS bibcode 2018JIMO...46...30W

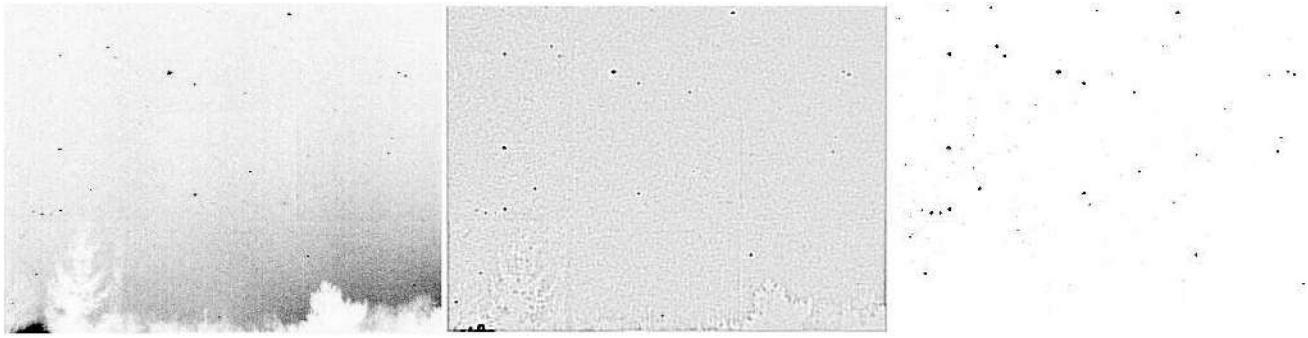

Figure 2 – Example of mean image, filtered image and map of the detected bright pixels.

searching on single images of the sky from the deployed cameras. There were not enough stars to fit the astrometry to sufficient accuracy to perform good quality trajectory calculations from two-station observations.

A special software package called sc RecoStar was created to obtain precise coordinates of the meteor tracks. The package allows you to automatically detect and identify stars on images from PFN cameras. The task of the package is to determine the coordinate transformation to convert the position of meteors in the image into equatorial coordinates. It consists of several programs working sequentially in a pipeline.

2.1 RecoMean

MetRec MetRec records, in 8-bit BMP format, all frames containing the meteor's passage and several frames before and after the meteor detection. For long events, there may be several tens of images. The program RecoMean calculates the average image of the star-filled background, from all individual frames. When computing the average brightness of a pixel the brightest measurement of all frames is ignored. This brightest measurement usually belongs to the meteor event. In this way we remove the contamination of the meteor from the average image. Only for meteors with a persistent train is there left behind a weak remnant in the average.

Detection of stars on the mean image is also conducted by RecoMean. The averaged image is sharpened using a Gaussian filter with a half-width similar to the point spread function which exists for the stars in the image. In this way we remove a background image and leave only objects that differ from the local background. Points that exceed the detection threshold are identified as potential stars.

The average image is saved as BMP file in the format of $15 + 1$ bits where 15-bit are used to represent the average image and the 1-bit map stores information about pixels recognized as belonging to stars or background. Calculating a multi-frame average image allows you to find weaker stars and improve the quality of the photometry. An example of mean images are shown on Figure 2.

2.2 RecoStar

The RecoStar software automatically recognizes stars on the mean images. Each average picture is examined individually. The program can also recognize the size of the camera's field of view, but these are time-consuming calculations. During identification we compare positions of detected stars on the image with coordinates from the Bright Star Catalog (BSC) (Hoffleit, 1964).

The algorithm of star identification is based on a method that calculates and compares the distances between stars on the image and in the star catalog. The search of similarities is based not on pairs but on triangles from stars. When the program is executed, a database of all possible triangles generated from groups of 3 stars from the catalog is created. A pre-computed database of all possible triangles speeds up the process of comparing the triangles found on the average image. The database of all possible triangles is created only once. We assume that all images for the astrometry estimation in one run of the program comes from one camera, and the size of the field of view doesn't change.

The size of the catalog of possible triangles is reduced with additional filters. The first filter is removing triangles with sides larger than field of view (too big to find). The second one is removing shorter than one tenth of the field of view (too small for our resolution), and finally check if the sides of the triangle differed significantly from each other (hard to distinguish which side is which). The last test allows us to determine which of the sides in the image correspond to the sides of the triangle identified in the catalog.

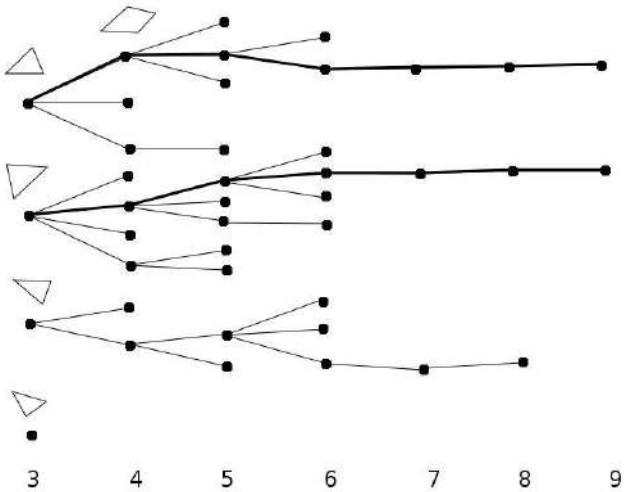

Figure 3 – Selection of best maching list of stars.

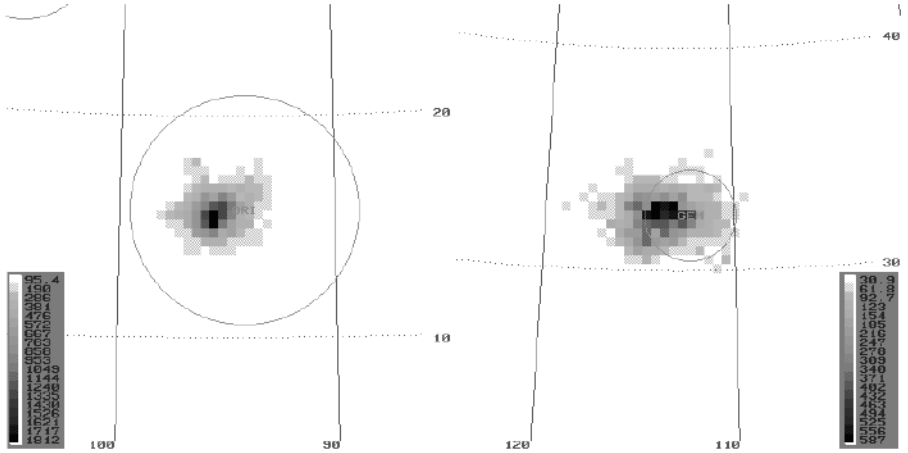

Figure 4 – Maps of possible position of radiant of Orionids (ORI) and Geminids (GEM) from single-station data. For all calculations we use the Intersections method in the Radiant software with pixel size of 0.4 degree. A number of crossings between meteors are outlined.

The process of identification of stars on each image starts from the creation of a list of all visible triangles. Then triangles from the mean image are matched with possible triangles from the catalog. Often, many triangles from the catalog match one triangle in the image. The best aligned triangles are chosen from those that contain the 10 brightest stars in the image and correspond to the brightest stars in the catalog. We call them the initial triangles for recognition. The selection criteria of triangle similarity and the threshold for brightest stars are adjusted to find several initial triangles. It protects against cases when a bright object in the picture turns out to be an unmasked hot pixel, some noise (cloud, blinks from the Moon), or a planet.

Matching fourth star begins from the initial triangle.

During the identification triangles are created by a new star and pair of already identified stars, which are compared.

Each initial triangle leads to one or many lists of identified stars that match the position in the picture. Out of all the identified lists of stars, we choose the most numerous star list. When there are several lists that have the same number of identified stars, we select those which have the best matching between the observed and the catalog (See Figure 3). Based on a list of identified stars the coordinates of the center field of view is determined.

The stars are correctly identified even when the sky is partially cloudy or the visibility of stars is limited by bright sky background. Typically RecoStar recognize 20 to 30 stars on the image from our cameras. The whole process takes from 2 to 10 seconds on a Pentium IV 2.6GHz, depending on the number of objects detected as a star on the average image.

2.3 RecoGrid

Equatorial coordinates of identified stars are converted to a common system for multiple mean images based on the sidereal time of the meteor event. We assume that the camera was unguided and didn't change pointing direction in time.

The RecoStar does not know whether stars on a mean image was well recognized. Rejecting erroneous identification is based on the coordinates of the center. The calculated centers of view for each image are converted to a common system of coordinates. The median from all coordinates of the image centers is estimated. If the coordinates of the measured center for a given mean image deviates by more than 3 degrees from the median position we assume the image star field was poorly recognized.

To obtain more reference stars, which is needed to determine a good quality coordinate transformation for the images, we use all the stars visible in all available images with meteors through the night. Thanks to this method, several thousand reference tie-points can be utilized.

Determination of the transform from pixel coordinates on the image to equatorial coordinates is based on the Turner method (Koten, 2002). We found that the best results are obtained using a first-order function in the Turner method plus the correction function dependant on the distance from the optical center. The parameter coefficients are fit using the difference between the coordinates obtained from the image and the catalog. Applying the correction function, it is possible to obtain the accuracy of the meteor positions in equatorial coordinates of 3 arc minutes across nearly the entire image. Only on the far edges of the field of view, do we achieve less accuracy of 10 arcminutes.

2.4 RecoBase

RecoBase collects information about the time, brightness, velocity, and coordinates of the begin and end points of all the meteor events. RecoBase creates files for a DBF database. These data are used for searching and analyzing phenomena underlying activity based on single-station observations. Figure 4 shows the exemplary results obtained by Radiant (Arlt, 1992) for the largest meteor streams active during the period covered by the reduced data. For all calculations we use pixel size of 0.4 degree. A number of crossings between meteors are outlined.

3 Conclusion

The PFN shows that it is possible to build a low-cost fireball network. In 2008, the total cost for all of our hardware is estimated to about 10k Euro. The problem with low limiting magnitude for reference stars was solved by merging data from many images and events. This way we can use thousands of reference stars to achieve high quality astrometry. This task would not be possible without an automatic identifier of stars which was implemented by the PFN.

RecoStar was tested on several thousand images and recognized stars even for both partially cloudy and bright sky conditions. The method of similar triangles leads to a fast association method between measured stars and catalog stars. A single image takes from 2 to 10 seconds to analyze on a P4 2.6GHz processor. Using all the available position of stars from all images during the course of a night RecoGrid yields an astrometric accuracy in equatorical coordinates of 3 arcminutes.

Acknowledgments

We would like to thank to Siemens Building Technologies for financial support which allowed to create and run PFN.

References

Arlt R. (1992). "The software "Radiant"". *WGN Journal of the IMO*, **20:2**, 62–69.

Hoffleit D., editor (1964). *Catalogue of bright stars*. Yale University Observatory, New Haven, Conn., 3rd rev. ed. edition.

Koten P. (2002). "Software for processing of meteor video records". In Warmbein B., editor, *Asteroids, Comets, and Meteors: ACM 2002*, volume 500. pages 197–200.

Molau S. (1999). "The meteor detection software MetRec". In Baggaley W. J. and Porubcan V., editors, *Meteroids 1998*. page 131.

Spurný P., Olech A., and Kedzierski P. (2004). "Trajectory and orbit of the EN200204 Łaskarzew fireball". *WGN, Journal of the IMO*, **32:2**, 48–50.

Wiśniewski M., Olech A., Krasnowski M., Zloczewski K., Mularczyk K., Kedzierski P., and Jonderko W. (2005). "CCTV lenses for video meteor astronomy". *WGN, Journal of the IMO*, **33:1**, 23–29.

Żołądek P., Olech A., Wiśniewski M., and Kwinta M. (2007). "The PF030405a "Krzeszowice" fireball". *Earth Moon and Planets*, **100**, 215–224.

Handling Editor: Javor Kac
This paper has been typeset from a LaTeX file prepared by the authors.

About the mass and magnitude distributions of meteor showers

Janko Richter [1]

This theoretical model, inspired by thermodynamic models, describes the mass distribution of a perfect meteor shower using stochastic mathematics. In detail, it tries to explain why the observed population index is in most cases between 2 and 3 and the meteor magnitudes are distributed exponentially.

Received 2017 June 13; Revised 2017 August 14

1 Introduction

It is generally assumed that meteor magnitudes in a meteor observation have an exponential distribution (see, e.g., Rendtel and Arlt, 2017). There is a known problem with this assumption, however. Because the magnitude scale is not limited for faint meteors, the total number of meteors must be infinite (see Figure 1). Hence, there must exist at least one local magnitude maximum for all meteor magnitudes, not only for observable meteor magnitudes.

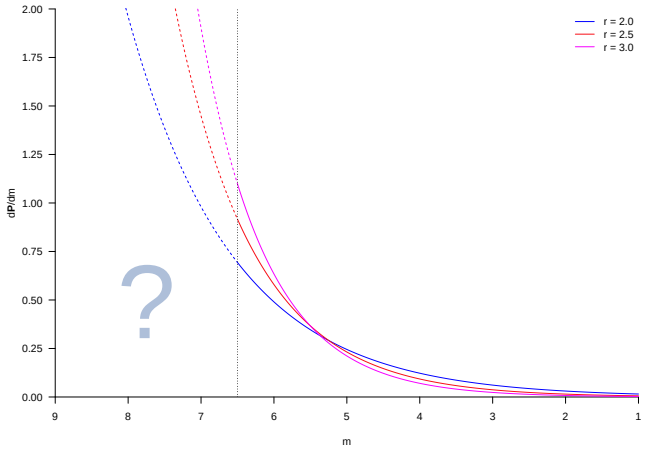

Figure 1 – Usually observed magnitude spectrum.

Another problem is why observed population indices are only between roughly 2 and 3? Why is this range apparently limited?

The answers to those problems seems to be of a stochastical nature. The theoretical model presented in this paper tries to describe how meteoroids are leaving their common orbit. For the convenience of the reader, we have added at the end of the paper a list of the symbols and abbreviations we use in the presentation of this model.

For modeling, a parent body is not required. One can assume that leaving the common orbit and leaving the parent body is the same process. It is even not required to assume that meteoroids are leaving their common orbit only near the perihelion.

2 Energy

Imagine there is a reservoir with currently not moving meteoroids in it. Then, continuously add energy to it. As a result, the meteoroids begin to leave the reservoir by chance. By the law of energy conservation, the total added energy is the same as the total kinetic energy of the ejected meteoroids combined. This is called a homogeneous Poisson point process (Stoyan, 2013). In this case, the "rate" is not the count of meteoroids per time, but the count of meteoroids per energy unit.

If nothing is known about the probability distribution of the kinetic energy of the meteoroids after leaving their common orbit and if there are no common constraints, we may assume a priori the following, by the principle of maximum entropy (Jaynes, 1957a; 1957b):

Postulate 2.1 *The kinetic energy E of a meteoroid after leaving the common orbit is exponentially distributed, i.e., the probability density function (PDF) of the random variable E equals*

$$\frac{\mathrm{d}\mathbf{P}}{\mathrm{d}E} = \lambda_E e^{-\lambda_E E}. \tag{1}$$

In Equation (1), $\lambda_E > 0$ is the only parameter of the probability density function. The expected (mean) value of the energy E is given by

$$\mathbf{E}[E] = \frac{1}{\lambda_E}. \tag{2}$$

3 Momentum

After a meteoroid has left the common orbit, it has a translation momentum $\vec{p} = M\vec{v}$, where M is the meteoroid's mass and $\vec{v}$ its velocity. We make the following simple assumptions about these momentums using the principle of maximum entropy (Jaynes, 1957a; 1957b):

Postulate 3.1 *The momentums in each of the three coordinate directions are independent.*

Postulate 3.2 *The distribution of the momentums in each of the coordinate directions does not depend on the orientation of the coordinate system.*

Hence, the distribution of the momentum is rotationally symmetrical.

With Postulates 3.1 and 3.2, it is possible to prove the following:

Proposition 3.3 *Meteoroids are leaving randomly distributed the common orbit in all directions in a three-dimensional cartesian coordinate system; in each coordinate direction, the meteoroid's momentum with which it leaves the common orbit is normally distributed with expected value 0.*

[1]Landsberger Allee 22, 10249 Berlin, Germany
Email: janko@richtej.de

IMO bibcode WGN-461-richter-mass
NASA-ADS bibcode 2018JIMO...46...34R

Proof. In probability theory, Maxwell's Theorem (see, e.g., Feller, 1966) states that if the probability distribution of a vector-valued random variable is rotationally invariant and the components are independent, then these components are all normally distributed with expected value 0 and the same variance. By Postulates 3.1 and 3.2, the preconditions of Maxwell's Theorem are satisfied, and the Proposition follows. □

Hence, the PDFs of p_x, p_y, and p_z are

$$\frac{\mathrm{d}\mathbf{P}}{\mathrm{d}p_x} = \frac{1}{\sqrt{2\pi}\sigma_p} e^{-\frac{p_x^2}{2\sigma_p^2}}; \tag{3}$$

$$\frac{\mathrm{d}\mathbf{P}}{\mathrm{d}p_y} = \frac{1}{\sqrt{2\pi}\sigma_p} e^{-\frac{p_y^2}{2\sigma_p^2}}; \tag{4}$$

$$\frac{\mathrm{d}\mathbf{P}}{\mathrm{d}p_z} = \frac{1}{\sqrt{2\pi}\sigma_p} e^{-\frac{p_z^2}{2\sigma_p^2}}, \tag{5}$$

where σ_p, the common standard deviation of p_x, p_y, and p_z, is the only parameter of these distributions.

Proposition 3.3 allows us to derive the distribution of $p^2 = p_x^2 + p_y^2 + p_z^2$. We use $q = p^2/\sigma_p^2$ to denote the normalized version of this quantity.

Proposition 3.4 *Let $p^2 = p_x^2 + p_y^2 + p_z^2$ and $q = p^2/\sigma_p^2$. The PDF of q is given by*

$$\frac{\mathrm{d}\mathbf{P}}{\mathrm{d}q} = \frac{q^{\frac{1}{2}}}{\sqrt{2\pi}} e^{-\frac{q}{2}}. \tag{6}$$

Proof. By Proposition 3.3, p_x, p_y, and p_z are three independent, normally distributed random variables with expected value 0 and the same variance. Hence, q has a χ^2-distribution with three degrees of freedom. □

From the above, the following can easily be shown for the expected (mean) value of p^2:

$$\mathbf{E}[p^2] = 3\sigma_p^2. \tag{7}$$

The last postulate in this Section describes the relation between kinetic energy E and the momentum $\vec{p}$:

Postulate 3.5 *For a meteoroid, after leaving the common orbit, the kinetic energy E and the momentum $\vec{p}$ are stochastically independent.*

Note that this does not mean that there is no causality between energy and momentum. Indeed, by classical mechanics, we have that

$$E = E(M, \vec{p}) = \frac{p^2}{2M} \tag{8}$$

for all meteoroids.

4 Mass distribution

Using postulate 3.5, we can calculate from Equation (8) the mass distribution of meteoroids. First notice that we can rewrite Equation (8) as

$$M = M(E, \vec{p}) = \frac{p^2}{2E} \tag{9}$$

Proposition 4.1 *The PDF of meteoroid mass M is given by*

$$\frac{\mathrm{d}\mathbf{P}}{\mathrm{d}M} = \frac{3}{2}\,\mu \sqrt{\frac{M}{(\mu + M)^5}}\,, \tag{10}$$

where μ, the only parameter of this distribution, is also a mass which equals

$$\mu = \lambda_E \sigma_p^2 = \frac{\mathbf{E}[p^2]}{3\mathbf{E}[E]}\,. \tag{11}$$

Proof. By Postulate 3.5, kinetic energy and squared momentum are stochastically independent, and hence also their dimensionless equivalents $\varepsilon = \lambda_E E$ and $q = p^2/\sigma_p^2$. Thus,

$$\frac{\mathrm{d}\mathbf{P}}{\mathrm{d}(\varepsilon, q)} = \frac{\mathrm{d}\mathbf{P}}{\mathrm{d}\varepsilon}\,\frac{\mathrm{d}\mathbf{P}}{\mathrm{d}q}\,. \tag{12}$$

According to Equations (1) and (6), the PDFs of ε and q are

$$\frac{\mathrm{d}\mathbf{P}}{\mathrm{d}\varepsilon} = \frac{\mathrm{d}\mathbf{P}}{\mathrm{d}E}\left|\frac{\mathrm{d}E}{\mathrm{d}\varepsilon}\right| = e^{-\varepsilon}; \tag{13}$$

$$\frac{\mathrm{d}\mathbf{P}}{\mathrm{d}q} = \frac{1}{\sqrt{2\pi}}\, q^{\frac{1}{2}} e^{-\frac{q}{2}}. \tag{14}$$

Hence,

$$\frac{\mathrm{d}\mathbf{P}}{\mathrm{d}(\varepsilon, q)} = \frac{1}{\sqrt{2\pi}}\, q^{\frac{1}{2}} e^{-\frac{q}{2}} e^{-\varepsilon}. \tag{15}$$

Using Equation (9), we can define a dimensionless mass parameter from ε and q by

$$\eta = \frac{q}{2\varepsilon} \tag{16}$$

In order to determine the PDF for the meteoroids' mass, we must do a coordinate transformation $(\varepsilon, q) \mapsto (\eta, \tau)$, with τ is any transformation coordinate orthogonal to the mass parameter η, followed by an integration:

$$\frac{\mathrm{d}\mathbf{P}}{\mathrm{d}\eta} = \int_{-\infty}^{+\infty} \frac{\mathrm{d}\mathbf{P}}{\mathrm{d}(\eta, \tau)}\,\mathrm{d}\tau \tag{17}$$

$$= \int_{-\infty}^{+\infty} \frac{\mathrm{d}\mathbf{P}}{\mathrm{d}(\varepsilon, q)} \left|\frac{\partial(\varepsilon, q)}{\partial(\eta, \tau)}\right| \mathrm{d}\tau \tag{18}$$

In order to solve the integral (18) with a Laplace transformation, the following coordinate transformation is used:

$$\eta = \frac{q}{2\varepsilon}; \tag{19}$$

$$\tau = \frac{2\varepsilon^2}{q}. \tag{20}$$

The inverse of this transformation is

$$\varepsilon = \eta\tau; \tag{21}$$

$$q = 2\eta^2\tau. \tag{22}$$

Therefore, the Jacobian determinant of this transformation is

$$\frac{\partial(\varepsilon,q)}{\partial(\eta,\tau)} = \det\begin{bmatrix}\frac{\partial\varepsilon}{\partial\eta} & \frac{\partial\varepsilon}{\partial\tau}\\ \frac{\partial q}{\partial\eta} & \frac{\partial q}{\partial\tau}\end{bmatrix} \tag{23}$$

$$= \det\begin{bmatrix}\tau & \eta\\ 4\eta\tau & 2\eta^2\end{bmatrix} \tag{24}$$

$$= 2\eta^2\tau - 4\eta^2\tau \tag{25}$$

$$= -2\eta^2\tau. \tag{26}$$

This allows for the solution of integral (18) by substituting in it Equations 15 and 26:

$$\frac{\mathrm{d}\mathbf{P}}{\mathrm{d}\eta} = \int_{-\infty}^{+\infty} \frac{\mathrm{d}\mathbf{P}}{\mathrm{d}(\varepsilon,q)} \left|\frac{\partial(\varepsilon,q)}{\partial(\eta,\tau)}\right| \mathrm{d}\tau \tag{27}$$

$$= \frac{1}{\sqrt{2\pi}} \int_0^{+\infty} (2\eta^2\tau)^{\frac{1}{2}} e^{-\eta^2\tau} e^{-\eta\tau}\, 2\eta^2\tau \,\mathrm{d}\tau \tag{28}$$

$$= \frac{2}{\sqrt{\pi}}\eta^3 \int_0^{+\infty} e^{-\eta\tau}\, \tau^{\frac{3}{2}} e^{-\eta^2\tau} \,\mathrm{d}\tau. \tag{29}$$

Now, the Laplace transform can be used, which is defined as follows:

$$\mathcal{L}\{f\}(s) = \int_0^{+\infty} e^{-st} f(t)\,\mathrm{d}t. \tag{30}$$

Hence, integral (29) can be rewritten as

$$\frac{\mathrm{d}\mathbf{P}}{\mathrm{d}\eta} = \frac{2}{\sqrt{\pi}}\eta^3 \mathcal{L}\left\{t^{\frac{3}{2}} e^{-\eta^2\tau}\right\}(\eta). \tag{31}$$

Application of the Laplace transformation yields

$$\frac{\mathrm{d}\mathbf{P}}{\mathrm{d}\eta} = \frac{2}{\sqrt{\pi}}\,\eta^3 \frac{3\sqrt{\pi}}{4\,(\eta+\eta^2)^{\frac{5}{2}}} \tag{32}$$

$$= \frac{3}{2}\sqrt{\frac{\eta}{(1+\eta)^5}}\,. \tag{33}$$

Using Equation (9), $\varepsilon = \lambda_E E$, and $q = p^2/\sigma_p^2$, we get

$$M = \frac{p^2}{2E} \tag{34}$$

$$= \frac{\lambda_E \sigma_p^2 q}{2\varepsilon} \tag{35}$$

$$= \lambda_E \sigma_p^2 \eta \tag{36}$$

$$= \mu\eta, \tag{37}$$

with $\mu = \lambda_E\sigma_p^2$. Finally, Equations (33) and (37) yield

$$\frac{\mathrm{d}\mathbf{P}}{\mathrm{d}M} = \frac{\mathrm{d}\mathbf{P}}{\mathrm{d}\eta}\left|\frac{\mathrm{d}\eta}{\mathrm{d}M}\right| \tag{38}$$

$$= \frac{3}{2}\,\mu\sqrt{\frac{M}{(\mu+M)^5}}\,, \tag{39}$$

the desired result. □

Integration of Equation (10) yields the cumulative distribution function (CDF) $\mathbf{P}[M \le M_0]$, the probability that the meteoroid's mass is at most M_0:

Proposition 4.2 *The CDF of meteoroid mass equals*

$$\mathbf{P}[M \le M_0] = \left(\frac{M_0}{\mu + M_0}\right)^{\frac{3}{2}}. \tag{40}$$

Proof. By integration, we find that

$$\mathbf{P}[M \le M_0] = \int_0^{M_0} \frac{\mathrm{d}\mathbf{P}}{\mathrm{d}M}\,\mathrm{d}M \tag{41}$$

$$= \left(\frac{M_0}{\mu + M_0}\right)^{\frac{3}{2}}, \tag{42}$$

the desired result. □

5 Logarithmic mass distribution

We consider the logarithmic meteoroid mass defined by

$$m := \frac{1}{a}\ln(bM), \tag{43}$$

with a and b constants. The CDF of logarithmic meteoroids mass follows immediately from Equation (40) in Proposition 4.2:

Proposition 5.1 *The CDF of logarithmic meteoroid mass m as defined in Equation* (43) *is given by*

$$F(m) = \left(\frac{e^{am}}{e^{a\psi} + e^{am}}\right)^{\frac{3}{2}}, \tag{44}$$

with

$$\psi = \frac{1}{a}\ln(b\mu) \tag{45}$$

the only parameter of this function. We have that

$$\begin{cases}\mathbf{P}[m \le m_0] = F(m_0) & \text{if } a > 0\,;\\ \mathbf{P}[m \ge m_0] = F(m_0) & \text{if } a < 0\,.\end{cases} \tag{46}$$

The PDF of logarithmic meteoroid mass now follows straightforwardly from Proposition 5.1 by differentiation of Equation (44), or, alternatively, from

$$\frac{\mathrm{d}\mathbf{P}}{\mathrm{d}m} = \frac{\mathrm{d}\mathbf{P}}{\mathrm{d}M}\left|\frac{\mathrm{d}M}{\mathrm{d}m}\right|, \tag{47}$$

using $M = e^{am}/b$ and $\mu = e^{a\psi}/b$ (cf. Equations (43) and (45) and Equation (10) from Proposition 4.1):

Proposition 5.2 *The PDF of logarithmic meteoroid mass m as defined in Equation* (43) *is*

$$\frac{\mathrm{d}\mathbf{P}}{\mathrm{d}m} = \frac{3}{2}\,|a|\sqrt{\frac{e^{2a\psi+3am}}{\left(e^{a\psi}+e^{am}\right)^5}}\,. \tag{48}$$

This PDF has very interesting properties when $m \to -\infty$ or $m \to \infty$. In both cases, it approximates an exponential distribution:

$$\frac{\mathrm{d}\mathbf{P}}{\mathrm{d}m} \approx \begin{cases}\frac{3}{2}|a|e^{a\psi}\,e^{-am} & \text{if } am \gg a\psi\,;\\ \frac{3}{2}|a|e^{-\frac{3}{2}a\psi}\,e^{\frac{3}{2}am} & \text{if } am \ll a\psi\,.\end{cases} \tag{49}$$

6 Magnitude distribution

An example of a logarithmic mass distribution is the magnitude distribution of meteor brightness:

$$m(I) = -2.5 \log\left(\frac{I}{I_0}\right). \tag{50}$$

Assuming a linear relationship between a meteor's luminance and the mass of the corresponding meteoroid, i.e., $I(M) \propto M$, or

$$I(M) = CM, \tag{51}$$

for some constant C, then the parameters a and b are

$$\begin{cases} a &= -\ln(10)/2.5 \approx -0.921034\ldots; \\ b &= C/I_0. \end{cases} \tag{52}$$

With Equation (48) and

$$r = e^{-a} = 10^{0.4} \approx 2.51189\ldots \tag{53}$$

we obtain the following:

Proposition 6.1 *The PDF of meteor magnitudes is given by*

$$\frac{\mathrm{d}\mathbf{P}}{\mathrm{d}m} = \frac{3}{2}\ln(r)\sqrt{\frac{r^{-2\psi-3m}}{(r^{-\psi}+r^{-m})^5}}. \tag{54}$$

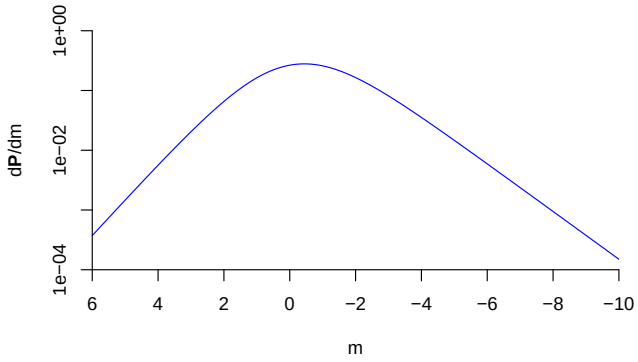

Figure 2 – Example of a probability density function of meteor magnitude for parameter $\psi = 0$.

From Equation (49), we now derive the following:

Proposition 6.2 *The magnitude of brighter meteors is approximately exponentially distributed with*

$$\frac{\mathrm{d}\mathbf{P}}{\mathrm{d}m} \approx \frac{3}{2}\ln(r)\, r^{-\psi}\, r^{m}. \tag{55}$$

This is a quite good match with meteor observations. The meteor magnitudes in the observable magnitude range are indeed exponentially distributed and the measured population index r is usually between 2 and 3.

For *all* meteor magnitudes, the distribution according to Equation (54) reaches a maximum, as argued in the Introduction. As an example, Figure 2 shows the probability density function of meteor magnitude in the case that $\psi = 0$.

7 Conclusions

In order to validate or refute this model, observations of faint meteors are required.

Please note that this model does not consider further effects on the meteoroid's mass such as, for example, the Poynting-Robertson effect (see, e.g., Jenniskens, 2006, p. 536 a.f.). The assumptions we made are quite simple, but already result in a good match for observations of brighter meteors.

Because the population index r is nearly constant, i.e., showing little variation between different meteor showers, it is not such an interesting parameter to measure. The only interesting parameter is ψ, because it describes the entire mass distribution of a meteor shower.

Furthermore, analysts of meteor observations are invited to perform stochastical tests to validate the exponential distribution of meteor magnitudes. If the tests fail, this means that the common method to compute ZHRs (see, e.g., Rendtel and Arlt, 2017) should not be used. Analysts are also encouraged not to assume exponential distributions when considering the full range of meteor brightnesses.

For calculations of flux densities, good estimates of the parameter ψ or, even better, the parameter μ are required. This work suggests that knowledge of one of these parameters that is essential to determine a flux density.

List of symbols and abbreviations

a, b	Constants used in the logarithmic meteoroid mass.
CDF	Cumulative distribution function.
$\frac{\mathrm{d}\mathbf{P}}{\mathrm{d}X}$	Probability density function of a variable X.
$\frac{\mathrm{d}\mathbf{P}}{\mathrm{d}(X_1,X_2)}$	Joint probability density function of variables X_1 and X_2.
$\frac{\partial(f_1,f_2)}{\partial(x_1,x_2)}$	Jacobian matrix of the function $f : \mathbf{R}^2 \to \mathbf{R}^2 : (x_1, x_2) \mapsto (f_1(x_1, x_2), f_2(x_1, x_2))$.
$\mathbf{E}$	Expected value (mean).
E	Kinetic energy of a meteoroid after leaving the common orbit.
ε	Dimensionless version of the kinetic energy of a meteoroid E, i.e., $\varepsilon = \lambda_E E$.
η	Dimensionless version of meteoroid mass M, i.e., $\eta = q/(2\varepsilon) = M\mu$.
I	Luminance of a meteor.
I_0	Reference value for the luminance of a meteor.
ln	Natural logarithm, i.e., with basis the number $e = 2.71828\ldots$.
log	Common or Briggsian logarithm, i.e., with basis 10.

λ_E	Only parameter of the exponential distribution of a meteoroids' kinetic energy E after leaving the common orbit.
M	Meteoroid mass.
M_0	Value for the mass of a meteoroid.
m	Logarithmic meteoroid mass. In particular, meteor magnitude.
μ	Only parameter of the mass probability distribution of meteoroids. It is itself a mass.
PDF	Probability density function.
P	Probability.
$\vec{p}$	Translational momentum of a meteoroid leaving the common orbit.
p_x, p_y, p_z	Cartesian coordinates of the translational momentum vector $\vec{p}$.
p^2	Squared length of the translational momentum vector $\vec{p}$.
ψ	The only parameter of the logarithmic mass probability distribution, and, in particular, the meteor magnitude probability distribution. In this case, ψ itself is a meteor magnitude.
q	Normalized version of p^2, i.e., $q = p^2/\sigma_p^2$.
r	Population index of the magnitude distribution of a meteor shower.
σ_p	Standard deviation and only parameter of the zero-mean normal distribution of the components p_x, p_y, and p_z of the translational momentum $\vec{p}$.
τ	Transformation coordinate orthogonal to the mass parameter η.
$\vec{v}$	Velocity of a meteoroid after leaving the common orbit.
ZHR	Zenithal Hourly Rate of a meteor shower.

Acknowledgement

The author would like to thank the Handling Editor for his helpful advice, reviews, and comments, as well as for editing this article.

In addition, the Handling Editor wishes to thank Dr. Karel Proesmans of Hasselt University for his assistance in reviewing an earlier version of this paper.

References

Feller W. (1996). *An Introduction to Probability Theory and its Applications. II.* John Wiley & Sons Inc.

Jaynes E. T. (1957a). "Information theory and statistical mechanics". *Physical Review*, **106**, 620–630.

Jaynes E. T. (1957b). "Information theory and statistical mechanics ii". *Physical Review*, **108**, 171–190.

Jenniskens P. (2006). *Meteor Showers and their Parent Comets.* Cambridge University Press.

Rendtel J. and Arlt A., editors (2017). *Handbook for Meteor Observers.* IMO.

Stoyan D. (2013). *Stochastic geometry and its applications.* John Wiley & Sons Inc.

Handling Editor: Marc Gyssens
This paper has been typeset from a LaTeX file prepared by the author.

Radio meteors

Visualizing meteor streams by radio forward scattering on the basis of meteor head echoes

Wolfgang Kaufmann[1]

The outcome of radio meteor observation of a basic monitoring system based on forward scattering can be enhanced by additionally analysing meteor head echoes. Meteoroids of common origin produce in a circumscribed area of reflection a bunch of head echoes with equally Doppler shifted frequency gradients. These can be made visible in a kernel density map. Measurements are performed to verify this idea and to outline the possibilities and constraints. The described method proves to provide a spatially differentiated depiction of the monitored meteoric activity.

Received 2018 January 15

1 Introduction

The observation of radio meteors via forward scattering can be performed 24h a day regardless of clouds and the position of the sun and the moon. As long as only the presence of a meteor will be detected this will not provide any positional information about it. This is a severe shortcoming of forward scattering. To overcome this at least an interferometric system must be built up (Rendtel & Arlt, 2015). In this paper a new way for a basic radio monitoring station is described to identify different origins of meteors. It requires a radio meteor receiving and detecting system that is able to pick up meteor head echoes and their frequency change with a sufficient time and frequency resolution.

Meteor head echoes are radio waves scattered from the small intense plasma region surrounding the meteoroid during its atmospheric passage. On its flight a meteoroid shows a permanent changing radial velocity with respect to the observer (Kero et al., 2008). Also it undergoes a deceleration dependent on its physical characteristics and entry velocity (Kikwaya et al., 2009). So Doppler shift of the reflected radio frequency is not constant but reveals a specific slope. Meteoroids of a shower move on almost parallel trajectories and their head echoes should produce a consistent group of frequency slopes in a circumscribed region of reflection. These groups can be made visible in a kernel density plot. So, different sources of meteoric activity in the sky can be detected. Yet a localisation of the radiant cannot be achieved by this procedure. This is out of the reach of a single basic forward scattering system.

The practical procedure and the results of four observation sessions are described and shall demonstrate the possibilities of forward scattering taking in account head echoes.

2 Material and Methods

The French radar-transmitter GRAVES was employed for forward scattering. It transmits a continuous rf-signal at a frequency of 143.050 MHz and illuminates a well defined region of the sky in 100 km height, see Figure 1. Receiving location was Algermissen, Northern Germany (N 52°15′16, E 009°58′71). A HB9CV-antenna was directed to the transmitter location and fed to a FUNcube Dongle Pro+ (FCDP). The FCDP is a software defined receiver.[a] This means all filtering and demodulation is done by software. SDR# was used as receiving software.[b] It was set to USB, 143.049 MHz receiving frequency, 48 kHz audio output, audio filtering and AGC switched off. The audio output was fed to the software Meteor Logger[c], which detects and logs meteor signals within an audio stream (Kaufmann, 2017). It reveals a continuous output i.a. of the frequency of the detected signal in 10.7 ms steps. Both programs ran on the same computer (Intel i5, clock speed 2.3 GHz) with Windows 7.

For post processing of the gathered data, the software Process Data[c] was used to reduce interference and extract the frequency slopes of the received head echoes. First the software calculates the median of all recorded frequencies, $f(\text{median})$, gradually to take account of a possible receiver drift. Hereby $f(\text{median})$ represents the frequency of the meteor trails because these are much more numerous than head echoes. Then the software reduces interference by eliminating any signal that do not contain at least one frequency in the range of $f(\text{median}) \pm 2df$, where df is the frequency resolution of the measurement (it is predefined by Meteor Logger to 23.4 Hz). At least the software runs through the frequencies, $f(i)$, of each signal and checks for the following three conditions that must be fulfilled cumulative to identify an analysable head echo, see Figure 2, upper graph:

1. start frequency $f(i = 1)$ must be $\geq 5df + f(\text{median})$,
2. each subsequent frequency, $f(i + 1)$, must be $\leq$ its precedent frequency, $f(i)$ until $f(i) < 2df + f(\text{median})$,
3. number of frequencies, fulfilling (1) and (2), must be ≥ 3.

[1]Lindenweg 1e, 31191 Algermissen, Germany.
Email: contact@ars-electromagnetica.de

IMO bibcode WGN-461-kaufmann-radio
NASA-ADS bibcode 2018JIMO...46...39K

[a]http://www.funcubedongle.com/
[b]https://airspy.com/download/
[c]http://www.ars-electromagnetica.de/robs/download.html

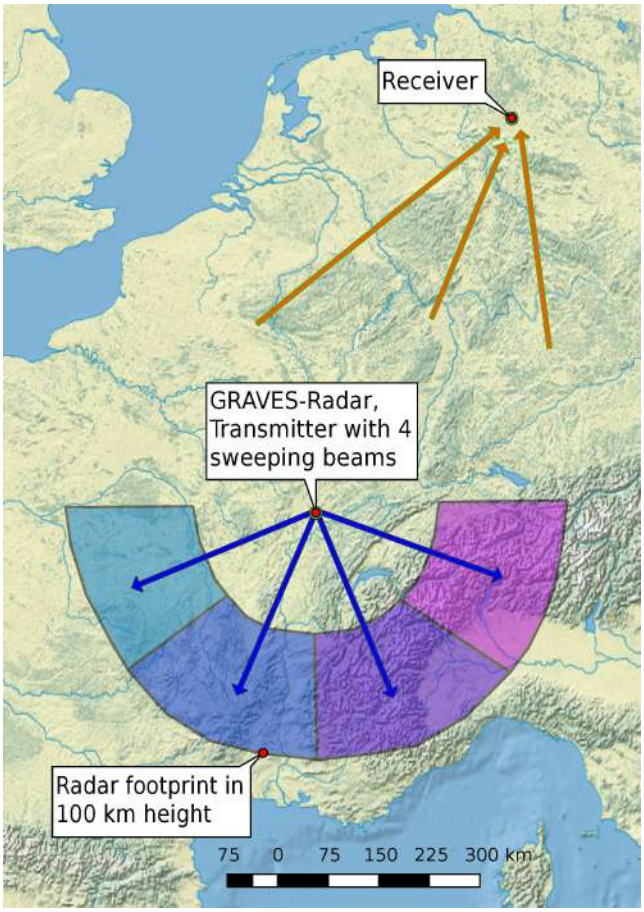

Figure 1 – Footprint of the French GRAVES radar and location of the receiver at Northern Germany. Four radar beams continuously sweep in steps of 7.5° each 0.8 s in azimuthal sectors of 45°.[d] Please note the quoted paper still states steps of 3.2 s duration, this has been changed a few years ago to 0.8 s. Map made with Natural Earth.

From the resulting time series of frequencies of a head echo signal the slope was calculated by the software by means of a linear regression analysis.

The extracted frequency slopes with associated date-time stamps were transformed to obtain the same scale. The date-time stamp was converted to a decimal number, starting from the first day of detection at 00^h UTC with 0.0. To the absolute value of the frequency slope a decadic logarithm was applied to reduce the skewness of the distribution. Finally by means of the statistic software PAST (Hammer et al., 2001)[e], a kernel density map was produced with these pairs of data. Thereby a triangular kernel function was selected. This function was found to produce the most structured display. For a better readability the decimal day indication was replaced by date-time markers in the finished plot.

For comparative purposes also the hourly count rates (HCR) of all registered meteor-signals are determined. This again was obtained with the software Process Data. After reduction of interference the remaining signals were conflated if the time span between two signals was less than 0.525 s. If the precedent signal showed a logarithmic decline or the subsequent signal started with a head echo no conflation was performed. Then the number of signals per hour were ascertained and smoothed by a moving average. The resulting bar chart was superimposed on the kernel density map. The hypothetical hourly count rate of sporadic meteors was calculated from a fitted sine function (Powell, 2017) and is also indicated in the bar chart.

[d] http://www.itr-datanet.com/~pe1itr/pdf/The%20143.050MHz%20Graves%20Radar%20a%20VHF%20Beacon.pdf

[e] http://folk.uio.no/ohammer/past/

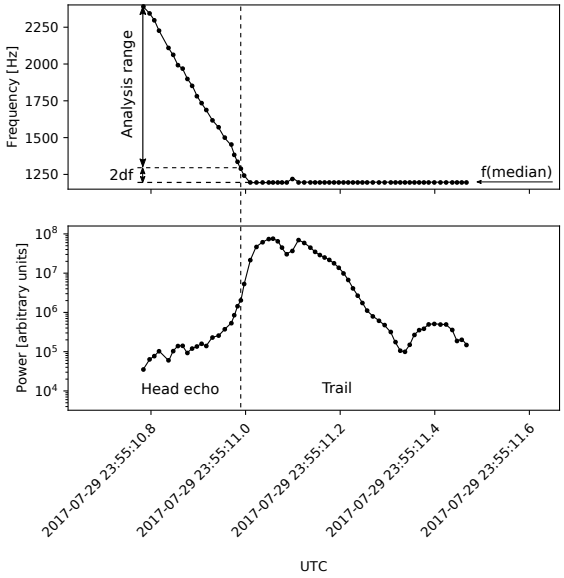

Figure 2 – An example of a meteor signal consisting of head echo and trail. The upper graph shows the progress of the reflected peak frequency. Head echoes are analysed only within the indicated range, for details see text. The lower graph exhibits the corresponding received power.

The calculation of the altitude of an assumed radiant for each date-time stamp of a received meteor signal was also carried out by Process Data. Right ascension and declination of each radiant was taken from Rendtel (2016). After unity-based normalisation the graph of the altitude was also superimposed on the kernel density map.

3 Results

Four radio meteor logging sessions were performed, see Table 1. From all detected meteor signals only about 12% show a head echo. According to Close et al. (2002) the plasma sheet around the meteoroid itself can be assumed to be spherical. Therefore a reflection of a small portion of the incident rf-power in direction of the receiver location should be possible independent of the angle of irradiance. Yet the benefit of the resulting general visibility is counteracted by the low radar cross section (RCS) of small meteoroids. E.g. Close et al. (2002) found a maximum RCS of 0.14 m^2 at 160 MHz for the Leonids. The reflected power at meteor trails is by orders of magnitude higher, see e.g. Figure 2. So smaller or very slow meteoroids can be detected only via their trail whereas their head echoes are too weak to be registered.

Hence the number of observed head echoes mainly depend on the overall sensitivity of the receiving system, the flux density and mass distribution of the me-

Table 1 – Brief overview of the radio meteor logging sessions.

Main Meteor Shower	Date and Time [UTC] of Observation 2017	Number of Detected Meteors	Number of Detected Head Echoes	Percentage of Head Echoes
SDA	Jul 27 03^h00^m – Jul 31 19^h59^m	8267	990	12.0%
PER	Aug 09 20^h00^m – Aug 14 17^h59^m	11663	1226	10.5%
DSX	Sep 25 03^h00^m – Sep 29 16^h59^m	6251	804	12.9%
ORI	Oct 18 20^h00^m – Oct 23 17^h59^m	8015	1090	13.6%

teor stream (Belkovich et al., 2005) and analogously to Lambert's cosine law to the angle of incidence. However the frequency slope of a head echo depends on the velocity and trajectory of its decelerating meteoroid in relation to both the transmitter position as well as the receiver position. In a kernel density map both the number and the frequency slopes of all observed head echoes can be combined: numerous head echoes with similar frequency slopes will be apparent as hot spots.

In the following the specific logging sessions will be addressed by their present main meteor shower according to Table 1. To interpret the findings in the kernel density maps the progress of the Zenithal Hourly Rate (ZHR) of a meteor stream was taken from Rendtel (2014). The active showers at a given time span were extracted from Rendtel (2016).

3.1 The Perseids (PER) observation

The PER are known to show high ZHR during their broad maximum. This minimizes the influence of all other sources of meteors. The radiant of PER circled well above the horizon in the northern sky which was basically true for the complete time span of the observations, see Figure 3, top. As can be seen in Figure 4 from about August 12 03^h to August 14 10^h UTC there was a strong presence of head echoes with common frequency slopes. With the diurnal movement of the radiant in terms of altitude and azimuth also the trajectories of the meteoroids changed relative to transmitter and receiver. This led to an altered progress of the radial velocities resulting in a serrated sequence of diurnal changing values of the frequency slopes as indicated in Figure 4. This pattern recurs in the azimuthal course of the radiant with daytime, see Figure 3, bottom. Between 02^h and 09^h UTC there was a fast change from East to West whereas the return to East was much slower.

The density of the slopes of the head echoes along the track of PER showed to be variable. In principle it followed the overall meteor shower activity as can be derived from the difference between observed HCR and the assumed amount of the sporadic meteors. In detail there were some deviations. E.g. the maximum of HCR on August 13 05^h UTC did not produce the highest density in the plot. Also the steep rise of the track on August 12 from about $04^h - 08^h$ UTC did not recur such pronounced on August 13 and 14 despite similar or higher HCR. So variations in the mass distribution also may contribute.

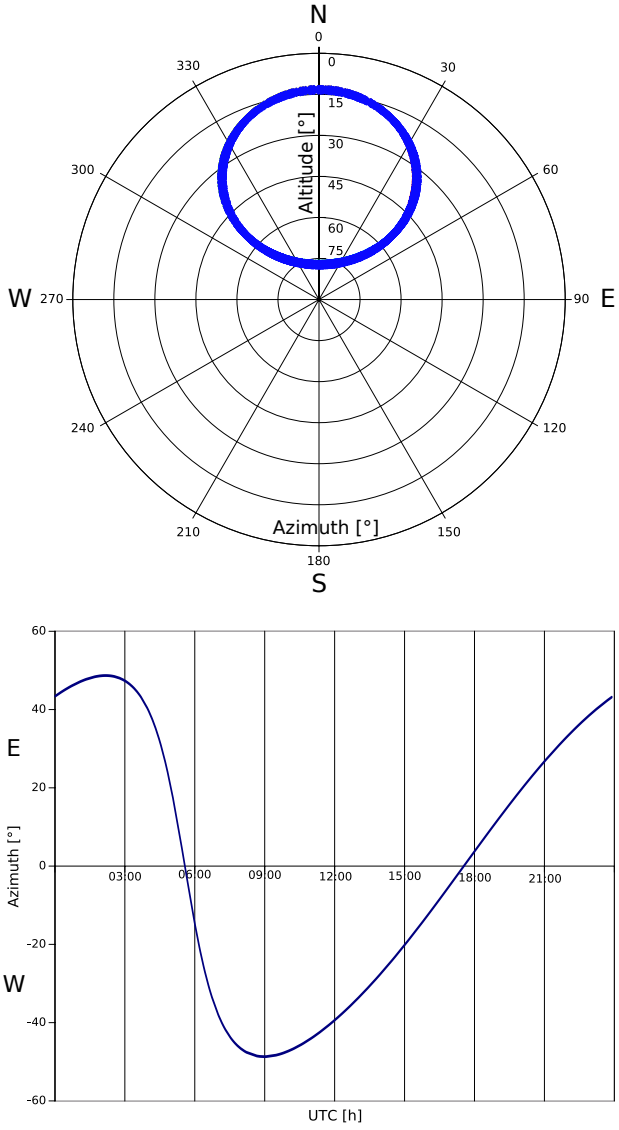

Figure 3 – Top: Polar plot of altitude and azimuth of the radiant of PER at the location of the footprint of GRAVES on August 12. Bottom: Plot of the azimuth of the radiant of PER against daytime at the location of the footprint of GRAVES on August 12.

3.2 The Southern δ-Aquariids (SDA) observation

Unfortunately there was a high level of noise present from July 28, 22^h UTC to 29, 12^h UTC and again from July 29, 22^h UTC to 30, 17^h UTC. As a consequence the weaker signals were buried resulting in a drastically declined number of observed meteors. So observations

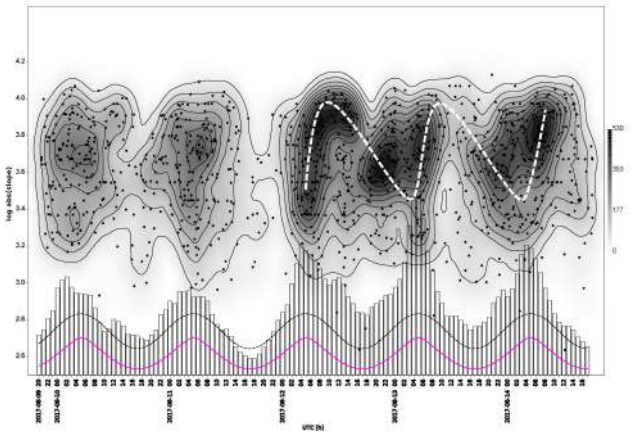

Figure 4 – The PER kernel density map. Each dot represents the frequency slope of a head echo. The dashed line track the PER. Superimposed are the hourly count rates of all observed meteors (min = 23, max = 251 counts/h). Herein the hypothetical amount of sporadic meteors is denoted. Also the normalised altitude of the radiant of the PER is indicated (magenta line) at the location of the footprint of GRAVES radar.

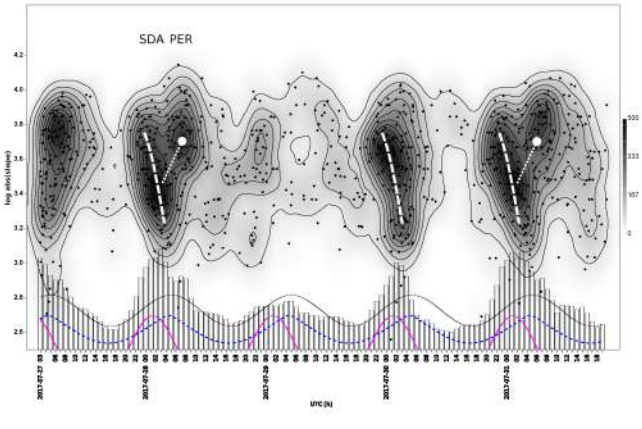

Figure 5 – The SDA kernel density map. Each dot represents the frequency slope of a head echo. Dashed lines track the SDA. Dotted lines simply indicate relations. Superimposed are the hourly count rates of all observed meteors (min = 27, max = 155 counts/h). Herein the hypothetical amount of sporadic meteors is denoted. Also the normalised altitude of the radiants of the SDA (magenta) and PER (blue) are indicated at the location of the footprint of GRAVES radar.

on July 29 turn out to be a complete failure and were strongly biased on July 30.

Together with the predominant SDA at least PAU, CAP and PER should be present during the observation. The diurnal changing values of the frequency slopes of the SDA can be tracked in the kernel density map at least on July 28 and 31, see Figure 5. PAU and CAP cannot be identified individually because of their low flux densities in combination with their high proximity to the radiant of SDA. All three radiants only temporarily moved above the horizon for a restricted range of azimuth. This depicts as a short track of changing values of the frequency slopes of the common head echoes. However the PER are well distinguishable. Their frequency slopes form a single hot spot when their radiant was near its maximum altitude. Outside the maximum altitude the number of observed head echoes was too low to be mapped. The curve of HCR shows the SDA as high peak and the PER as tiny subsidiary summit.

3.3 The Orionids (ORI) observation

During this observation besides the predominant ORI also the EGE and LMI were active. The ORI produced much smaller HCR than the SDA so the sporadic meteor background cannot be neglected anymore. At least the antihelion source with mainly the STA/NTA and the helion source should be considered. The radiants of all above-mentioned sources only temporarily rose above the horizon. The ORI exhibit diurnal changing values of the frequency slopes in form of short tracks in the kernel density map, see Figure 6. ORI and EGE cannot be identified individually because of the low activity of EGE in combination with the fairly adjacent radiants of the two streams. The STA/NTA and LMI/helion source can be recognised as ellipsoids very clearly on October 20 but can be found also during the other days of the observation. STA/NTA, ORI and

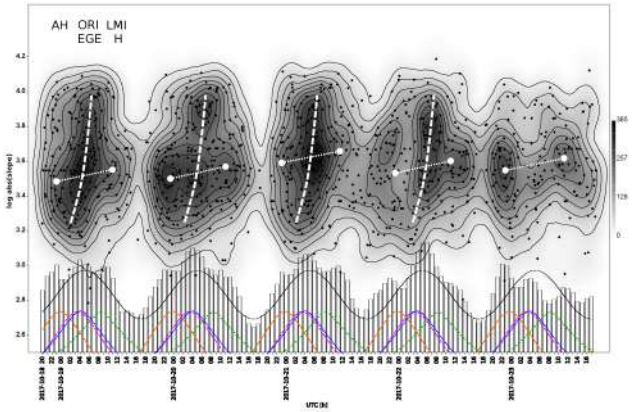

Figure 6 – The ORI kernel density map. Each dot represents the frequency slope of a head echo. Dashed lines track the ORI. Dotted lines simply indicate relations. Superimposed are the hourly count rates of all observed meteors (min = 25, max = 108 counts/h). Herein the hypothetical amount of sporadic meteors is denoted. Also the normalised altitude of the radiants of the antihelion source AH (on base of the radiants of the NTA/STA, orange), the ORI (magenta), EGE (blue) and LMI (green) are indicated at the location of the footprint of GRAVES radar (from left to right). H = helion source.

LMI/helion source also are visible in the curve of the HCR as separate peaks or shoulders.

The density distribution of the frequency slopes of the head echoes along the diurnal tracks of the ORI noticeably differed from one day to the next. Especially on October 20 and 22 the overall density was low despite a high value of HCR. A noticeable change in the mass distribution towards lower number of meteoroids with higher masses may be assumed.

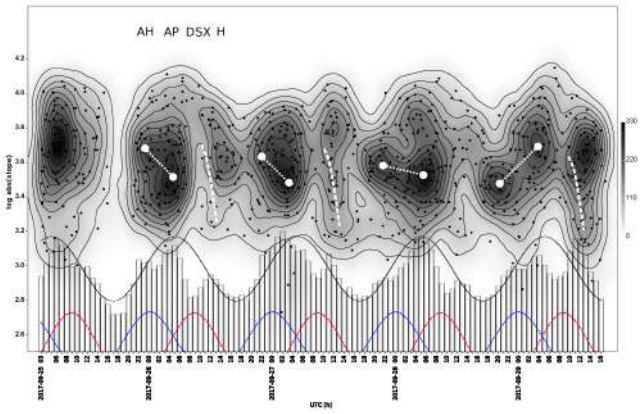

Figure 7 – The DSX kernel density map. Each dot represents the frequency slope of a head echo. Dashed lines track the DSX. Dotted lines simply indicate relations. Superimposed are the hourly count rates of all observed meteors (min = 27, max = 86 counts/h). Herein the hypothetical amount of sporadic meteors is denoted. Also the normalised altitude of the radiants of the antihelion source AH (on base of the radiants of the STA, blue) and the DSX (red) are indicated at the location of the footprint of GRAVES radar (from left to right). AP = apex source, H = helion source.

3.4 The Daytime Sextantids (DSX) observation

Within the observation period, the minor active DSX and from the sporadic meteor background the helion source, the apex source and the antihelion source with mainly the STA were present. Their radiants rose only temporarily above the horizon. Sporadic meteors dominated the hourly count rates, see Figure 7. The prominent diurnal hot spots at 05^{h} UTC (= 06^{h} local time) in the kernel density map coincided with the maximum activity of the apex source (Rendtel, 2006). The diurnal short tracks of changing values of the frequency slopes of the DSX onto the background of the helion source can be assumed on September 26, 27 and 29. On September 28 only the HCR show a small peak at 12^{h} UTC, a clear representation in the kernel density map cannot be found. The antihelion source can be well distinguished from the apex source both being depicted as ellipsoids. Yet the density centres of both change their positions relative to each other to a great degree. Both sources cannot be distinguished reliably in the curve of HCR.

4 Discussion

The footprint of GRAVES radar in 100 km height consists of four different fields, see Figure 1. So four different geometrical conditions of reflections exist simultaneously. Hence a meteor stream must be expected to produce four contiguous groups of head echo frequency slopes at the receiver site. This may explain the broadened tracks of the meteor streams as shown in Figures 4–7. This effect reduces the directional sensitivity of the receiving system.

The PER observation validates the theoretical considerations by demonstrating the grouping of head echoes with common frequency slopes originating from a common source. Also a first impression of the variance of the frequency slopes is achieved resulting from different radiant positions. Thereby the azimuth of the radiant has a much greater influence on the resulting radial velocities than the altitude in this observation. This analysis shows that indeed different radiant-positions can be identified via the frequency slopes of head echoes.

The SDA, ORI and DSX observations follow a descending order of radio activity level as described in Ogawa & Steyaert (2017). So, the interaction of meteor shower and sporadic meteors can be gradually studied. The SDA show HCR being well above the sporadic meteor background. Hence only the SDA and the PER appear in the kernel density map. The HCR of ORI exceed the assumed amount of the sporadic meteors only by a small quantity. The antihelion source now becomes apparent in the kernel density map whereas the apex source is widely masked by the ORI. The DSX are almost embedded in the sporadic meteor background. The antihelion and apex source now are visible together with the DSX. Thereby the apex source shows to have higher HCR and higher densities in the kernel density map than the antihelion source. This is in accordance with Jakšová et al. (2015). This analysis shows that the detectability of meteor sources by means of a kernel density map is determined by the activity of the single present streams.

The density within a kernel density map depends on the number of head echoes with similar frequency slopes. This number is a result of mainly (1) the activity of the meteor stream, (2) the altitude of its radiant and (3) its mass distribution. In general the calculated densities are found to follow the difference between observed HCR and the assumed amount of the sporadic meteors, i.e. are primarily characterised by (1) and (2). For the most part the influence of (3) cannot be directly observed. The described inconsistencies between density and HCR being apparent in the kernel density maps of PER and ORI could indicate the impact of (3).

The DSX observation shows an interesting dynamics of the antihelion and apex source of sporadic meteors. Shape and position of highest density vary strongly from day to day in the kernel density map. It can be assumed that this is an expression of the high inhomogeneity of these sources.

5 Conclusion

The density mapping of frequency slopes of head echoes allow a new and more detailed insight in the occurrence of radio meteors received by a basic radio monitoring station. It can help to understand and interpret the course of the observed HCR: individual HCR-segments can be assigned to meteor streams or delimited from various sources of sporadic meteor background and possibly also from interference. Meteor streams with low activity being numerically embedded in the sporadic meteor background can be made visible. The dynamics of various sources of meteors become apparent. So far the presented results are analysed under a qualitative aspect. Further research may show whether quantitative results can also be compiled.

References

Belkovich O. I., Nedeljković S., and Verbeeck C. (2005). "Forward scatter meteor observations". In Verbeeck C. and Wislez J.-M., editors, *Proceedings of the Radio Meteor School, Oostmalle, Belgium, September 10-14, 2005*. International Meteor Organization, pages 55–66.

Close S., Oppenheim M., Hunt S., and Dryud L. (2002). "Scattering characteristics of high-resolution meteor head echoes detected at multiple frequencies". *J. Geophs. Res.*, **107:A10**. SIA 9 (1-12).

Hammer Ø., Harper D. A. T., and Ryan P. D. (2001). "PAST: Paleontological statistics software package for education and data analysis". *Palaeontologia Electronica*, **4:1**, 9pp.

Jakšová I., Porubčan V., and Klačka J. (2015). "Structure and sources of the sporadic meteor background from video observations". *Publ. Astron. Soc. Japan*, **67:5**. (1-7).

Kaufmann W. (2017). "New radio meteor detecting and logging software". *WGN, Journal of the IMO*, **45:4**, 67–72.

Kero J., Szasz C., Pellinen-Wannberg A., Wannberg G., Westman A., and Meisel D. D. (2008). "Determination of meteoroid physical properties from tristatic radar observations". *Ann. Geophys.*, pages 2217–2228.

Kikwaya J.-B., Campbell-Brown M., G. B. P., Hawkes R. L., and Weryk R. J. (2009). "Physical characteristics of very small meteoroids". *A&A*, **497**, 851–867.

Ogawa H. and Steyaert C. (2017). "Major and daytime meteor showers using global radio meteor observations covering the period 2001-2016". *WGN, Journal of the IMO*, **45:5**, 98–106.

Powell C. (2017). "Modelling & analysis of diurnal variation in meteor flux". *WGN, Journal of the IMO*, **45:2**, 32–37.

Rendtel J. (2006). "Sporadic meteors". In Kac J. and Bettonvil F., editors, *Proceedings of the International Meteor Conference, Roden, The Netherlands, September 14-17, 2006*. International Meteor Organization.

Rendtel J., editor (2014). *Meteor Shower Workbook 2014*. International Meteor Organization, Potsdam.

Rendtel J. (2016). "2017 Meteor Shower Calendar". IMO_INFO (2-16).

Rendtel J. and Arlt R. (2015). *Handbook for Meteor Observers*. International Meteor Organization, Potsdam.

Handling Editor: Jean-Louis Rault

Preliminary results

Results of the IMO Video Meteor Network — July 2017, and effective collection area continued

Sirko Molau[1], *Stefano Crivello*[2], *Rui Goncalves*[3], *Carlos Saraiva*[4], *Enrico Stomeo*[5], *and Javor Kac*[6]

The IMO Video Meteor Network cameras recorded over 35 000 meteors in more than 8 300 hours of observing time during 2017 July. The flux density profile of the 2017 July γ-Draconids is presented and is found to be lower than the average of 2011–2015. Discussion of the effective collection area of video cameras is continued and findings applied to the July γ-Draconids.

Received 2018 February 22

1 Introduction

During July, 37 observers of the IMO Network, with their 73 active video cameras, enjoyed perfect observing conditions. On two nights, 70 of these cameras were active. 66 of the cameras collected data on twenty and more observing nights, and seven of these observed without a break at all. This time, it was the German observers who were below the average with "only" little more than twenty observing nights. In total we recorded over 35 000 meteors in 8 300 hours of effective observing time (Table 1 and Figure 1). The output is lower than in earlier years because there were fewer active cameras.

2 July meteor showers

The two most important showers of July – the Southern δ-Aquariids and α-Capricornids – reach their peak just before the end of the month. Their descending activity branch extends well into August, which is why we will discuss their flux density profiles in the next monthly report.

2.1 July γ-Draconids

The July γ-Draconids produced a remarkable outburst last year with a short peak of up to 20 meteoroids per 1 000 km^2 per hour at 125.°132 solar longitude (Molau et al., 2016). This solar longitude interval was outside the European observing window in 2017, but during the nights before and after we recorded lower activity than the average for 2011 to 2015 (Figure 2).

3 Effective collection area continued

Since there is no other relevant meteor shower in July, we now want to continue and conclude our analysis of the effective collection area of video cameras and the best observing direction. In Molau et al. (2017) we demonstrated the impact of boundary conditions like the meteor shower velocity, population index and atmospheric extinction. Depending on these parameters, the detection probability may vary significantly,

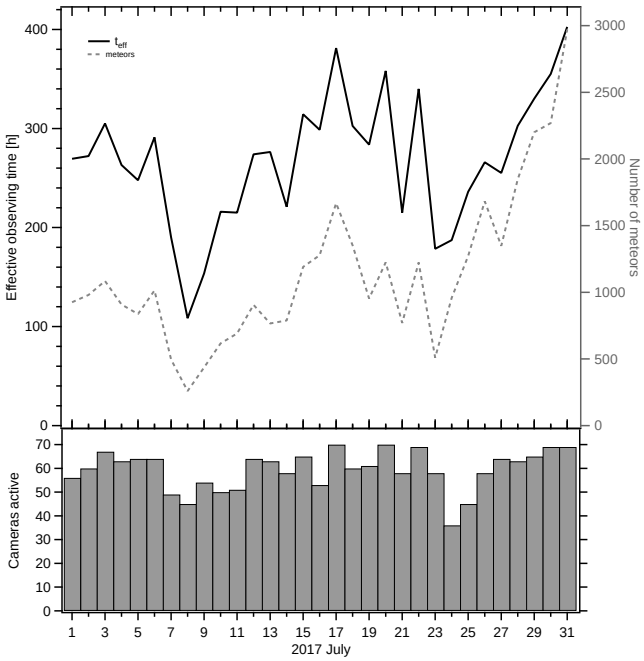

Figure 1 – Monthly summary for the effective observing time (solid black line), number of meteors (dashed gray line) and number of cameras active (bars) in 2017 July.

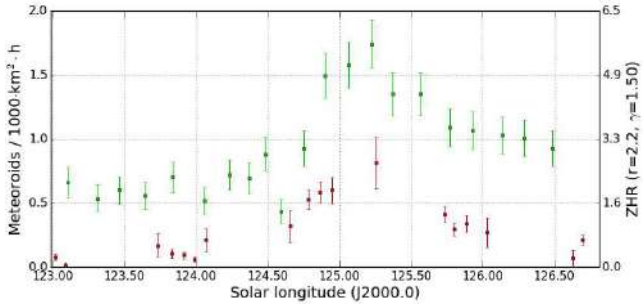

Figure 2 – Flux density profile of the July γ-Draconids 2011–2015 (lighter/green) and 2017 (darker/red), derived from video data of the IMO Network.

[1]Abenstalstr. 13b, 84072 Seysdorf, Germany.
Email: sirko@molau.de
[2]Via Bobbio 9a/18, 16137 Genova, Italy.
Email: stefano.crivello@libero.it
[3]Urbanizacao da Boavista, Lote 46, Linhaceira, 2305-114 Asseiceira, Tomar, Portugal. Email: rui.goncalves@ipt.pt
[4]Rua Aquilino Ribeiro, 23 - 1 Dto. 2790028 Carnaxide, Portugal. Email: carlos.saraiva@netcabo.pt
[5]via Umbria 21/d, 30037 Scorze (VE), Italy.
Email: stom@iol.it
[6]Na Ajdov hrib 24, 2310 Slovenska Bistrica, Slovenia.
Email: javor.kac@orion-drustvo.si

IMO bibcode WGN-461-molau-vidjul
NASA-ADS bibcode 2018JIMO...46...45M

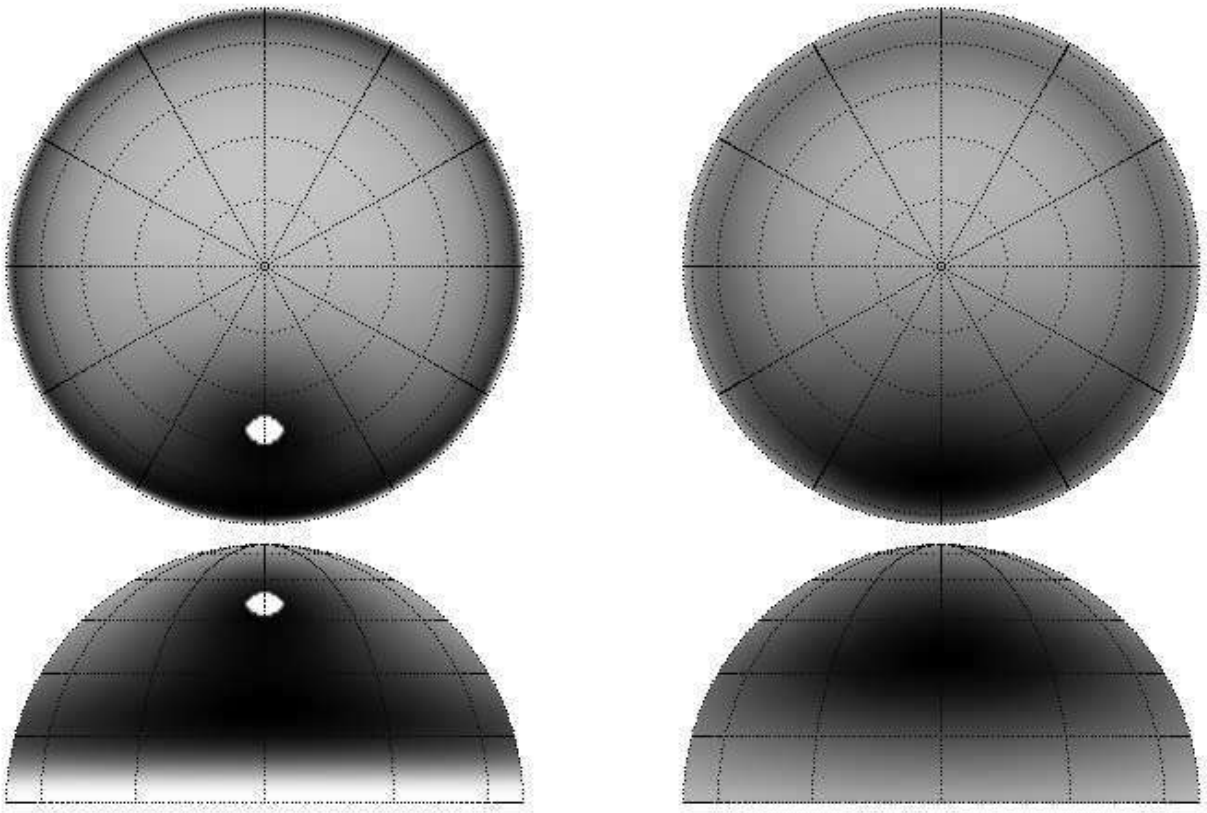

Figure 3 – Effective collection area per square degree for the whole celestial sphere (left) and for a 50° diameter camera field of view (right) for an "average meteor shower". Above is the total view of the sky with the zenith at the center, below is the horizontal view in radiant direction. White represents zero, black the biggest effective collection area. The grey levels of the two figures are scaled independently of each other.

whereby observing fields either near the radiant or near the horizon are favoured. In practice meteor cameras have a larger field of view, and the detection probability has to be integrated over the full field of view. Due to this, local effects like the "blind spot" at the radiant disappear. If the camera is pointed towards the horizon, the lower part of the field of view points below the horizon and does not contribute to the effective collection area at all, whereas higher parts extend towards those areas with maximum detection probability.

To analyze the effect quantitatively we extended the simulation via a variable camera field of view. For simplicity we simulate a circular field of view, since rectangular fields give even more degrees of freedom (proportion and orientation of axes) without changing the result significantly.

Figure 3 presents the effective collection area for an "average meteor shower" as in the last report (radiant at south with 10° declination, a population index of $r = 2.5$ and a velocity of $V_\infty = 50$ km/s). In the left hand image each pixel represents the effective collection area per each square degree at the celestial sphere; in the right hand image each pixel represents the collection area of a camera with 50° field of view diameter pointing in that direction. The deviation in detection probability between the individual observing directions are getting smaller, but they are still substantial. If, for example, we compare spots at 30° altitude in northern and southern direction, the results differ by a factor or 2.1 in the left hand case and by a factor of 1.8 in the right hand case. That is, a camera pointing towards the radiant is recording almost twice as many shower meteors as a camera pointing north. That matches the subjective impression when analyzing data of oppositely facing camera pairs, such as Remo2 and Remo3.

Comparing the impact of the individual meteor shower parameters pixel-wise and with a camera of 50° field of view, we get qualitatively the same picture. At low meteor shower velocities, small population indices or low atmospheric extinction, fields of view near the horizon have the largest effective collection area. At high meteor shower velocities, large population indices or large extinction, observing fields near the radiant are privileged. That is particularly prominent if we combine parameters with similar effects: Figure 4 shows at the left the effective collection area of a camera with 50° field of view for a shower with $V_\infty = 30$ km/s, $r = 2.0$ and an extinction of 0.20, and at the right for a shower with $V_\infty = 70$ km/s, $r = 3.0$ and an extinction of 0.45. In the first case, an observing field in the south at 25° altitude fares better than one at the zenith by a factor of four. In the second case, there is a three-fold increase when the center is at 45° altitude south (near the radiant) compared with when it is at the zenith.

Now we are only missing the temporal aspect, because the camera observes not just when the radiant culminates, but all-night long. So, once more, we take the "average meteor shower" from Figure 3 and let the radiant raise from east to south during six hours of observing time (Figure 5). On the left is the picture from

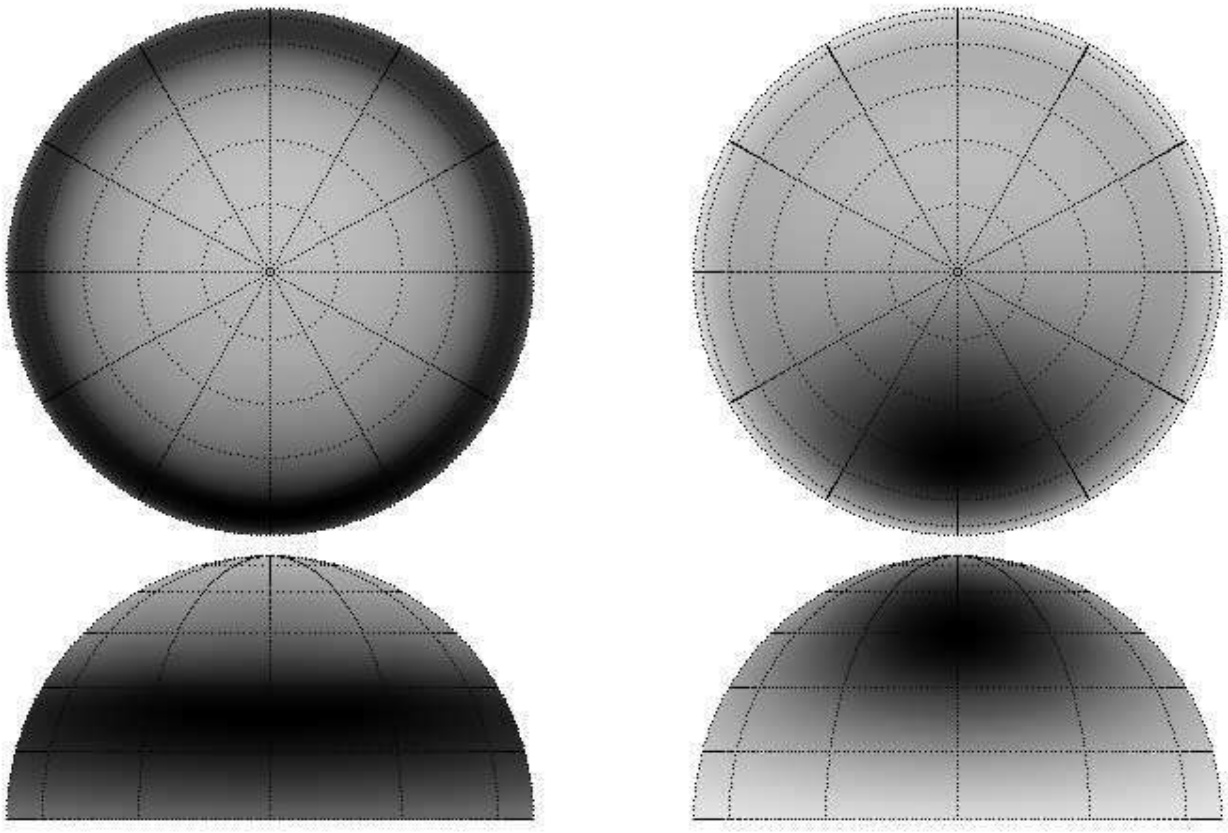

Figure 4 – Comparison of the effective collection area of a camera with 50° field of view for a meteor shower with low velocity and small population index at low extinction (left), and for a meteor shower with high velocity and a large population index at high extinction (right). The grey levels of the two figures are scaled independently of each other.

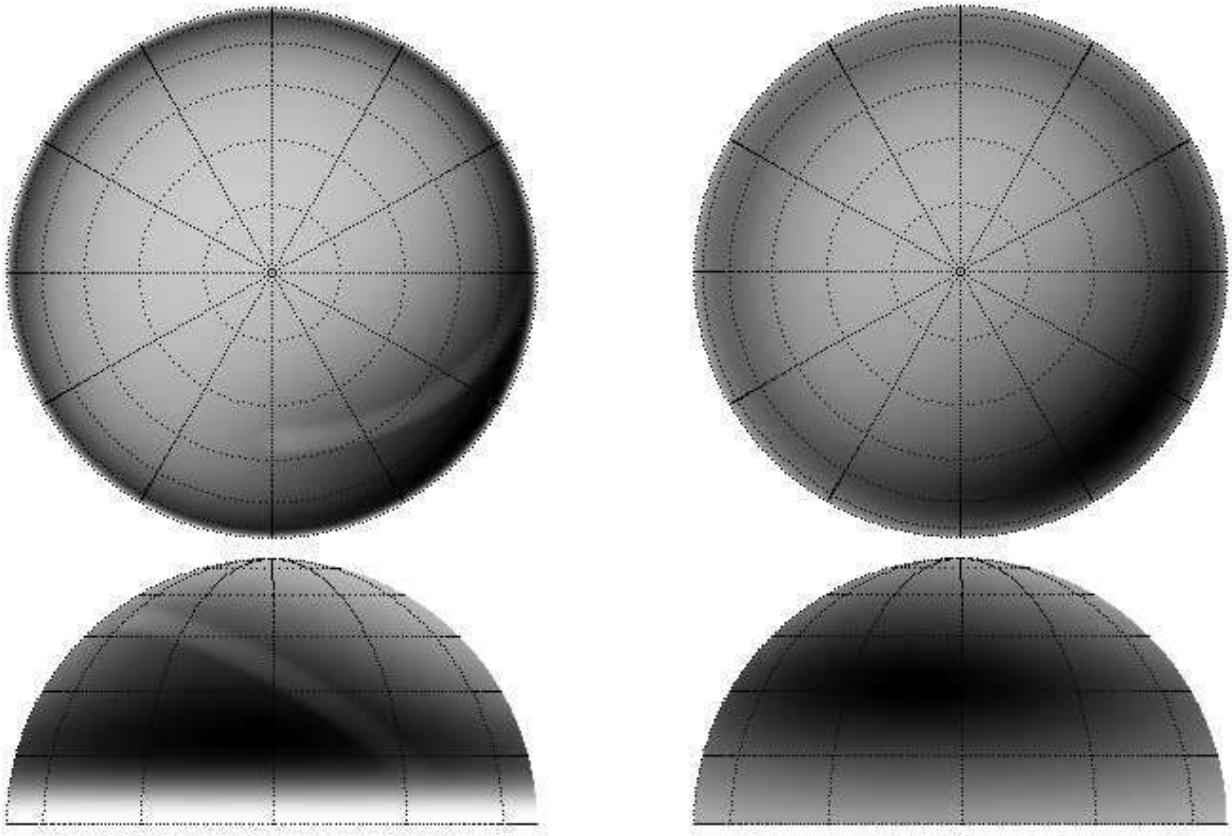

Figure 5 – Effective collection area per square degree at the celestial sphere (left) and with 50° camera field of view diameter (right) for an "average meteor shower", whose radiant is moving from east to south during six hours of observation. The grey levels of the two figures are scaled independently of each other.

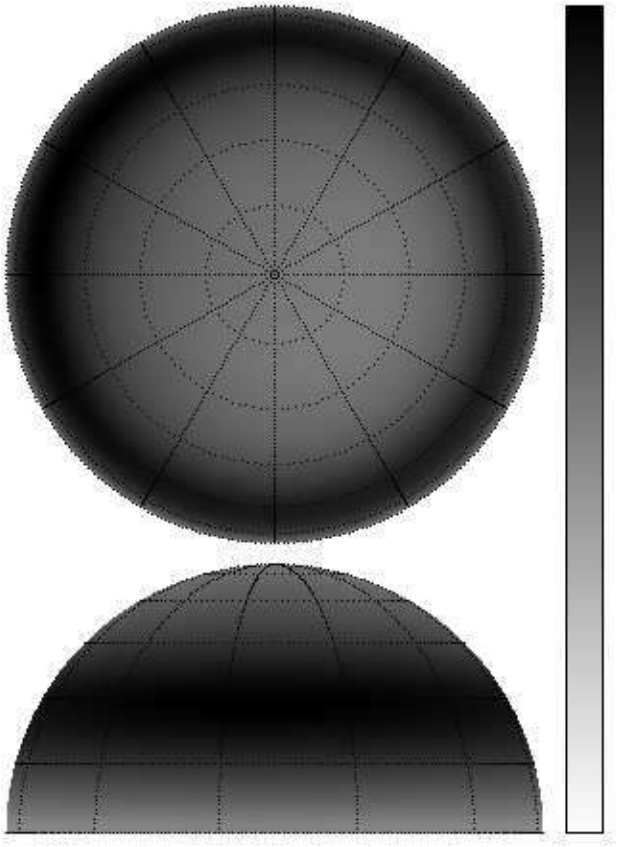

Figure 6 – Best observing direction for a video camera to record the July γ-Draconids. The lower figure is oriented north-west towards the maximum effective collection area.

the last monthly report (Molau et al., 2017) with the effective collection area per pixel, right the collection area of a camera with 50° field of view diameter. The best detection rate is achieved with a field of view in a south-eastern direction at about 30° altitude.

Finally, let us return to the July γ-Draconids. Where should a camera be best pointed for this, a circumpolar meteor shower radiant in central Europe? The answer is given in Figure 6: The observing direction hardly matters – the camera just needs to be pointed at 30° altitude. Fields of view near the zenith are not advised.

References

Molau S., Crivello S., Goncalves R., Saravia C., Stomeo E., and Kac J. (2016). "Results of the IMO Video Meteor Network – July 2016". *WGN, Journal of the IMO*, **44:6**, 205–210.

Molau S., Crivello S., Goncalves R., Saravia C., Stomeo E., and Kac J. (2017). "Results of the IMO Video Meteor Network – June 2017, and effective collection area study". *WGN, Journal of the IMO*, **45:6**, 149–155.

Handling Editor: Javor Kac

Code	Name	Location	Camera	FOV [°²]	Stellar LM [mag]	Eff.CA [km²]	Nights	Time [h]	Meteors
ARLRA	Arlt	Ludwigsfelde/DE	Ludwig2 (0.8/8)	1475	6.2	3779	24	72.5	434
BERER	Berkó	Ludányhalászi/HU	Hulud1 (0.8/3.8)	5542	4.8	3847	17	82.6	616
BOMMA	Bombardini	Faenza/IT	Mario (1.2/4.0)	5794	3.3	739	31	183.7	1222
BREMA	Breukers	Hengelo/NL	Mbb3 (0.75/6)	2399	4.2	699	19	51.5	188
BRIBE	Klemt	Herne/DE	Hermine (0.8/6)	2374	4.2	678	23	52.5	230
		Bergisch Gladbach/DE	Klemoi (0.8/6)	2286	4.6	1080	18	64.5	234
CARMA	Carli	Monte Baldo/IT	Bmh2 (1.5/4.5)*	4243	3.0	371	24	108.7	856
CASFL	Castellani	Monte Baldo/IT	Bmh1 (0.8/6)	2350	5.0	1611	29	154.4	600
CINFR	Cineglosso	Faenza/IT	Jenni (1.2/4)	5886	3.9	1222	31	190.3	697
CRIST	Crivello	Valbrevenna/IT	Bilbo (0.8/3.8)	5458	4.2	1772	30	169.1	901
			C3P8 (0.8/3.8)	5455	4.2	1586	29	131.3	548
			Stg38 (0.8/3.8)	5614	4.4	2007	31	176.8	1390
ELTMA	Eltri	Venezia/IT	Met38 (0.8/3.8)	5631	4.3	2151	31	134.4	618
FORKE	Förster	Carlsfeld/DE	Akm3 (0.75/6)	2375	5.1	2154	15	52.6	292
GONRU	Goncalves	Foz do Arelho/PT	Farelho1 (0.75/4.5)	2286	3.0	208	12	56.0	27
		Tomar/PT	Templar1 (0.8/6)	2179	5.3	1842	28	192.1	1088
			Templar2 (0.8/6)	2080	5.0	1508	28	196.3	769
			Templar3 (0.8/8)	1438	4.3	571	28	181.3	345
			Templar4 (0.8/3.8)	4475	3.0	442	28	194.6	806
			Templar5 (0.75/6)	2312	5.0	2259	29	178.5	855
GOVMI	Govedič	Središče ob Dravi/SI	Orion2 (0.8/8)	1447	5.5	1841	29	125.8	462
			Orion4 (0.95/5)	2662	4.3	1043	30	116.7	295
HERCA	Hergenrother	Tucson/US	Salsa3 (0.8/3.8)	2336	4.1	544	22	119.5	289
HINWO	Hinz	Schwarzenberg/DE	Hinwo1 (0.75/6)	2291	5.1	1819	21	69.0	278
IGAAN	Igaz	Budapest/HU	Hupol (1.2/4)	3790	3.3	475	26	117.6	151
JONKA	Jonas	Budapest/HU	Husor (0.95/4)	2286	3.9	445	29	118.4	304
			Husor2 (0.95/3.5)	2465	3.9	715	29	137.2	332
KACJA	Kac	Ljubljana/SI	Orion1 (0.8/8)	1399	3.8	268	28	128.6	736
		Kamnik/SI	Cvetka (0.8/3.8)*	4914	4.3	1842	23	113.4	777
			Rezika (0.8/6)	2270	4.4	840	23	116.1	1114
			Stefka (0.8/3.8)	5471	2.8	379	23	106.3	538
		Kostanjevec/SI	Metka (0.8/12)*	715	6.4	640	29	128.1	366
LOJTO	Łojek	Grabniak/PL	Pav57 (1.0/5)	1631	3.5	269	9	40.3	200
MACMA	Maciejewski	Chełm/PL	Pav35 (0.8/3.8)	5495	4.0	1584	28	94.8	396
			Pav36 (0.8/3.8)*	5668	4.0	1573	29	118.5	625
			Pav43 (0.75/4.5)*	3132	3.1	319	26	105.5	322
			Pav60 (0.75/4.5)	2250	3.1	281	27	112.9	508

Table 1 – Observers contributing to 2017 July data of the IMO Video Meteor Network. Eff.CA designates the effective collection area; the overall number of nights is the number of nights with at least one camera operating, the overall observing time and number of meteors are sums over all cameras.

Table 1 – Observers contributing to 2017 July data of the IMO Video Meteor Network – continued from previous page.

Code	Name	Location	Camera	FOV [°²]	Stellar LM [mag]	Eff.CA [km²]	Nights	Time [h]	Meteors
MARRU	Marques	Lisbon/PT	CAB1 (0.75/6)	2362	4.8	1517	29	202.4	784
			RAN1 (1.4/4.5)	4405	4.0	1241	23	124.3	286
MASMI	Maslov	Novosibirsk/RU	NOWATEC (0.8/3.8)	5574	3.6	773	21	60.6	301
MOLSI	Molau	Seysdorf/DE	AVIS2 (1.4/50)*	1230	6.9	6152	24	85.5	810
			ESCIMO2 (0.85/25)	155	8.1	3415	21	87.0	190
			MINCAM1 (0.8/8)	1477	4.9	1084	23	81.6	423
		Ketzür/DE	REMO1 (0.8/8)	1467	6.5	5491	24	73.9	496
			REMO2 (0.8/8)	1478	6.4	4778	24	79.3	552
			REMO3 (0.8/8)	1420	5.6	1967	24	91.5	517
			REMO4 (0.8/8)	1478	6.5	5358	25	90.4	600
MORJO	Morvai	Fülöpszállás/HU	HUFUL (1.4/5)	2522	3.5	532	30	155.5	339
MOSFA	Moschini	Rovereto/IT	ROVER (1.4/4.5)	3896	4.2	1292	26	56.0	347
OCHPA	Ochner	Albiano/IT	ALBIANO (1.2/4.5)	2944	3.5	358	15	68.6	155
OTTMI	Otte	Pearl City/US	ORIE1 (1.4/5.7)	3837	3.8	460	29	128.6	274
PERZS	Perkó	Becsehely/HU	HUBEC (0.8/3.8)*	5498	2.9	460	28	128.1	629
ROTEC	Rothenberg	Berlin/DE	ARMEFA (0.8/6)	2366	4.5	911	19	58.6	197
SARAN	Saraiva	Carnaxide/PT	RO1 (0.75/6)	2362	3.7	381	26	172.5	331
			RO2 (0.75/6)	2381	3.8	459	28	183.4	475
			RO3 (0.8/12)	710	5.2	619	25	170.7	701
			RO4 (1.0/8)	1582	4.2	549	26	152.3	222
			SOFIA (0.8/12)	738	5.3	907	26	137.9	339
SCALE	Scarpa	Alberoni/IT	LEO (1.2/4.5)*	4152	4.5	2052	28	127.2	220
SCHHA	Schremmer	Niederkrüchten/DE	DORAEMON (0.8/3.8)	4900	3.0	409	22	75.7	280
SLAST	Slavec	Ljubljana/SI	KAYAK1 (1.8/28)	563	6.2	1294	25	105.2	416
			KAYAK2 (0.8/12)	741	5.5	920	26	121.5	164
STOEN	Stomeo	Scorze/IT	MIN38 (0.8/3.8)	5566	4.8	3270	31	136.9	1090
			NOA38 (0.8/3.8)	5609	4.2	1911	31	138.7	904
			SCO38 (0.8/3.8)	5598	4.8	3306	31	140.5	1008
STRJO	Strunk	Herford/DE	MINCAM2 (0.8/6)	2354	5.4	2751	23	61.3	278
			MINCAM3 (0.8/6)	2338	5.5	3590	24	51.6	163
			MINCAM4 (0.8/6)	2306	5.0	1412	24	61.4	124
			MINCAM5 (0.8/6)	2349	5.0	1896	23	55.5	181
			MINCAM6 (0.8/6)	2395	5.1	2178	23	45.9	134
TEPIS	Tepliczky	Agostyán/HU	HUAGO (0.75/4.5)	2427	4.4	1036	29	122.5	323
			HUMOB (0.8/6)	2388	4.8	1607	26	109.4	474
WEGWA	Wegrzyk	Nieznaszyn/PL	PAV78 (0.8/6)	2286	4.0	778	23	75.5	291
* active field of view smaller than video frame						Overall	31	8 309.9	35 427

The International Meteor Organization

www.imo.net

Follow us on Facebook InternationalMeteorOrganization

Follow us on Twitter @IMOMeteors

Council

President: Cis Verbeeck,
Bogaertsheide 5, 2560 Kessel, Belgium.
e-mail: cis.verbeeck@scarlet.be

Vice-President: Jürgen Rendtel,
Eschenweg 16, D-14476 Marquardt, Germany.
tel. +49 33208 50753
e-mail: jrendtel@aip.de

Secretary-General: Robert Lunsford,
14884 Quail Valley Way, El Cajon,
CA 92021-2227, USA. tel. +1 619 755 7791
e-mail: lunro.imo.usa@cox.net

Treasurer: Marc Gyssens, Heerbaan 74,
B-2530 Boechout, Belgium.
e-mail: marc.gyssens@uhasselt.be
BIC: GEBABEBB
IBAN: BE30 0014 7327 5911
Bank transfer costs are always at your expense.

Other Council members:

Megan Argo, Jodrell Bank Centre for Astrophysics, Alan Turing building, University of Manchester, Oxford Road, Manchester, M13 9PL, UK.
e-mail: megan.argo@gmail.com

Javor Kac (see details under WGN)

Detlef Koschny, Zeestraat 46,
NL-2211 XH Noordwijkerhout, Netherlands.
e-mail: detlef.koschny@esa.int

Masahiro Koseki, 4-3-5 Annaka, Annaka-shi,
Gunma-ken 379-0116, Japan.
e-mail: geh04301@nifty.ne.jp

Sirko Molau, Abenstalstraße 13b, D-84072 Seysdorf, Germany. e-mail: sirko@molau.de

Jean-Louis Rault, Société Astronomique de France, 16, rue de la Vallée, 91360 Epinay sur Orge, France. e-mail: f6agr@orange.fr

Paul Roggemans, Pijnboomstraat 25, 2800 Mechelen, Belgium, e-mail: paul.roggemans@gmail.com

Galina Ryabova, Res. Inst. of Appl. Math. & Mech., Tomsk State University, Lenin pr. 36, build. 27, 634050 Tomsk, Russian Federation.
e-mail: ryabova@niipmm.tsu.ru

Damir Šegon, J. Rakovca 3, 52100 Pula, Croatia. e-mail: damir.segon@pu.t-com.hr

Juraj Tóth, Fac. Math., Phys. & Inf., Comenius Univ., Mlynska dolina, 84248 Bratislava, Slovakia.
e-mail: toth@fmph.uniba.sk

Commission Directors

Visual Commission: Rainer Arlt (rarlt@aip.de)
Generic e-mail address: visual@imo.net
Electronic visual report form:
http://www.imo.net/visual/report/electronic

Video Commission: Sirko Molau (video@imo.net)

Photographic Commission: Bill Ward (William.Ward@glasgow.ac.uk)
Generic e-mail address: photo@imo.net

Radio Commission: Jean-Louis Rault (radio@imo.net)

Fireballs: Online fireball reports:
http://fireballs.imo.net

Outreach Officer

Jure Atanackov, e-mail: jureatanackov@gmail.com

Webmaster

Karl Antier, e-mail: webmaster@imo.net

WGN

Editor-in-chief: Javor Kac
Na Ajdov hrib 24, SI-2310 Slovenska Bistrica, Slovenia. e-mail: wgn@imo.net;
include METEOR in the e-mail subject line

Editorial board: Ž. Andreić, M. Argo, D.J. Asher, F. Bettonvil, J. Correira, M. Gyssens, C. Hergenrother, T. Heywood, J.-L. Rault, J. Rendtel, C. Verbeeck, S. de Vet, D. Vida.

IMO Sales

Available from the Treasurer or the Electronic Shop on the IMO Website	€	$
IMO membership, including subscription to WGN Vol. 46 (2018)		
Surface mail	26	35
Air Mail (outside Europe only)	49	65
Electronic subscription only	21	25
Proceedings of the International Meteor Conference on paper		
1990, 1991, 1993, 1995, 1996, 1999, 2000, 2002, 2003, per year	9	12
2007, 2010, 2011, per year	15	20
2012, 2013, 2014, 2015 per year	25	34
Proceedings of the Meteor Orbit Determination Workshop 2006	15	20
Radio Meteor School Proceedings 2005	15	20
Handbook for Meteor Observers	15	20
Meteor Shower Workbook	12	16
Electronic media		
Meteor Beliefs Project ZIP archive	6	8


Marcelo Zurita